UNIVERSITY OF CALIFORNIA
RIVERSIDE

Electrochemical Synthesis and Characterization of Nanostructured Chalcogenide Materials

A Dissertation submitted in partial satisfaction
of the requirements for the degree of

Doctor of Philosophy

in

Chemical and Environmental Engineering

by

Chong Hyun Chang

March 2011

Dissertation Committee:
Dr. Nosang V. Myung, Chairperson
Dr. David Kisailus
Dr. David Cwiertny
Dr. Christopher Dames

The Dissertation of Chong Hyun Chang is approved:

_____

_____

_____

_____

Committee Chairperson

University of California, Riverside

Acknowledgements

Without the countless help, advice and encouragement I received from the people I mention below as well as the countless others who have helped me in this journey, I would never have completed this dissertation.

First and foremost, I would like to give my sincere thanks to my advisor, Prof. Nosang V. Myung, for giving me the chance to explore the world of nanotechnology and supporting my research. His passionate guidance, friendly relationship, and supportive concern for my research during the progress of my Ph.D study were unshakeable foundations of my journey to accomplish the higher goals as he has always taught me. Also, I would further like to express my gratitude to all members of my dissertation committee, Prof. David Kisailus, Prof. David Cwiertny and Prof. Christopher Dames, for their comments, reviews and encouragement of my research. I am also especially very grateful to Prof. Bongyoung Yoo and Dr. Youngwoo Rheem for their guidance and help to keep study in this lab.

I want to express my deepest appreciation to numerous collaborators and colleagues for their friendship, help, and advice, including: Becky, Carlos, Charles, Divya, Fang, Feng, Dr. Hosik Park, Hoyoung, Hugo, Prof. Hyun Jung Kim, Hyunsung, Dr. Jae-Hong Lim, Jiwon, Joun, Dr. Kun-Jae Lee, Lauren, Mangesh, Max, Miluo, Miso, Mubeen, Nicha, Sandra, Sira, Shen-Long, Sudeep, Tapan, Dr. Yongsuk Hong; and to Korean family in UCR: Dr. Bongsoo Jung, Dr. Bumsub Kim, Joonbok Lee, Panya & Dr. Jaewoo

Kim, Dr. Seongyup Kim, Dr. Seung Hyun Kang, Dr. Wanyoung Jang, Dr. Yoonjoo Kim & Younghoon Kim, Zhehui Jin.

Final, special thanks go to my parents, brothers and their family, and all of my friends for their unconditional love and unlimited sacrifice. SOLI DEO GLORIA!

ABSTRACT OF THE DISSERTATION

Electrochemical Synthesis and Characterization of Nanostructured Chalcogenide Materials

by

Chong Hyun Chang

Doctor of Philosophy, Graduate Program in Chemical and Environmental Engineering
University of California, Riverside, March 2011
Dr. Nosang V. Myung, Chairperson

Nanostructured materials have attracted extensive attention due to their small dimension and enhanced properties compared to bulk materials, and their large range of potential applications in energy harvesting devices. Among these materials, nanostructured chalcogenides play an important role in thermoelectric and solar cell devices. Electrochemical techniques have drawn attention as an improved method for synthesizing nanostructured chalcogenide materials, since they provide a cost-effective, simple, and versatile method for depositing various kind of chalcogenides with tunable nanostructures and properties.

The overall objective of this dissertation work is to develop the following electrochemical techniques:

1) to synthesize nanostructured chalcogenide materials (*e.g.* Bi_xTe_y, Pb_xTe_y and Cd_xTe_y) with well-controlled dimensions, surface morphologies and compositions

2) to systematically investigate the effect of experimental parameters on their nanostructures
3) to characterize their tunable properties
4) and ultimately to establish a guidance of experimental design for further synthesis of other nanostructured chalcogenide materials.

In this dissertation, the viability of using electrochemical methods for synthesizing nanostructured three chalcogenide materials – Bismuth telluride (Bi_xTe_y) Lead telluride (Pb_xTe_y) and Cadmium telluride (Cd_xTe_y) was tested. An easy way to tune their size (nano to micro), surface morphology (from novel nanostructures to nanoparticles and core/shell hybrid nanostructure) and composition (excess either electropositive element or chalcogens) by tailoring the electrochemical parameters such as electrolyte composition, type and thickness of sacrificial materials, and reaction time of electrochemical techniques, including electrodeposition (ED) and galvanic displacement (GD), was demonstrated.

Table of Contents

List of Figures

List of Tables

Chapter 1

Introduction

1.1 Motivation

As population and economic growth continue all over the world, the U.S. government has predicted that global energy demands will also grow by 50% over the next two decades [1]. Unfortunately, current research on sustainable energy has not progressed enough to satisfy this additional burden. Recently, thermoelectrics and photovoltaics have become very attractive for their potential in harvesting the energy lost from the staggering amount of waste heat source and the energy received from the sun [2,3]. Thermoelectric (TE) power generators and photovoltaic (PV) devices have very similar advantages, including solid-state operation, zero-emissions, vast scalability, zero maintenance, no noise, and a long operating lifetime [4,5]. In spite of these obvious advantages, their implementation in power generation for human activities have been very limited because of their low conversion efficiency and high manufacturing cost [4,5]. Low-dimensional structures of TE and PV materials has held great promise in overcoming these limitations, since they display novel and enhanced properties compared to bulk materials. Nanostructured materials can be used for enhancement of energy conversion efficiency by tailoring their physical, electrical and optoelectrical properties. Furthermore, improvements in the electrochemical technique have been shown to have great promise in overcoming the limitation of high production cost, because they provide

simple and cost competitive methods for depositing various kind of compound semiconductor and synthesis of nanostructures compared to conventional method.

1.2 Thermoelectrics (TE) and Photovoltaics (PV) – An Overview:

The thermoelectric (TE) effect describes the generation of electrical potential when a material is placed in a temperature gradient. There are two major phenomena related to the thermoelectric effect: (1) the direct generation of an electric voltage from the temperature gradient known as the Seebeck effect, $\Delta T \rightarrow E$ (power generation), and (2) the conversion of electric current to temperature movement known as the Peltier effect, $E \rightarrow \Delta T$ (Cooler/Heater or thermoelectric heat pump) [3]. Base on the TE effect, there have been a number of efforts to generate power from small thermal gradient sources such as the waste heat from power plants, and to heat or cool objects for applications like air conditioning and refrigeration. However, TE devices currently have limited economical applications due to their low conversion efficiencies and relatively low power densities [4]. Despite these disadvantages, the discovery of new thermoelectric materials, especially among low dimensional structures, that show significant improvement on the energy conversion efficiency of TE devices have revitalized research efforts in the field. The efficiency of TE devices directly depend on the dimensionless figure of merit (ZT), requiring values of the order of unity or greater [3]. The thermoelectric figure of merit is defined as

$$ZT = \frac{S^2 \sigma}{\kappa} T \tag{1}$$

where S is the Seebeck coefficient ($\mu V \cdot K^{-1}$), σ is the electrical conductivity ($\Omega^{-1} \cdot m^{-1}$), κ is the thermal conductivity ($W \cdot m^{-1} \cdot K^{-1}$), T (K) is the absolute temperature, and $S^2\sigma$ is usually called as the thermoelectric power factor. Based on this equation, the TE materials should possess a large Seebeck coefficient to maximize the energy conversion, high electrical conductivity to minimize the effect of Joule heating, and low thermal conductivity to retain heat at the junctions to maximize the ZT [6]. It is, however, difficult to optimize the ZT values because three parameters (*S, σ,* and *κ*) are dependent on each others in bulk materials. For example, the Seebeck coefficient decreases with increasing electrical conductivity because of carrier density considerations as shown in Figure 1.1 [3].

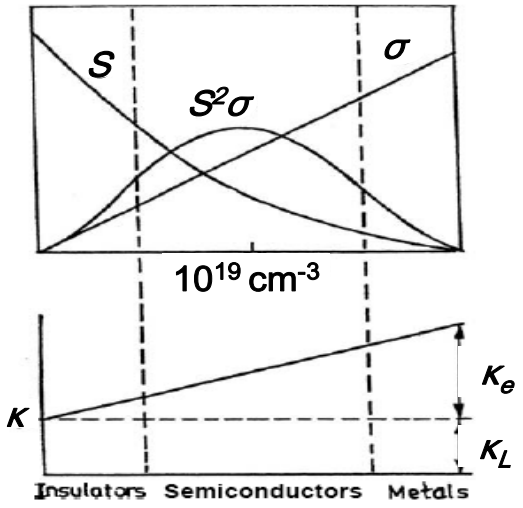

Figure 1.1. Dependence of *S, σ, κ* and $S^2\sigma$ as a function of the carrier concentration.

Therefore, improvement and optimization of TE efficiency requires independent control and adjustment of each TE property, which can be achieved by nanoengineering

TE materials with controlled composition, dimension, and structure. Typically, accomplishing this enhancement of TE efficiency requires synthesis of semiconducting materials with reduced thermal conductivity without affecting the electrical properties.

Photovoltaics (PV) are another innovative research field to generate energy by directly converting sunlight into electricity. Solar cells are one of the most promising alternatives to fossil fuels because the tremendous amount of energy available from the sun. PV effect describes how semiconducting materials absorb incoming photons of sunlight by excitation of electrons from the valence band to conduction band in a semiconductor and release electron-hole pairs. At a p-n junction interface, electrical current flows as a result of electrons in the n-type semiconductor migrating toward the p-type and, vice versa for holes. Since the semiconductor p-n junction had been used for solar cells in Bell laboratory in 1941, a variety semiconducting materials have been studied. In particular, II-VI compound semiconductors (cadmium chalcogenide) such as CdTe, CdSe, and CdS have been rigorously developed as they are direct band gap semiconductors with the high optical absorption coefficient in the visible spectrum, which makes them ideal materials for photovolatics. In bulk semiconductor solar cells, an absorbed photon excites a single electron-hole pair, known as the one-to-one relationship, and excess electron-hole pairs in the band gap are wasted as heat. This phenomenon induces relatively low conversion efficiency in bulk semiconductor solar cells. For example, one data from the literature reports that the best single crystal silicon solar cell has an efficiency of ~25% in the laboratory scale and ~18% in commercial practice, with a theoretical/maximum thermodynamic conversion efficiency at ~32% based on the

assumption of a single p-n junction, and unconcentrated sunlight [7]. Therefore, it is highly desirable to develop low cost solar cells with an improved conversion efficiency. Quantized semiconductor nanostructures may be a solution to this problem, as they are expected to generate many electron-hole pairs from a single absorbed photon, with the extra pairs exited multiple steps in the band gap. For instance, semiconductor quantum dots of PbSe and PbS have high efficiencies because one photon yields three electron-hole pairs, generating 3 times as many excitons as shown in Figure 1.2 [2].

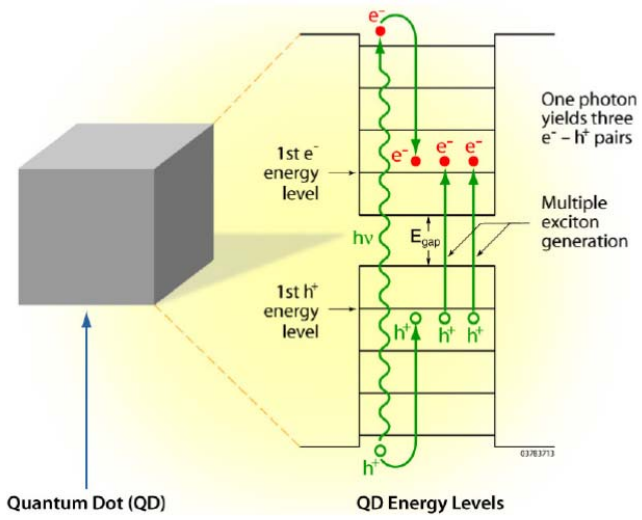

Figure 1.2. Multiple exciton generation in PbSe and PbS quantum dots.

Therefore, the development of TE devices and solar cells based on nanostructured materials has drawn attention because they can overcome limitations in efficiency and high production cost by displaying novel and enhanced properties compared to bulk materials while still having extremely inexpensive cost of production. By utilizing specific compositions, sizes and structures of materials, the energy harvesting devices

based on nanostructured semiconductors can achieve a decoupling the interdependence between three TE parameters (*S, σ,* and *κ*), to enhance light absorption properties via confinement effects, and to increase the surface/junction area for higher conversion efficiency. These factors can provide significant advancement towards achieving viable energy harvesting devices, and give an improved synthesis of materials and fabrication of device structures to implement low-cost solar cells exhibiting high cell performance.

1.3 Thermoelectric and Photovoltaic Materials

1.3.1 Chalcogenide

The chemically and technologically important elements in the group 16 of the Periodic Table such as sulfur, selenium and tellurium are commonly referred to as chalcogens. A chalcodenide is a chemical compound of chalcogens with at least one more electropositive element [8]. The basic physical properties of chalcogens (e.g. sulfur, selenium, and tellurium) are indicated in Table 1.1 [8].

Table 1.1. The basic physical properties of sulfur, selenium, and tellurium

	S	Se	Te
Atomic mass	32.07	78.96	127.60
Atomic number	16	34	52
Electronic structure	$[Ne]3s^2 3p^4$	$[Ar]3d^{10}4s^2 4p^4$	$[Kr]4d^{10}5s^2 5p^4$
Melting point (°C)	119 (S_β)	220.5 (gray)	449.8
Boiling point (°C)	444.6	684.8	989.8
Density (g cm^{-3})	2.06 (S_α)	4.82 (gray)	6.25
Atomic radius (10^{-10} m)	1.00	1.40	1.37
$X^{(II)}$ covalent radius (10^{-10} m)	1.03	1.16	1.37
Electronegativity (Allred–Rochow; Pauling)	2.44; 2.58	2.48; 2.55	2.01; 2.10
First ionization potential (eV)	10.38	9.75	9.01

Based on various chemical compounds of these calcogens, the chalcogenide materials, especially bismuth- , lead- and cadmium-chalcogenide, have attracted intense interest on their important properties for fundamental research and for their potential applications in thermoelctrics, photovoltaics, electronics, optics, batteries, and energy harvesting devices [8]. Among these, chemical compounds with tellurium, such as bismuth telluride (Bi_2Te_3), lead telluride (PbTe) and cadmium telluride (CdTe), are focused on this thesis, because those are well known to be good TE and PV materials in practice.

1.3.2 Chalcogenide as a TE and PV Materials

Good TE materials usually have carrier concentrations ranging from 10^{19} to 10^{21} cm^{-3}, which are located in the heavily doped region with low thermal conductivity, as shown in Figure 1.1. In other words, heavily doped semiconductors provide a balance between the large Seebeck coefficient (S) of lightly doped semiconductors and the high electrical conductivity of metals, providing an excellent basis for optimizing the ZT value [9]. The total thermal conductivity of thermoelectrics is the sum of the lattice thermal conductivity (κ_L) and the electrical thermal conductivity (κ_e). Lattice thermal conductivity (κ_L) is decided by phonons traveling through the lattice by vibrations, whereas the electrical thermal conductivity (κ_e) is controlled by electrons or holes transporting heat. In many semiconductors, the lattice thermal conductivity is much greater than the electrical conductivity, and as such minimization of the lattice thermal conductivity (κ_L) is a key factor in enhancing the ZT value. Accordingly, a large number of IV-VI and V-VI semiconductor materials, such as Bi_2Te_3 and PbTe, have been rigorously investigated for

their reduction of atomic vibration frequencies as well as their uncompromised electrical conductivity (σ) from their lattice thermal conductivities (κ_L).

Bismuth telluride (Bi_2Te_3) is one of the most promising TE materials to date because of its highest ZT values near room temperature as shown in Figure 1.3 [3,10]. The structure of Bi_2Te_3 is described as a rhombohedral unit cell with a narrow band gap (E_g = 0.11–0.15 eV at room-temperature), and its band gap changes slightly with temperature. Also, n-type or p-type BiTe can be synthesized by slight modulation of the composition from its stoichiometric ratio (excess Bi (p-type) or excess Te (n-type)).

Lead Telluride (PbTe) is a direct band gap semiconductor with a narrow band gap (E_g = 0.31 eV at 300K). Similar to Bi_2Te_3, its semiconductor conductivity type (*e.g.* n-type or p-type) can also be tuned by controlling the deposit composition in proportion to its stoichiometry (excess Pb (n-type) or excess Te (p-type)). The TE properties of PbTe show the highest ZT values in the intermediate temperature range (near 500-600 K) of up to 1000 K as shown in Figure 1.3. [12].

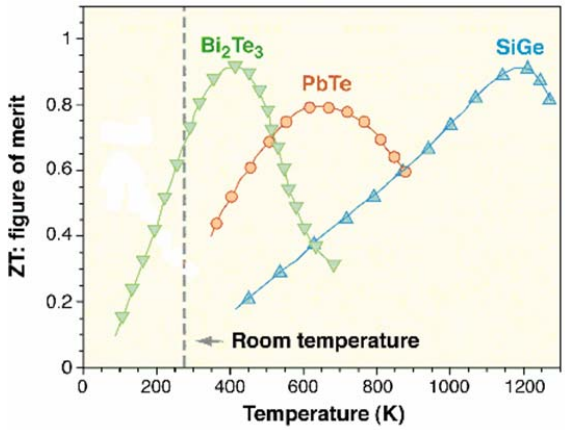

Figure 1.3. The thermoelectric figure-of-merit (ZT) as a function of operating temperature.

Cadmium telluride (CdTe) was selected as a PV material since its energy band gap (1.44eV) is very well matched with the solar spectrum [13]. Its high absorption coefficient also makes it have one of the highest potential efficiency in solar cells. The conductivity type of CdTe can be changed by adding a disproportional amount of either Cd or Te (excess Cd (n-type) or excess Te (p-type)) [13].

1.4 Importance of Electrochemical Method

The chalcogenide materials are generally prepared by high temperature solidification via vaccum evaporation or chemical vapor deposition (CVD). These processes require high energy for their processing steps, and also emits many gaseous waste materials. However, electrochemical process is a simple and cost competitive method for depositing various compound semiconductors and also for synthesis of nanostructures. This method employs electrochemical reactions in the electrolyte, thus opening up possibilities for the preparation of large area and low cost nanostructured solar cells. This is because the mechanics allow for easy control of growth parameters such as applied potential, current, pH, temperature, and electrolyte composition. [14]

1.4.1 Electrodeposition (ED)

Electrodeposition has been employed as a synthesis process for nanostructured mateirials (*e.g.* nanowires, nanotubes, nanoaprticles, and etc.) over recent decades [14]. It is a process using electrical potential or current to reduce cations of a desired material in the electrolyte. Electrodeposition can be carried out in a traditional three-electrode cell.

A conductive substrate, a saturated calomel electrode (SCE) and a noble metal such as platinum-coated titanium are used as a working, reference and counter electrode, respectively. Once those electrodes are submerged in an electrolyte containing cations of the materials to be deposited, the cations are electrochemically deposited (reduction) on the cathod by applyication of an external electric field. The reduction of desired cations (M^{n+}) in the electrolyte is described as

$$M^{n+} + ne^{-} \rightarrow M^{0} \tag{1}$$

where M is a desired material (e.g. Ni, Co, Fe etc.) and n is the number of electrons.

1.4.2 Galvanic Displacement (GD)

Galvanic displacement (GD) is commonly referred as an electrochemical process since GD reactions occur due to the difference in redox potential among materials. A more noble metal is reduced and deposited on the substrates while the sacrificial materials is oxidized in this process, which means that no external power is needed for the process[14]. The GD method is a very attractive alternative for the synthesis of chalcogenides, as it provides control over the size, surface morphology, and composition of nanomaterials by adjusting the synthesis parametres such as electrolyte composition, type and thickness of sacrificial materials, as well as the reaction time. For example, Bi_2Te_3 nanotubes can be synthesized with controlled composition by simply adjusting the Bi^{3+} and $HTeO_2^{+}$ concentration [15]. With obvious advantages, GD is a facile and versatile method for synthesizing of chalcogenide nanostructures with controlled composition and morphology.

1.5 Objective and Scope

The overall objective of this dissertation work is to synthesize nanostructured chalcogenide materials (*e.g.* Bi_xTe_y, Pb_xTe_y and Cd_xTe_y) with well-controlled dimensions, surface morphologies and compositions by various electrochemical techniques including electrodeposition (ED) and galvanic displacement (GD), and to investigate their size, morphology and composition dependent electrical and optoelectrical properties. Results from this systematic investigtaion are expected to provide a clear understanding of the growth mechanism and the effect of synthesis parameters on the nanomaterials, which will help guide future experimental designs. Further, this study has the potential to establish a new method for synthesizing chalcogenide materials with nanostructures.

Specific aims of this work include:

1) Developing electrochemical techniques to synthesize nanostructured TE materials (*e.g.* Bi_xTe_y and Pb_xTe_y) with controlled dimensions, surface morphologies and compositions

2) Investigating the growth mechanism of chalcogenide nanostructures for further synthesis of chalcogenide materials

3) Developing electrochemical techniques to synthesize nanostructured PV materials (*e.g.* Cd_xTe_y) with controlled dimensions, surface morphologies and compositions

4) Investigating the dimension, surface morphology and composition dependent electrical and optoelectrical properties

1.6 Thesis Organization

Following the Introduction, this dissertation is categorized into two parts. The first deals with electrochemical synthesis of TE materials (e.g. Bi_xTe_y and Pb_xTe_y), and the next part deals with the electrochemical synthesis of PV materials (Cd_xTe_y).

Within Part 1, chapters 2 and 3 describe the electrochemical synthesis of hierarchical Bi_xTe_y nanostructures and systematic investigation of the effect of experimental parameters (e.g. ratio of $[Bi^{3+}]/[HTeO_2^+]$ and type of sacrificial materials) on the nanostructures of the resulting materials. This is followed by an explanation for understanding their growth mechanisms. Chapters 4 and 5 represent the influence of the type and thickness of sacrificial thin films and reaction time on the synthesis of Bi and Te nanostructures. This work clearly demonstrates the possibility of synthesizing Te nanotubes via electrochemical methods that still provide effective control of their sizes. Chapter 6 highlights the fact that further Pb_xTe_y chalcogenide can be synthesized through electrochemical routes, and provides an understanding of their growth mechanism.

Part 2 explains the synthesis of cadmium chalcogenide, especially Cd_xTe_y as PV materials. Chapter 7 describes experiments conducted to functionalize SWNTs with CdTe NPs and evaluates their electrical and optoelectrical properties. In this chapter, it is shown that the size, surface morphology and composition of CdTe NPs/SWNT hybrid

nanostructures can be well controlled by adjusting the electrodeposition parameters. Chapter 8 introduces a new approach to chemically transform metals into compound semiconductors with nanostructures. In this section, metal substrates (e.g. Co) have been shown to be chemically transformed into Pb_xTe_y, Ag_xTe_y and Cd_xTe_y in each reaction step. Finally, chapter 9 summarizes the dissertation.

1.7 References

[1] EIA, Annual Energy Outlook 2010: With Projections to 2035 - EIA. Annual Energy Outlook 2010: p. 1-231.

[2] DOE, Basic Research Needs for Solar Energy Utilization (U.S. Department of Energy). BES Workshop and Technical Reports, 2005: p. 1-276.

[3] Rowe, D.M., CRC Handbook of Thermoelectrics. 1st edn. ed. 1995: CRC Press.

[4] Riffat, S.B. and X. Ma, Thermoelectrics: a review of present and potential applications. Applied Thermal Engineering, 2003. 23(8): p. 913-935.

[5] Alsema, E., Energy requirements of thin-film solar cell modules--a review. Renewable and Sustainable Energy Reviews, 1998. 2(4): p. 387-415.

[6] Chasmar, R.P. and R. Stratton, The Thermoelectric Figure of Merit and its Relation to Thermoelectric Generators. International Journal of Electronics, 1959. 7(1): p. 52 - 72.

[7] Shockley, W. and H.J. Queisser, Detailed balance limit of efficiency of p-n junction solar cells. Journal of Applied Physics, 1961. 32(3): p. 510-519.

[8] Bouroushian, M., Electrochemistry of Metal Chalcogenides. 1st edn. ed. Monographs in Electrochemistry, ed. F. Scholz. 2010: Springer.

[9] Snyder, G.J., et al., Disordered zinc in Zn4Sb3 with phonon-glass and electron-crystal thermoelectric properties. Nature Materials, 2004. 3(7): p. 458-463.

[10] Yoo, B.Y., et al., Electrochemically deposited thermoelectric n-type Bi2Te3 thin films. Electrochimica Acta, 2005. 50(22): p. 4371-4377.

[11] Dughaish, Z.H., Lead telluride as a thermoelectric material for thermoelectric power generation. Physica B-Condensed Matter, 2002. 322(1-2): p. 205-223.

[12] Tritt, T.M., Thermoelectric materials - Holey and unholey semiconductors. Science, 1999. 283(5403): p. 804-805.

[13] Maxwell, C.K., et al., Synthesis and characterization of cadmium telluride nanowire. Nanotechnology, 2008(32): p. 325711.

[14] Milan Paunovic, M.S., Fundamentals of Electrochemical Deposition. 2nd edn. ed. 2006: Wiley-Interscience.

[15] Xiao, F., et al., Synthesis of Bi2Te3 nanotubes by galvanic displacement. J. Am. Chem. Soc., 2007. 129(33): p. 10068-10069.

Part 1

Electrochemical Synthesis and Characterization of Chalcogenide Nanostructures: TE materials

Chapter 2

Electrochemical Synthesis of Bi_xTe_y Nanostructures

2.1 Abstract

Bi_xTe_y thin films synthesized by galvanic displacement were systematically investigated by observing open circuit potential (OCP), surface morphology, microstructure and film composition. Surface morphologies and crystal structures of synthesized Bi_xTe_y thin films were strongly depended on the type of the sacrificial materials (i.e., nickel (Ni), cobalt (Co) and iron (Fe)). Galvanically deposited Bi_xTe_y thin films from the sacrificial Ni and Co thin films exhibited Bi_2Te_3 intermetallic compounds and hierarchical structures with backbones and sub-branches. A linear relationship of deposited Bi content in Bi_xTe_y thin films as a function of $[Bi^{3+}]/[HTeO_2^{+}]$ ratio (within a range of less than 0.8) in the electrolyte was also observed. Surface morphologies of Bi_xTe_y thin films were altered with the film composition.

2.2 Introduction

Electrochemical techniques including electrodeposition, electroless (autocatalytic) deposition and galvanic displacement are widely used in printed circuit boards (PCB), semiconductor devices, integrated circuits, read/write heads, optical devices, sensors and other devices [1–3]. Electrodeposition is the process by which an ionized substance in liquid is deposited on an electrode (cathode) by the action of electricity (especially

electrolysis). Alternatively, electroless routes such as electroless deposition and galvanic displacement differ from electrodeposition because both processes are conducted without the use of an external voltage or current [3]. In electroless deposition, the reduction of the metal ions in solution can be carried out through the oxidation of a chemical compound, known as a reducing agent, present in the solution itself. Galvanic displacement (sometimes referred to as immersion plating or cementation) takes place when the redox potential of ametal ion in solution is more positive than that of the sacrificial material on the substrate [3]. Galvanic displacement differs from electroless deposition because a reducing agent necessary in electroless deposition is not required. In galvanic displacement, the sacrificial material behaves as a reducing agent. Electroless deposition and galvanic displacement are commonly referred to as chemical processes rather than electrochemical processes because of the absence of an external power supply, although the mechanisms can be explained using their electrochemical redox potentials. Galvanic displacement has been used to synthesize hollow nanostructures and to selectively deposit Cu and other metals onto Si in many devices such as integrated circuits, microelectromechanical systems (MEMS), and microchannel chemical reactors [3–7]. In addition to semiconductor metallization and nanoporous transmetallation, galvanic displacement has recently been studied as an efficient fabrication method for thermoelectric materials [8–11].

Thermoelectric devices convert thermal energy from a thermal gradient into electrical energy (the Seebeck effect), or vice versa (the Peltier effect), without any actuating parts [12–14]. The $(Bi,Sb)_2(Te,Se)_3$-based thermoelectric materials has been investigated by

many researchers because of various applications [12–25], which include microcoolers, power generation systems, infrared detectors, charge coupled device (CCD) cameras, laser diodes, microprocessors, thermocouples, blood analyzers, and portable picnic coolers. Among these thermoelectric materials, bismuth telluride (Bi_2Te_3) is considered one of the best materials for near room-temperature thermoelectric applications because of its superior ZT (the thermoelectric figure-of-merit) [12–14]. Bi_2Te_3 is a V2-VI3 compound semiconductor with narrow-band gap energy (0.11–0.15 eV at room-temperature). Also, n-type or p-type BiTe can be synthesized by slight modulation of the composition from its stoichiometric ratio [14].

Several different techniques including electrochemical processes (electrodeposition [12–14], galvanic displacement [11], electrochemical atomic layer epitaxy (ECALE) [26]) and vacuum processes (sputtering [27], evaporation [28,29], metal organic chemical vapor deposition (MOCVD) [30]) have been developed to synthesize Bi_xTe_y thin films. Among these methods, galvanic displacement is a simplistic and rapid deposition technique capable of tailoring surface morphology, crystal structure and composition by varying deposition conditions (e.g. sacrificial materials or compositions of electrolyte). Although extensive studies to synthesize thermoelectric BiTe alloys by other means have been conducted, the fabrication of BiTe alloys by galvanic displacement has not received significant attention, with previous work limited to synthesis of Bi_2Te_3 nanotubes [11].

In this chapter, the synthesis of Bi_xTe_y thin films by galvanic displacement was systematically investigated. The electrolyte composition and sacrificial materials were varied. Several sacrificial metallic films (Fe, Co, and Ni) were electrodeposited on

platinumcoated Ti/SiO2/Si substrates from chloride baths. Bi_xTe_y thin films were synthesized by galvanic displacement with these sacrificial thin films. Surface morphology, microstructure and composition of the galvanically deposited Bi_xTe_y thin films were studied and the growth mechanism was proposed.

2.3 Experimental Section

For electrodeposition and galvanic displacement reaction, the Pt(200 nm)/Ti(20 nm)/SiO_2(100 nm)/Si substrate was placed on a slide glass for mechanical support. The substrate was fixed using double-sided conductive copper tape (3 M, 1182a) for electrical contact during electrodeposition of the sacrificial layers. Pt (platinum) and Ti (titanium) were deposited on SiO_2/Si substrate by electron-beam evaporation process. Pt was used as a seed layer and Ti as an adhesion layer between Pt and SiO_2 layer. The entire sample including copper tape except an open area ($1.0cm^2$) at the middle of the substrate was insulated using a red mylar insulting tape and Microstop (Pyramid Plastic, Inc.). Sacrificial Ni, Co and Fe thin films with a thickness of ~3 μm were galvanostatically electrodeposited on the substrates from chloride baths. Table 2.1 lists bath compositions and operating conditions. Calcium chloride was used as a supporting electrolyte. l-ascorbic acid was added to prevent oxidation of Fe^{2+} in the electrolyte for electrodeposition of Fe thin films [31]. The solution pH was adjusted to 3.0 with HCl or NaOH. Electrodeposition was conducted using a Princeton Applied Research Potentiostat (VMP2) at current density of $5mAcm^{-2}$ and room-temperature without stirring. A

saturated calomel electrode (SCE) and platinum-coated titanium anode were used as a reference and a counter electrode, respectively.

Table 2.1. Bath compositions and operation conditions for electrodeposition of the sacrificial Ni, Co and Fe thin films on Pt/Ti/SiO_2/Si substrates.

Composition	Electrolyte	pH	Current density ($mA \cdot cm^{-2}$)	Temperature (^oC)	Agitation	Deposition rate ($\mu m \cdot hour^{-1}$)
Ni	1M $NiCl_2$+1M $CaCl_2$	3	5	RT	No	5.45
Co	1M $CoCl_2$+1M $CaCl_2$	3	5	RT	No	6
Fe	1M $FeCl_2$+1M $CaCl_2$+ 0.03M L-ascorbic acid	3	5	RT	No	7.2

Electrolyte compositions for galvanic displacement reactions are listed in Table 2.2. Bismuth nitrate [$Bi(NO_3)_3 \cdot 5H_2O$], tellurium oxide (TeO_2, 99.99%; Alfa Aesar) and nitric acid (HNO_3) were used to make the bath for galvanic displacement. The concentration of $HTeO_2^+$ was fixed at 10mMwith varying Bi^{3+} concentration from 2 to 20 mM to observe the dependence of solution $[Bi^{3+}]/[HTeO_2^+]$ ratio on film composition of Bi_xTe_y thin films. Nitric acid concentration was fixed at 1M and solution pH was maintained at pH 1. Electrodeposited thin films were dipped into the displacement electrolytes for 60 min. Open circuit potential (OCP) during galvanic displacement were measured in a three-electrode cell to monitor the effects of different sacrificial materials in the electrolytes.

Surface morphology and film composition of thin films obtained from electrodeposition and galvanic displacement were examined using a scanning electron microscope (SEM) (model: XL30-FEG, Phillips) and energy-dispersive spectroscopy

(EDS) (model: EDAX, Phoenix). An X-ray diffractometer (XRD) (model: D8 Advance Diffractometer, Bruker) with Cu Kα radiation (operating at 40 kV) was used for phase identification of the thin films. Samples were scanned from 20 to 80° with 0.02° increments and a 0.5 s collection time per increment.

Table 2.2. Bath compositions and operation conditions for galvanic displacement to synthesize Bi_xTe_y thin films.

Film composition	Electrolyte	Temperature (°C)	Agitation
Bi_xTe_y	$HTeO_2^+$: 10mM Bi^{3+}: 2mM~20mM HNO_3: 1M	RT	No

2.4 Results and Discussion

2.4.1 Effect of Ratio of $[Bi^{3+}]/[HTeO_2^+]$

Figure 2.1 shows surface morphologies of electrodeposited Ni, Co and Fe thin films on Pt/Ti/SiO_2/Si substrates from chloride baths. SEM images clearlyshowthat surface morphologies of the sacrificial thin films significantly depend on composition. Electrodeposited Ni thin films consisted of a needle-like features (Figure 2.1(a)), whereas electrodeposited Co thin film exhibited a granular structure with small and narrow needle-like structure (Figure 2.1(b)). On the other hand, the electrodeposited Fe thin film (Figure 2.1(c)) showed fine, dense and uniform feather-like structure. Kelcher et al. [31] and Myung et al. [32] reported that the surface morphology of Fe thin film

electrodeposited from chloride baths was influenced by current density and deposition temperature, respectively. Also, it was observed that the surface morphology of the electrodeposited Ni thin film in chloride bath was changed from powdery to smooth with an additive [33]. Myung et al. [32] and Park et al. [34] observed the effects of chemical composition in electrolyte on the surface morphology in FeCo and CoNi thin film alloys. No clear explanation to correlate electrodeposition parameters (solution pH, electrolyte composition, applied current density, operating temperature, and additive etc.) with surface morphology has been developed yet. Therefore, variation of surface morphologies according to the metal ion of each plating bath may be related to the different growth mechanism and crystal structures of each thin film in this study.

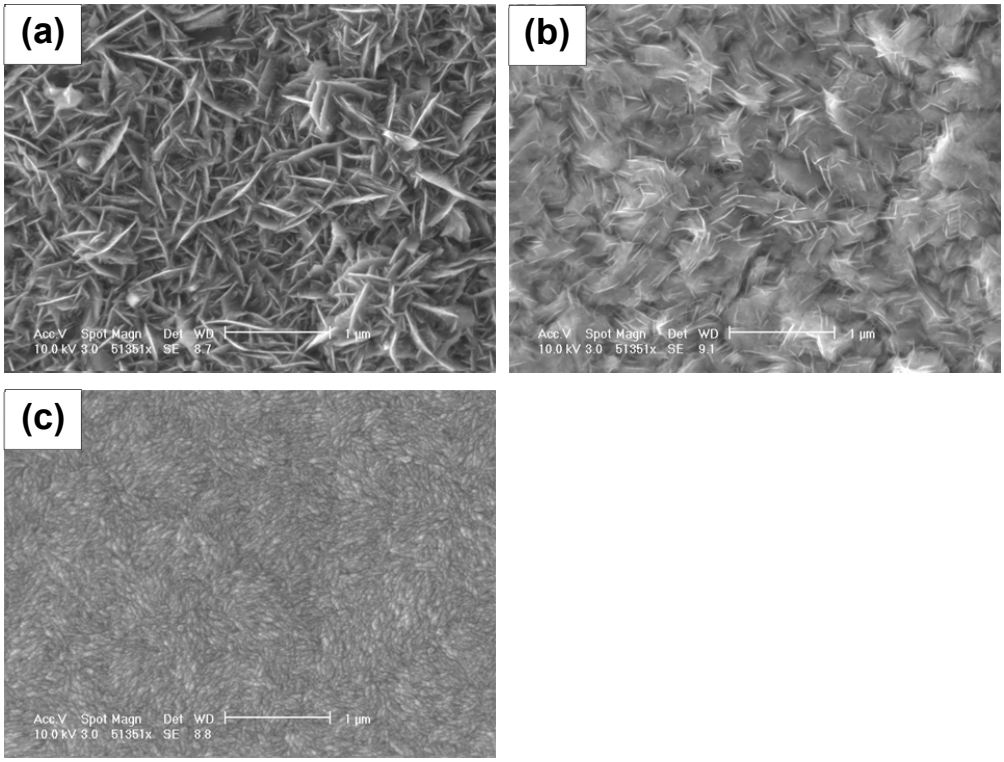

Figure 2.1. Surface morphologies of the sacrificial thin films electrodeposited from chloride baths: (a) Ni, (b) Co, and (c) Fe.

XRD analysis indicated that the electrodeposited Ni thin film consisted of the typical fcc (face-centered cubic) structure with (1 1 1), (2 0 0) and (2 2 0) planes (JCPDS No. 04-0850) as shown in Figure 2.2(a). (1 1 1) plane was the dominant phase in the electrodeposited Ni thin film. The electrodeposited Co (Figure 2.2(b)) exhibited fcc [(1 1 1) plane, JCPDS No. 15-0806] and hcp (hexagonal close packed) [(1 0 0), (0 0 2), (1 0 1) and (1 1 0) planes, JCPDS No. 05-0727] mixed structures. Both fcc (1 1 1) and hcp (1 1 0) phases were the dominant phases in the electrodeposited Co thin film. On the other hand, the electrodeposited Fe thin film (Figure 2.2(c)) was close to an amorphous phase as indicated by weak presence of bcc (body centered cubic) (1 1 0) structure (JCPDS No. 06-0696).

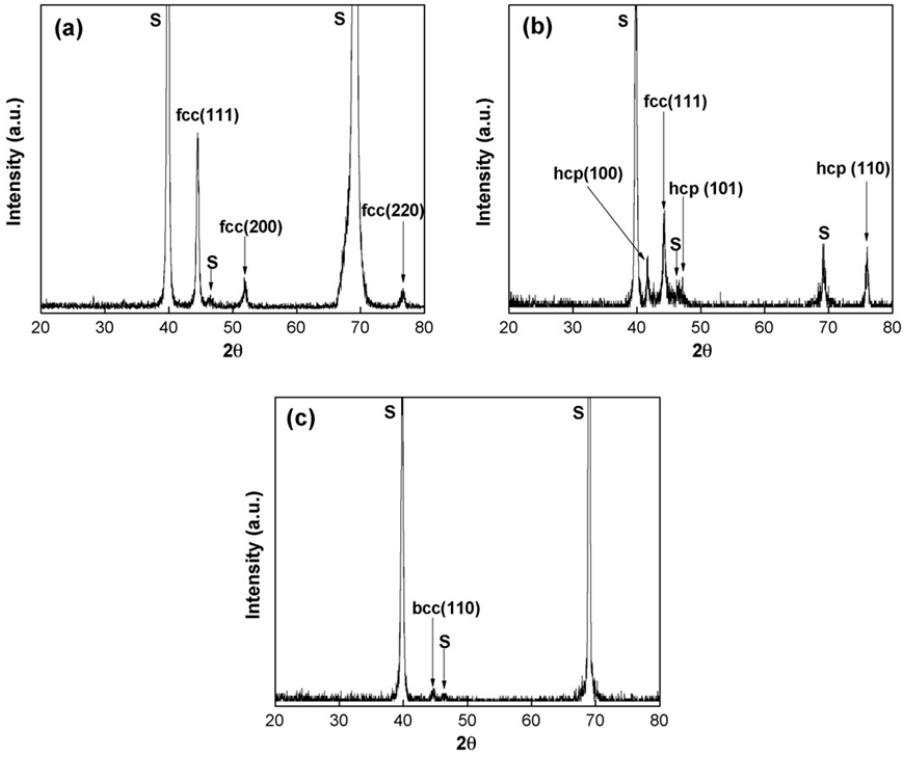

Figure 2.2. XRD patterns of the sacrificial thin films electrodeposited from chloride baths; (a) Ni, (b) Co, and (c) Fe. (S: substrate – Pt and Si)

The sacrificial thin films (Ni, Co and Fe) were immersed into the nitric acid baths containing 10 mM $HTeO_2^+$ +1 M HNO_3 with varying the concentrations of Bi^{3+} ions from 2 to 20 mM. The sacrificial thin films were galvanically displaced to form Bi_xTe_y thin films because of the difference in the redox potentials between the sacrificial thin films (i.e., Ni^{2+}/Ni^0: $E^0 = -0.257$ V vs. SHE, Co^{2+}/Co^0: $E^0 = -0.28$ V vs. SHE, and Fe^{2+}/Fe^0: $E^0 = -0.44$ V vs. SHE) and Bi^{3+} and/or $HTeO_2^+$ ions (i.e., Bi^{3+}, $HTeO_2^+/Bi_2Te_3$: $E^0 = -0.62$ V $-0.01475 \log [HTeO_2^+] + 0.0443[pH]$ vs. NHE) [11,12,35,36]. Using the sacrificial Co thin film, the dependence of film composition of Bi_xTe_y thin films on Bi^{3+} ion concentration in electrolyte was investigated and compared to previous reported data using Ni nanowires [11] (Figure 2.3). Only the sacrificial Co thin film was used to

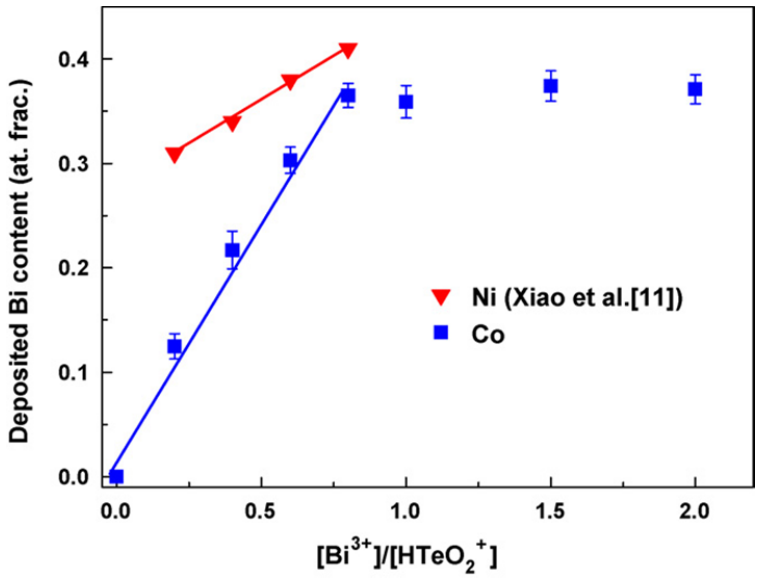

Figure 2.3. Dependence of the deposited Bi content in Bi_xTe_y thin films on ratio of $[Bi^{3+}]/[HTeO_2^+]$. Some error was found in Fig. 2 of the reference [11]. The error was revised as shown in Fig. 3 of this paper.

investigate the change of the chemical composition of Bi_xTe_y thin films because poor and porous Bi_xTe_y thin films were formed by galvanic displacement with the sacrificial Fe thin film. The galvanically deposited Bi content increased linearly from 0 to ~0.36 at.% with an increasing concentration ratio between Bi^{3+} and $HTeO_2^+$ in the electrolyte from 0 to 0.8, leveling off with the concentration ratio above 0.8. Xiao et al. [11] also observed a similar linear increase of the deposited Bi content with the sacrificial Ni nanowires in the range of $[Bi^{3+}]/[HTeO_2^+]$ ratios from 0.2 to 0.8. Therefore, the chemical composition of the galvanically deposited Bi_xTe_y thin films and nanotubes can be controlled by the concentration ratio of Bi^{3+} and $HTeO_2^+$ in the electrolyte.

The effect of the $[Bi^{3+}]/[HTeO_2^+]$ ratios on the surface morphologies and XRD patterns of Bi_xTe_y thin films are shown in Figures 2.4 and 2.5, respectively, using Co thin films as the sacrificial thin films. The Bi_xTe_y thin film (Figure 2.4(a) and (b)) displaced in the electrolyte containing 2 mM Bi^{3+} + 10 mM $HTeO_2^+$ +1 M HNO_3 produced a flower-like structure with the coexistence of Te and Bi_xTe_y peaks in the XRD pattern (Figure 2.5(a)] due to the relatively higher concentration of Te in the thin film, which measured to be $Bi_{0.63}Te_{4.37}$. Conversely, Bi_xTe_y thin films deposited from an electrolyte with 8 mM Bi^{3+} + 10 mM $HTeO_2^+$ +1 M HNO_3 displayed a granular structure with many needle-like shapes, as shown in Figure 2.4(c) and (d), with the chemical composition of Bi_xTe_y thin films measured near stoichiometric at $Bi_{1.83}Te_{3.17}$ from EDS analysis. From XRD analysis, only Bi_2Te_3 intermetallic peaks were observed as shown in Figure 2.5(b). Bi_xTe_y thin films deposited from the maximum $[Bi^{3+}]$, 20 mM Bi^{3+} + 10 mM $HTeO_2^+$ +1 M HNO_3, exhibited a similar granular structure with a chemical composition of $Bi_{1.86}Te_{3.14}$, but the

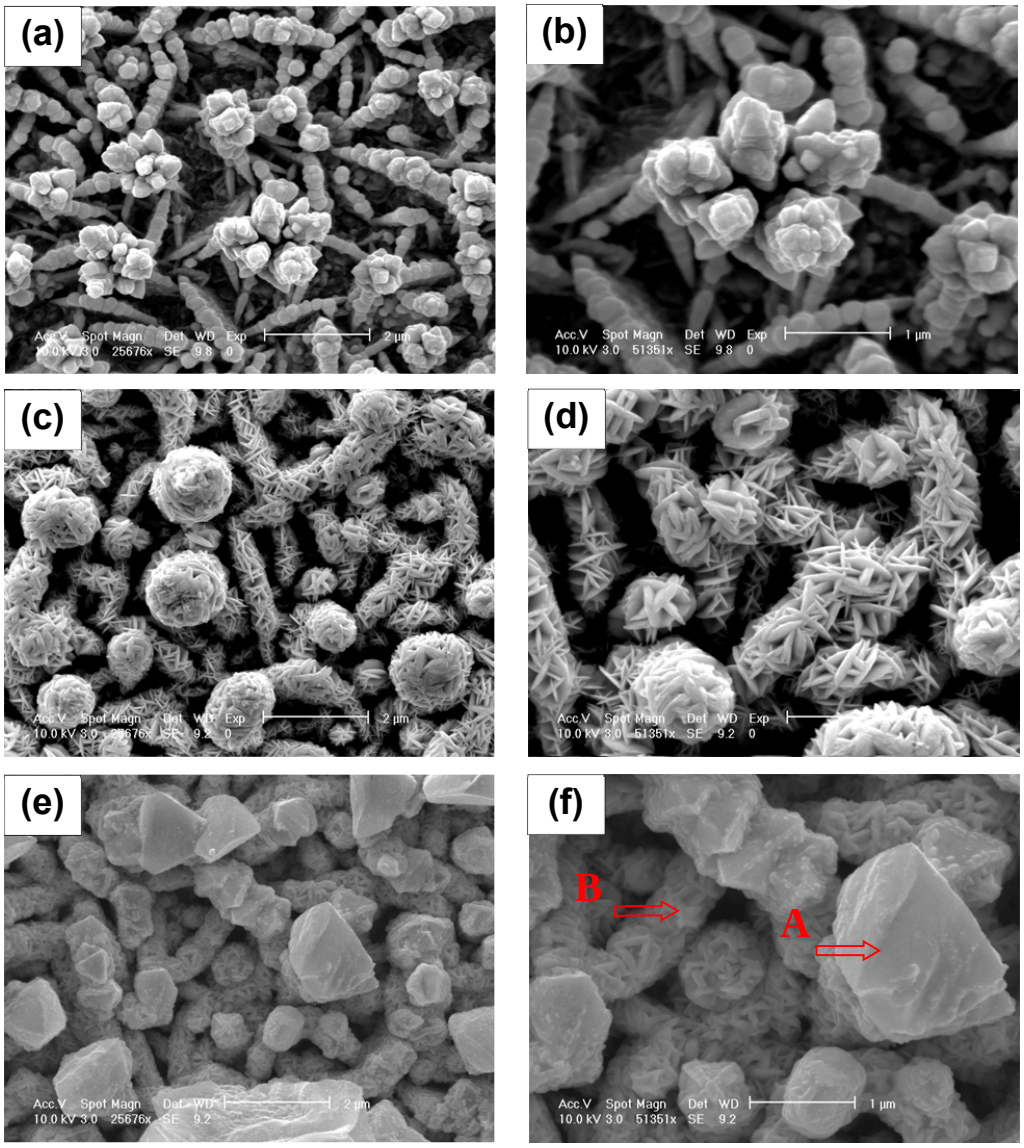

Figure 2.4. Surface morphologies of the galvanically deposited Bi_xTe_y thin films on the sacrificial Co substrates with ratio of $[Bi^{3+}]/[HTeO_2^+]$ in the electrolytes; (a) 0.2, low mag. (b) 0.2, high mag. (c) 0.8, low mag. (d) 0.8, high mag. (e) 2.0, low mag. and (f) 2.0, high mag. Concentrations of $HTeO_2^+$ and HNO_3 were fixed at 10 mM and 1M, respectively. The symbol "A" represents a cap part and "B" a stem part in Fig. 4(f).

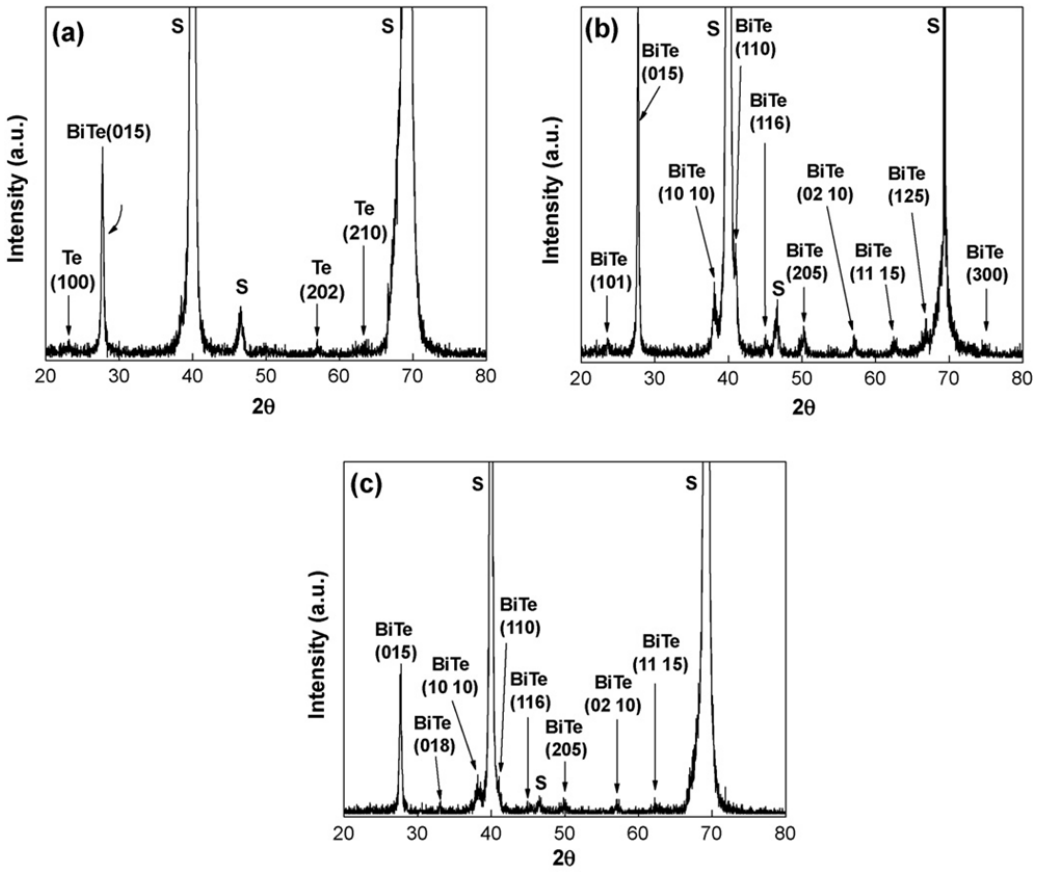

Figure 2.5. XRD patterns of the galvanically deposited Bi_xTe_y thin films with the ratio of $[Bi^{3+}]/[HTeO_2^+]$ in the electrolytes; (a) 0.2, (b) 0.8 and (c) 2.0. Cobalt thin films were used as the sacrificial thin films. (S: substrate – Pt and Si)

needle-like shapes were significantly decreased. However, within this sample a significant difference in the chemical composition between the cap part ($Bi_{1.13}Te_{3.87}$,marked with "A") and stem part ($Bi_{2.13}Te_{2.87}$, marked with "B") was observed as shown in Figure 2.4(f). This compositional disparity may have resulted from different diffusion length of metal ions between cap and stem parts. The cap portion of the granular structure has a shorter diffusion length with respect to the stem, allowing the mass transfer limited Te displacement reaction to predominate at the cap, reducing the

deposition rate at the surface of the stem.Martin-Gonzalez et al. [12] and Mori and Rajeshwar [37] suggested the possible deposition mechanism for BiTe, which occurs first by the reduction of $HTeO_2^+$ to Te on the electrode followed by the underpotential deposition (UPD) reaction of Bi^{3+} with the Te precursor in the well-known two-step deposition mechanism, having crucial effects on the composition of the alloy. Therefore, the Te content in the Bi_xTe_y thin film would be higher at the cap part than at the stem part of the nodular structure because the deposition rate of Te is faster than Bi^{3+} UPD reduction rate. This mechanism [12,37] is in good agreement with our results (Figure 2.4(f)). Therefore, it is reasonable that the overall Bi content of the granular structure deposited from the electrolyte containing relatively higher ratio of $[Bi^{3+}]/[HTeO_2^+]$ over 0.8 leveled off.

2.4.2 Electrochemical Study and Effect of Type of Sacrificial Materials

Open circuit potential (OCP) as a function of reaction time during galvanic displacement were measured to monitor the reaction between metal ions (Bi^{3+} and $HTeO_2^+$) in the electrolyte and sacrificial metal films (Ni, Co and Fe), as shown in Figure 2.6. The metal ion sources (Bi^{3+}: 6 mM and $HTeO_2^+$: 10 mM) were used to deposit the Bi_xTe_y intermetallic compound by galvanic displacement. By monitoring galvanic displacement reactions for 60 min, three different stages in the OCP curves were clearly observed for the Ni and Co thin films. The galvanically deposited Bi_xTe_y thin films with the sacrificial Ni, Co, and Fe thin films were synthesized at ~30 min (the slowest rate among the three sacrificial thin films), ~6min, and ~40 s, respectively. OCP curves

started from a negative potential at initial stage of galvanic displacement reaction due to negative redox potentials of the sacrificial materials as shown in Figure 2.6(b). In the case of nickel, the transient increase of OCP may be attributed to dissolution of native nickel oxide on the surface. Once the nickel oxide is dissolved by nitric acid, the OCP was shifted to negative value. A similar trend was also reported by Niwa et al. [38]. As the galvanic replacement reaction continued, the OCP remained at a steadystate value (step I represented in Figure 2.6(a) for the case of Ni) and sharply increased to positive values (step II) until completing the galvanic displacement reaction (step III). It was observed that the steady-state OCP values for Co thin film in step III is approximately 100mV higher than that for Ni and Fe thin films in Figure 2.6(a). The mixed potential theory has been proposed by following equation [39]:

$$\Delta E(OCP)=\left(\frac{kT}{e}\right)\left(\frac{\Delta j_C}{j_A}\right) \quad (1)$$

where k is the Boltzmann constant, T is the absolute temperature, e is the electric charge of the electron, and j_C and j_A are the anodic and cathodic exchange current densities, respectively. Based on this theory, the rapid change of potential in step II can be explained by increasing in cathodic current (j_C) due to reduction of Bi^{3+} and/or $HTeO_2^+$ ions. Since the steady-state OCP values for Co thin film in step III is approximately 100mV higher than that for Ni and Fe thin films, the reduction rate may be much faster than oxidation rate (dissolution of sacrificial materials) for Co thin film. This trend may

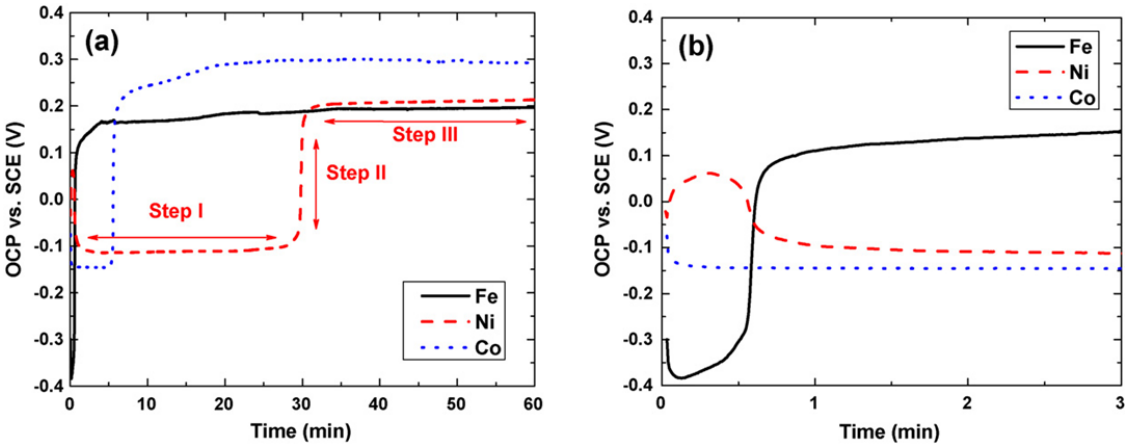

Figure 2.6. Open circuit potentials as a function of time for galvanic displacement reaction with the sacrificial thin films (Ni, Co and Fe): (a) overall OCP curves and (b) initial stages (within 3 minutes) of OCP curves. Solid, dash, and dotted lines represent Fe, Ni, and Co thin films, respectively.

be attributed to faster reduction rate than dissolution rate for Co thin film. Once the sacrificial thin films were completely displaced by Bi_xTe_y thin films, the OCP was stable with a value >0V vs. SCE (step III, mixed potential between Bi^{3+} and $HTeO_2^+$ ions in the electrolyte and the deposited Bi_xTe_y thin film). The negative potentials of step I in OCP curves indicate the mixed potentials between reduction of Bi^{3+} and $HTeO_2^+$ ions in the electrolyte and oxidation of the sacrificial metal thin films. The driving force for the galvanic displacement reaction is the difference of the redox potentials between $Bi^{3+}$and/or $HTeO_2^+$ ions in the electrolyte and the sacrificial metal thin films [11,12,35,36]. As expected, the average mixed potentials for Ni, Co, and Fe thin films at step I were −0.113, −0.145, and −0.358 V, respectively, which is in same sequence as redox potential of the sacrificial thin films. The more the available surface area of the sacrificial thin films for the galvanic displacement reaction decreases, the more the local

anodic current of the sacrificial thin films decreases. It may result in a shift of potential value toward a more positive value during step II. After the Bi_xTe_y compound formed on the entire surface area of the sacrificial thin film, the potential may reach to a steady-state (step III).

After finishing galvanic displacement reaction with the sacrificial metal thin films for 60 min, surface morphologies and XRD patterns for the galvanically synthesized Bi_xTe_y thin films were shown in Figures 2.7 and 2.8, respectively. It was revealed from XRD analysis (Figure 2.8(a) and (b)) that Bi_xTe_y thin film consists of peaks of Bi_2Te_3 intermetallic compound (JCPDS No. 15-0863). The galvanically synthesized Bi_xTe_y thin films from the electrodeposited sacrificial Ni and Co thin films show a very unique hierarchical structure with backbones and sub-branches, as shown in Figure 2.7(a)–(d). Li et al. [13] reported the formation of Bi_2Te_3 intermetallic compound with novel hierarchical nanostructures fabricated by electrodeposition process from the electrolyte containing $Bi(NO_3)_3$, Na_2TeO_3, tartaric acid, and HNO_3. They electrodeposited the Bi_2Te_3 intermetallic compound on a copper foil substrate. They suggested the possible mechanism for the formation of hierarchical Bi_2Te_3 nanostructures as the following three steps; first, formation of backbones followed by formation of original branches on backbones, and finally formation of sub-branches on original branches. The mechanism suggested by Li et al. [13] could be accepted as a possible mechanism for formation of Bi_xTe_y structures synthesized by galvanic displacement in this study. Also they suggested that formation of nanosheets of Bi_2Te_3 intermetallic compounds strongly depend on concentration of Bi and Te ions in electrolyte; the concentration of $Bi(NO_3)_3$ should be

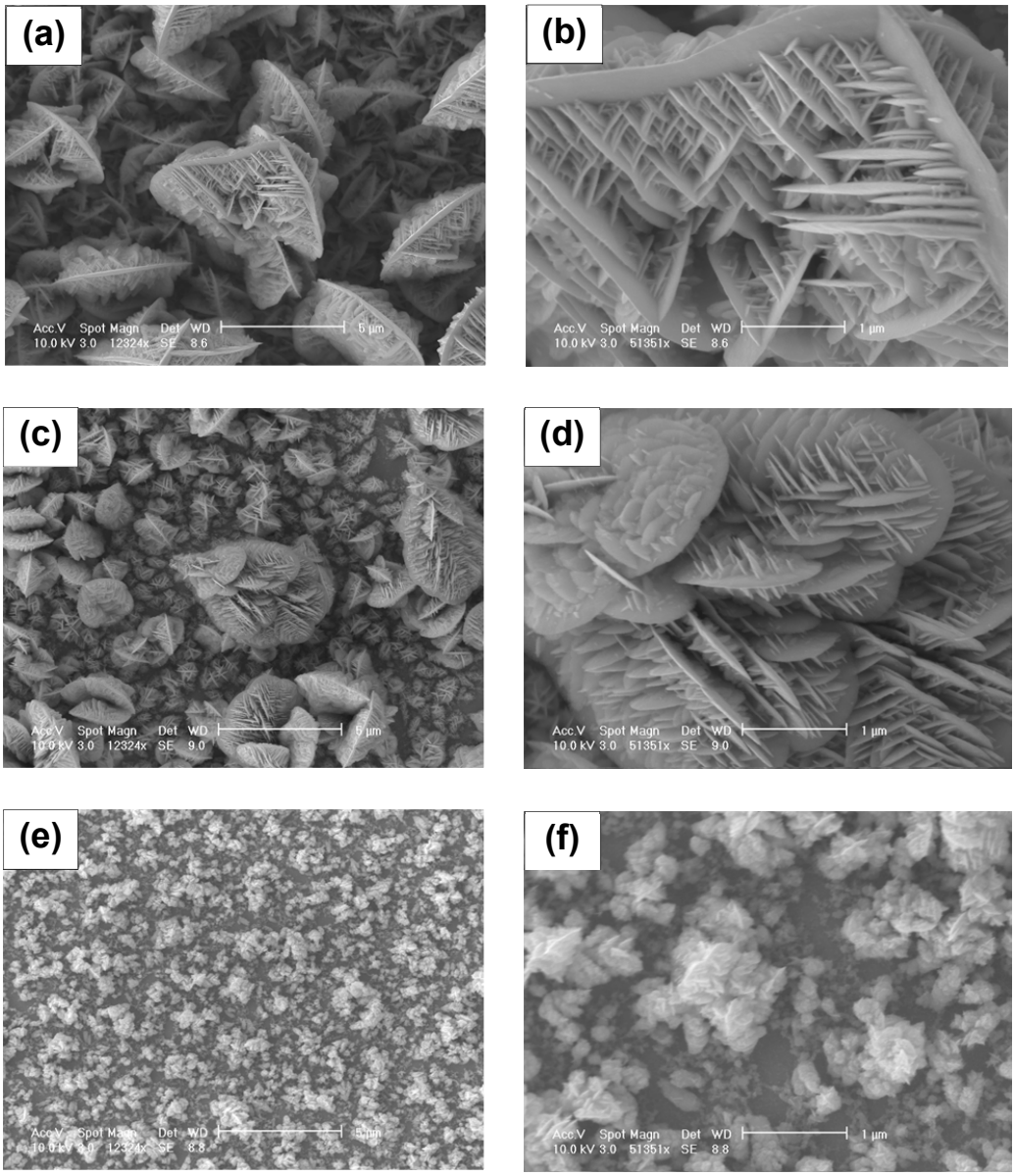

Figure 2.7. Surface morphologies of the galvanically deposited Bi_xTe_y thin films with sacrificial metal thin films of (a) Ni, low mag. (b) Ni, high mag. (c) Co, low mag. (d) Co, high mag. (e) Fe, low mag. and (f) Fe, high mag.

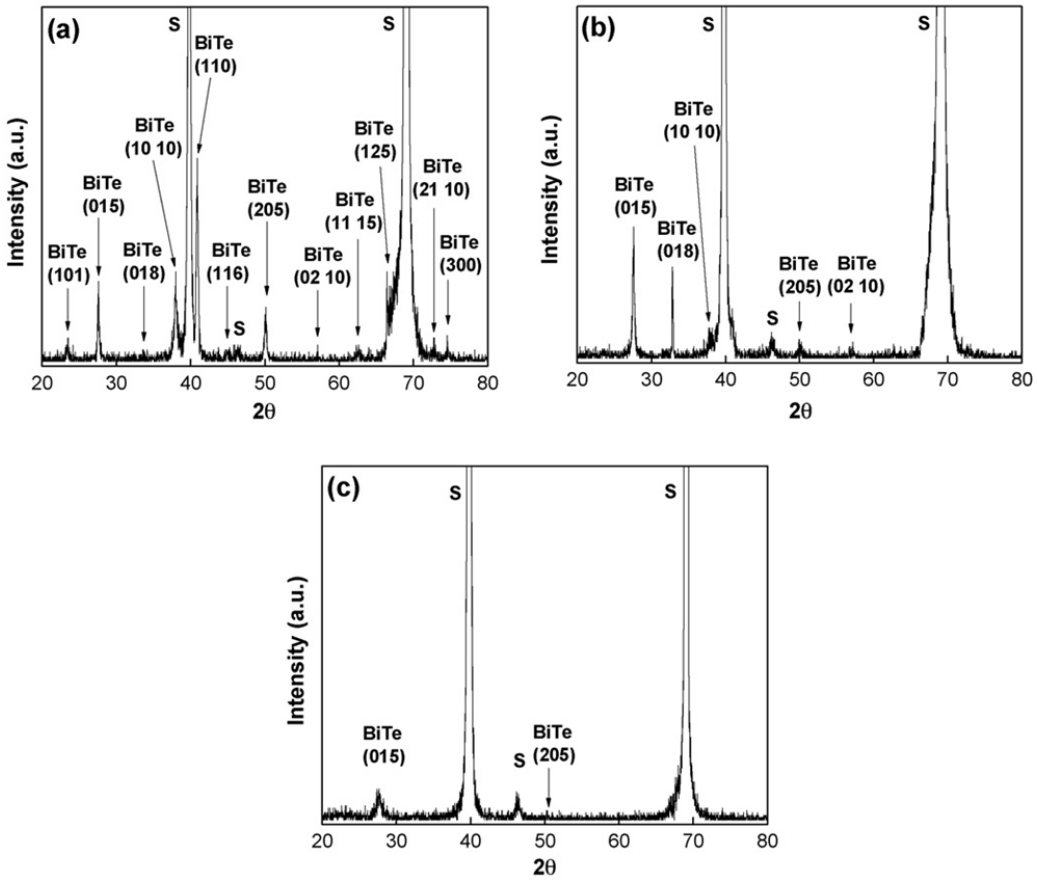

Figure 2.8. XRD patterns of the gavanically synthesized Bi_xTe_y thin films with the sacrificial (a) Ni, (b) Co, and (c) Fe thin films. (S: substrate – Pt and Si)

smaller than that of Na_2TeO_3 in the deposition solution to obtain nanosheets of Bi_2Te_3 intermetallic compounds. Figure 2.9 represents the possible growth mechanism of hierarchical Bi_xTe_y nanostructures by galvanic displacement reaction. It is expected that Bi_xTe_y nuclei initially formed on sacrificial thin film (Figure 2.9(a)), followed by growth of Bi_xTe_y nuclei to form a spindle-shaped Bi_xTe_y (referred to backbone) with a few branches (Figure 2.9(b)). Spindle-shaped backbones with additional sub-branches

continuously grow until complete coverage or displacement of sacrificial film (Figure 2.9(c)).

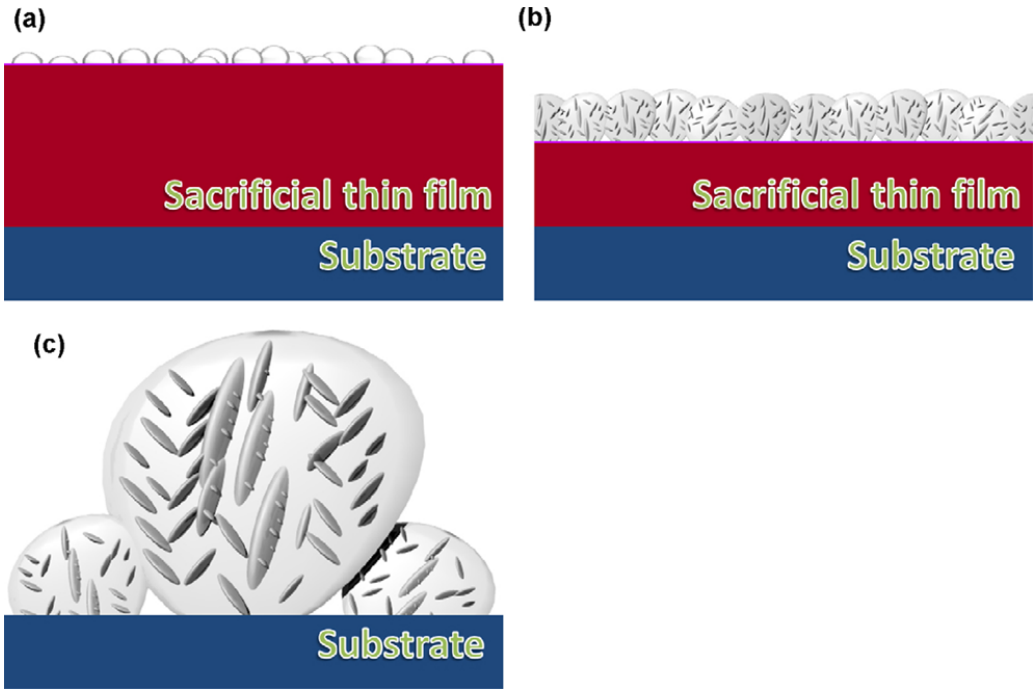

Figure 2.9. Schematic illustration (not to scale) of possible growth mechanism for galvanic displacement reaction. Hierarchical Bi_xTe_y nanostructures may be synthesized as follows; (a) formation of Bi_xTe_y nuclei on the overall sacrificial thin film, (b) formation of a spindle-shaped Bi_xTe_y (referred to a backbone) and initial branches on backbones, and (c) growth of the backbones and initial branches, and formation of the sub-branches (secondary branches) on initial branches for hierarchical structure.

The hierarchical structure of Bi_2Te_3 intermetallic compound was not observed for the galvanically synthesized Bi_xTe_y thin films (Figure 2.7(e) and (f)) from the sacrificial Fe thin films. The absence of the hierarchical structure in Figure 2.7(e) and (f) may be a consequence of the fast chemical dissolution rate of the sacrificial Fe thin film as shown

in the OCP curve in Figure 2.6. The surface morphology of the galvanically synthesized Bi_xTe_y thin film with the electrodeposited Fe thin film has a very fine granular structure.

It is clear from XRD analysis (Figure 2.8(a) and (b)) that the galvanically deposited Bi_xTe_y thin films with the sacrificial Ni and Co thin films exhibit the XRD patterns of Bi_2Te_3 intermetallic compound with a rhombohedral structure (JCPDS No. 15-0863). However, only some peaks of the Bi_2Te_3 intermetallic compound were observed in the galvanically deposited Bi_xTe_y thin films with the sacrificial Fe thin films, which probably result from the fast dissolution rate of the sacrificial Fe thin film. Since the microstructure of Bi_xTe_y intermetallic compound may strongly depend on the type of sacrificial materials, the sacrificial materials effect on the formation of hierarchical Bi_2Te_3 structures is an area that merits further study.

2.5 Conclusions

Bi_xTe_y thin films were synthesized by galvanic displacement with three sacrificial thin films (Ni, Co and Fe). The sacrificial Ni, Co and Fe thin films were electrodeposited on Pt/Ti/SiO_2/Si substrates at room-temperature without stirring. Based on OCP measurements, galvanic displacement reactions were monitored as follows; (i) redox reactions occurred simultaneously between the targeted materials (Bi_xTe_y) and the sacrificial metal thin films (Ni, Co and Fe), (ii) the values of the OCP shifted toward more positive values as the available surface area for galvanic displacement decreased, and (iii) the potentials remained at positive and constant values after the redox reaction had finished. Surface morphologies and crystal structures of the as-synthesized thin films

by galvanic displacement strongly depend on the types of the sacrificial materials. Bi_xTe_y thin films were successfully deposited using all the three sacrificial thin films.

A linear relationship for the deposited Bi content in Bi_xTe_y thin films as a function of $[Bi^{3+}]/[HTeO_2^{+}]$ ratio (within the range of less than 0.8) in the electrolyte was observed. Additionally, the surface morphologies of Bi_xTe_y thin films were shown to strongly depend on the chemical composition ratio and the sacrificial thin films. Bi_xTe_y thin films exhibited completely different surface morphologies compared to those of the sacrificial thin films. Specially, the hierarchical structures with backbones and sub-branches were obtained in Bi_xTe_y thin films galvanically synthesized with the sacrificial Ni and Co thin films.

2.6 References

[1] G. Oskam, J.G. Long, A. Natarajan, P.C. Searson, J. Phys. D: Appl. Phys. 31 (1998) 1927.

[2] L.T. Romankiw, T.A. Palumbo, in: L.T. Romankiw, D.R. Turner (Eds.), Electrodeposition Technology, Theory and Practice, The Electrochemical Society, Pennington, NJ, 1988, p. 13.

[3] C. Carraro, R. Maboudian, L. Magagnin, Surf. Sci. Rep. 62 (2007) 499.

[4] J.G.A. Brito-Neto, S. Araki, M. Hayase, J. Electrochem. Soc. 153 (2006) C741.

[5] H. Cachet, M. Froment, E. Souteyrand, C. Dennig, J. Electrochem. Soc. 139 (1992) 2920.

[6] C. Carraro, L. Magagnin, R. Maboudian, Electrochim. Acta 47 (2002) 2583.

[7] A.T. Carvalho, A.P. Nascimento, L.M. Silva, M.L.P. Silva, J.C. Madaleno, L. Pereira, Adv. Mater. Forum. III (Pts 1 and 2) (2006) 1328.

[8] V. Bansal, H. Jani, J.D. Plessis, P.J. Coloe, S.K. Bhargava, Adv. Mater. 20 (2008) 717.

[9] M.R.H. Nezhad, M. Aizawa, L.A. Porter Jr., A.E. Ribbe, J.M. Buriak, Small 1 (2005) 1076.

[10] Y.G. Sun, Chem. Mater. 19 (2007) 5845.

[11] F. Xiao, B.Y. Yoo, K.-H. Lee, N.V. Myung, J. Am. Chem. Soc. 129 (2007) 10068.

[12] M.S. Martin-Gonzalez, A.L. Prieto, R. Gronsky, T. Sands, A.M. Stacy, J. Electrochem. Soc. 149 (11) (2002) C546.

[13] G.-R. Li, F.-L. Zheng, Y.-X. Tong, Cryst. Growth Des. 8 (4) (2008) 1226.

[14] B.Y. Yoo, C.-K. Huang, J.R. Lim, J. Herman, M.A. Ryan, J.-P. Fleurial, N.V. Myung, Electrochim. Acta 50 (2005) 4371.

[15] B. Mayers, Y. Xia, J. Mater. Chem. 12 (2002) 1875.

[16] B. Mayers, Y. Xia, Adv. Mater. 14 (2002) 279.

[17] U.K. Gautam, C.N.R. Rao, J. Mater. Chem. 14 (2004) 2530.

[18] Y.J. Zhu, W.W. Wang, R.J. Qi, X.L. Hu, Angew. Chem. 116 (2004) 1434.

[19] H. Yu, P.C. Gibbons, W.E. Buhro, J. Mater. Chem. 14 (2004) 595.

[20] M. Mo, J. Zeng, X. Liu, W. Yu, S. Zhang, Y. Qian, Adv. Mater. 14 (2002) 1658.

[21] Z. Liu, S. Li, Y. Yang, Z. Hu, S. Peng, J. Liang, Y. Qian, New J. Chem. 27 (2003) 1748.

[22] G. Xi, Y. Peng, W. Yu, Y. Qian, Cryst. Growth Des. 5 (2005) 325.

[23] Q. Lu, F. Gao, S. Komarneni, Adv. Mater. 16 (2004) 1629.

[24] Q. Lu, F. Gao, S. Komarneni, Langmuir 21 (2005) 6002.

[25] Z. He, S.H. Yu, J. Zhu, Chem. Mater. 17 (2005) 2785.

[26] W. Zhu, J.Y. Yang, J. Hou, X.H. Gao, S.Q. Bao, X.A. Fan, J. Electroanal. Chem. 585 (2005) 83.

[27] C. Shafai, M.J. Brett, J. Vac. Sci. Technol. A 15 (1997) 2798.

[28] H. Zou, D.M. Powe, G. Min, J. Vac. Sci. Technol. A 19 (2001) 899.

[29] H. Zou, D.M. Powe, G. Min, J. Cryst. Growth 222 (2001) 82.

[30] R. Venkatasubramanian, T. Colpitts, E. Watko, M. Lamvik, N. El-Masry, J. Cryst. Growth 170 (1997) 817.

[31] S. Kelcher, B.-Y. Yoo, D.-Y. Park, N.V. Myung, Plat. Surf. Finish. 92 (1) (2005) 24.

[32] N.V. Myung, D.-Y. Park, D.E. Urgiles, T. George, Electrochim. Acta 49 (2004) 4397.

[33] D.-Y. Park, R.Y. Song, J.M. Ko, B.Y. Yoo, N.V. Myung, Electrochem. Solid-State Lett. 8 (2005) C23.

[34] D.-Y. Park, N.V. Myung, M. Schwartz, K. Nobe, Electrochim. Acta 47 (2002) 2893.

[35] D.R. Lide, CRC Handbook of Chemistry & Physics, CRC Press, Cleveland, OH, 2006.

[36] F. Xiao, B.Y. Yoo, M.A. Ryan, K.H. Lee, N.V. Myung, Electrochim. Acta 52 (2006) 1101.

[37] E. Mori, K. Rajeshwar, J. Electroanal. Chem. 258 (1989) 415.

[38] D. Niwa, N. Takano, T. Yamada, T. Osaka, Electrochim. Acta 48 (2003) 1295.

[39] M. Chemla, T. Homma, V. Bertagna, R. Erre, N. Kubo, T. Osaka, J. Electroanal. Chem. 559 (2003) 111.

Chapter 3

Growth Mechanism of Hierarchical Bi_xTe_y Nanostructures

3.1 Abstract

We demonstrated a three-step growth mechanism for hierarchical growth of Bi_xTe_y thin films on sacrificial Co thin films via galvanic displacement reaction between sacrificial materials and metal ions (Bi^{3+} and $HTeO_2^+$). This systematic investigation clearly exhibited nucleation and growth stages of Bi_xTe_y nanostructures as function of reaction time.

3.2 Introduction

Chalcogenide materials (*e.g.* Bi_2Te_3, PbTe, CdTe, CdS, etc.) have been attracting extensive attention due to their thermoelectric and optoelectric properties that have a large range of potential applications in thermoelectric and solar cell devices [1-5]. Among these materials, bismuth telluride (Bi_2Te_3) holds great promise for its thermoelectric applications at near-room temperature because of its superior ZT (the thermoelectric figure-of-merit) [6-8]. Among the various methods that have recently been reported for synthesis of Bi_2Te_3 nanostructures, galvanic displacement reaction is one of the most cost-effective, simple, and versatile approaches compared to the conventional method [1-2,8-12]. Since galvanic displacement reaction occurrs due to the difference in redox potential between materials, a more noble metal is reduced and deposited on the substrates while sacrificial materials itself is oxidized [14]. Using this method, our group

synthesized thin films, nanowires, and nanotubes composed of chalcogenide materials such as Bi_xTe_y by galvanic displacement from sacrificial iron group (*e.g.* Ni, Co and Fe) [10-12]. Detailed growth or reaction mechanisms have not yet been reported, and thus, systematic investigation of growth mechanism during the galvanic displacement reaction is a great merit for further study.

In this chapter, we report the three-step growth mechanism of galvanically synthesized Bi_xTe_y thin films with hierarchical nanostructures on sacrificial Co thin films. By analyzing open circuit potential (OCP) during the galvanic displacement reaction, the growth mechanism can be described as a nucleation stage of Bi_xTe_y thin films on the sacrificial Co thin films, followed by a transition to the formation of initial Bi_xTe_y nanostructures, and ending with various growth stages of hierarchical nanostructures. Characterization studies of their composition, morphology and crystal structures support this three-step growth mechanism.

3.3 Experimental Section

Sacrificial Co thin films with a thickness of ~3μm were prepared by galvanostatic electrodeposition on the Pt(200nm)/Ti(20nm)/SiO_2(100nm)/Si substrates. The electrolyte consists of 1M $CoCl_2$ and 1M $CaCl_2$. Calcium chloride was used as a supporting electrolyte. The solution pH was adjusted to 3.0 with HCl or NaOH. Electrodeposition was conducted using a Princeton Applied Research Potentiostat (VMP2) at current density of 5 mA cm^{-2} at room temperature without stirring. For the electrodeposition, a

saturated calomel electrode (SCE) and platinum-coated titanium anode were used as a reference and a counter electrode, respectively.

Bismuth nitrate [$Bi(NO_3)_3 \bullet 5H_2O$], and nitric acid (HNO_3) were purchased from Fisher Scientific; tellurium oxide (TeO_2, 99.99%) was purchased from Alfa Aesar. Both chemicals were used to make the bath for galvanic displacement. In s typical synthesis of hierarchical Bi_xTe_y thin films by galvanic displacement, the concentration of Bi^{3+}, $HTeO_2^+$, and HNO_3 was fixed at 6 mM and 10 mM and 1M, respectively. The pH of the electrolyte was maintained at 1. Once the sacrificial Co thin films were prepared, the substrates were dipped into the displacement electrolyte for 60 min. Then, open circuit potential (OCP) was measured in a three-electrode cell during galvanic displacement reaction. In order to investigate the growth mechanism, each sample was taken out from the electrolyte at the different reaction time.

Film compositions of thin films prepared by electrodeposition and galvanic displacement were examined using energy-dispersive spectroscopy (EDS, EDAX, Phoenix). Surface morphology and cross-sectional images were obtained by a scanning electron microscope (SEM, XL30-FEG, Phillips). A X-ray diffractometer (XRD, D8 Advance Diffractometer, Bruker) with Cu Kα radiation (operating at 40kV) was used to record the patterns from 100 to 800 with 0.020 increments and a 0.5 s collection time per increment.

3.4 Results and discussion

Figure 3.1. illustrates the three-step growth mechanism of galvanically synthesized Bi_xTe_y thin films with hierarchical nanostructures on the sacrificial Co thin films. As depicted in Figure 3.1, Bi_xTe_y nuclei are initially formed on the sacrificial Co thin films by oxidation of Co and reduction of metal ions (Bi^{3+} and $HTeO_2^+$) simultaneously. These nuclei are then grown to form a star-shapeed Bi_xTe_y mass with a few branches, followed by continuous growth of this nanostructure until it becomes spindle-shape Bi_xTe_y nanostructures.

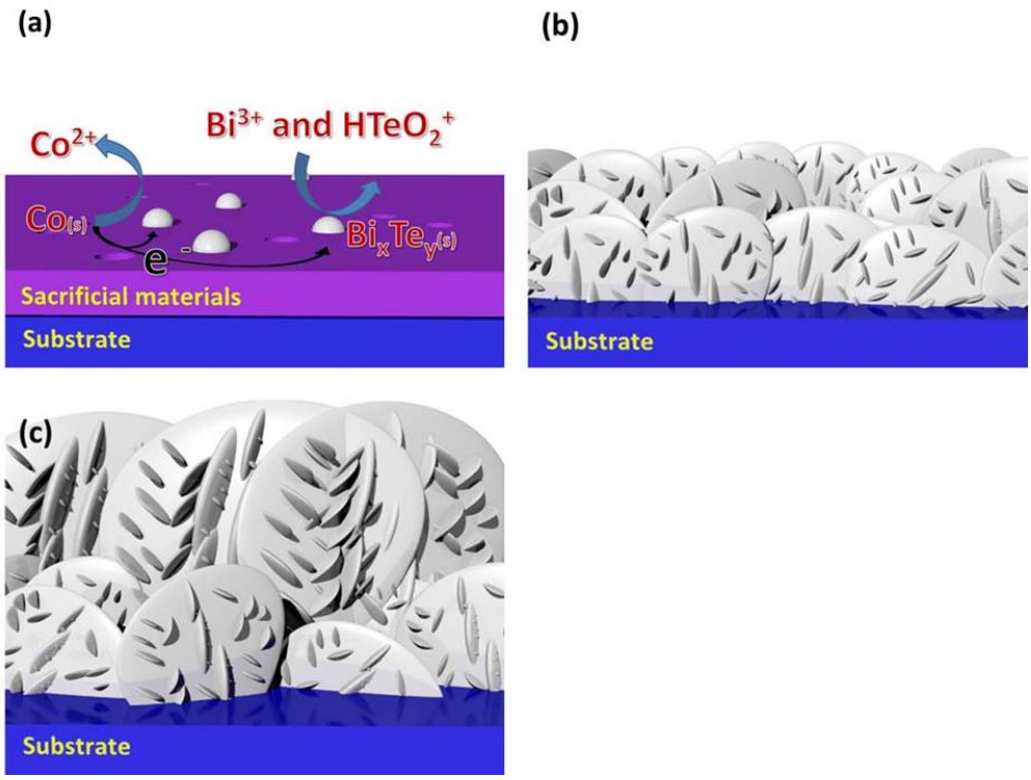

Figure 3.1. Schematic diagram of the three-step growth mechanism of galvanically synthesized Bi_xTe_y nanostructures on sacrificial Co thin films

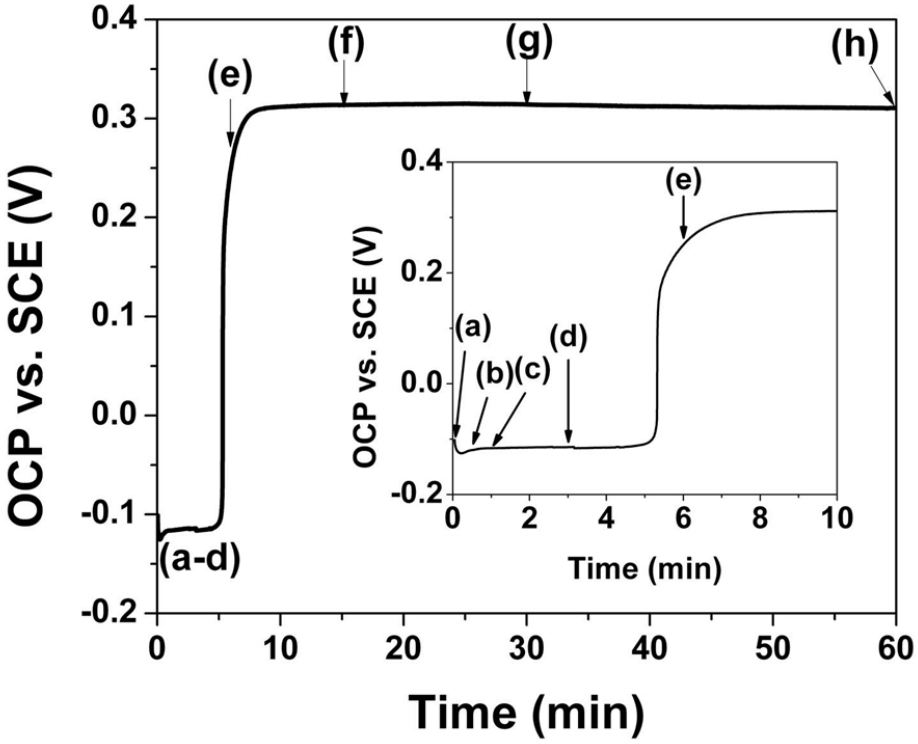

Figure 3.2. Open circuit potentials for galvanic displacement reaction on the sacrificial Co thin films as a function of time at (a) 0, (b) 0.5, (c) 1, (d) 3, (e) 6, (f) 15, (g) 30, and (h) 60 min, respectively. Insert figure represents initial stage of OCP curve within 10 min.

Figure 3.2 shows the changes of OCP as a function of reaction times during galvanic displacement with 6 mM Bi^{3+} + 10 mM $HTeO_2^+$ + 1 M HNO_3 for 1 h. These changes clearly indicate the three reaction steps as on the reaction progresses. In the first step, the galvanic reaction starts from the region of steady-negative potential, followed by rapid change in potential toward positive in the second step. Finally, the potential reaches another steady-positive potential at the third step. These three reaction steps can be explained by an interpretation of the reaction mechanisms. Once the metal ions (Bi^{3+} and $HTeO_2^+$) begin to galvanically form on sacrificial cobalt films at initial step (~ 3min), the

OCP shifts in the negative direction which represents the mixed potential of the oxidation of Co^{2+}/Co^{0} (−0.28V vs. SHE) and the reduction of Bi^{3+}, $HTeO_2^{+}/Bi_2Te_3$ (−0.62V −0.01475 log[$HTeO_2^{+}$] + 0.0443[pH] vs. SHE) [14]. The sharp increase of potential in the second step (between 3 and 15 min) is due to an increase in cathodic current (reduction: Bi^{3+}, $HTeO_2^{+}/Bi_2Te_3$) as a growth of Bi_xTe_y nuclei and decrease of anodic current (oxidation: Co^{0}/Co^{2+}) caused by covering Bi_xTe_y thin film on sacrificial Co thin films. The steady-positive potential at third step (after 15 min) indicates that deposition process completely changes from the nucleation stage to the growth stage.

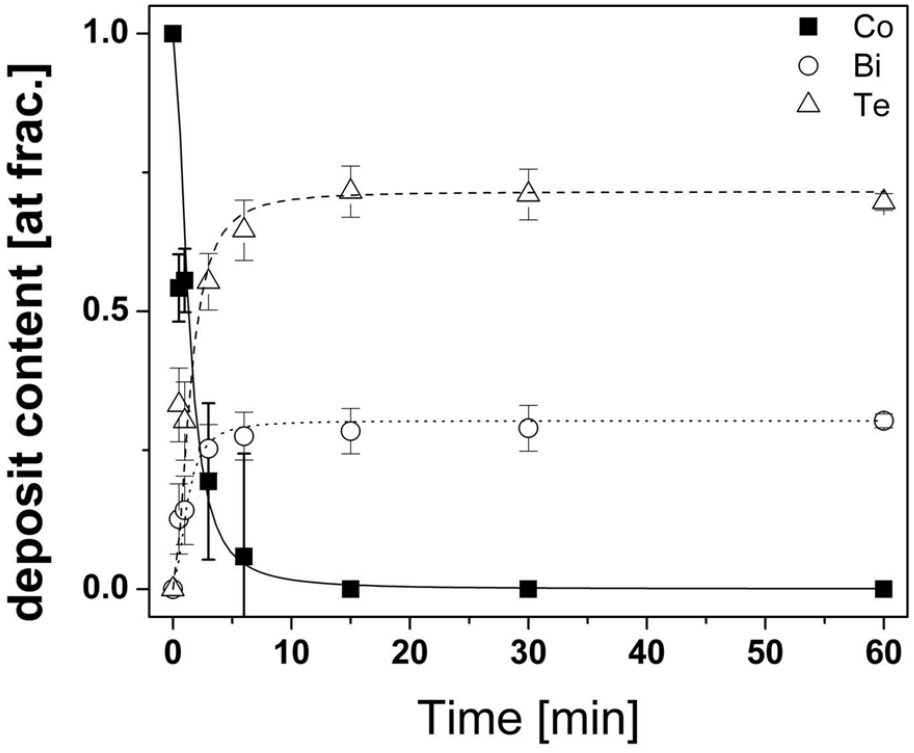

Figure 3.3. The content of sacrificial cobalt (solid square and line) thin films, and as-deposited bismuth (open circle and dot line) and tellurium (open triangle and dash line) on Bi_xTe_y thin films as a function of the reaction time, respectively.

To elucidate the detailed mechanism of formation, the content of sacrificial cobalt substrate and as-deposited bismuth and tellurium on the Bi_xTe_y thin films was characterized by EDS at 0.5, 1, 3, 6, 15, 30, and 60 min, respectively, as indicated in Figure 3.2. This analysis confirms that the amount of sacrificial cobalt substrate dramatically decreased in the first step (~3 min), as shown in Figure 3.3. We conjecture that the dissolution (oxidation) of sacrificial Co thin films in the 1M nitric acid is very fast, and this provides the electrons necessary for the formation of Bi_xTe_y nuclei (reduction) on sacrificial Co thin films. Afterwards, the content of sacrificial Co decreases continuously until it reached to zero in second step (between 3 and 15 min). As the sacrificial material decreases, the content of as-deposited bismuth and tellurium rapidly increases in the first and second step (~15 min). Once all the sacrificial cobalt are reacted with metal ions, eventually no increase in the amount of Bi and Te deposit ($Bi_{1.5}Te_{3.5}$) is observed in third step (15 ~ 60 min). This indicates that the galvanic displacement reaction proceeds up to 15 min, and then terminates spontaneously. This is in good agreement with the previous explanation of three reaction steps in OCP analysis.

Subsequently, the effects of reaction time on the surface morphology of as-synthesized Bi_xTe_y thin films were investigated. Figure 3.4. shows typical SEM images of electrodeposited Co on substrate and galvanically deposited Bi_xTe_y thin films on the sacrificial Co thin films at different reaction time. The surface morphology of the sacrificial Co thin films exhibits a granular structure with small and narrow needle-like structure as shown in Figure 3.4(a). On the other hand, Figure 3.4(b)-(h) shows that

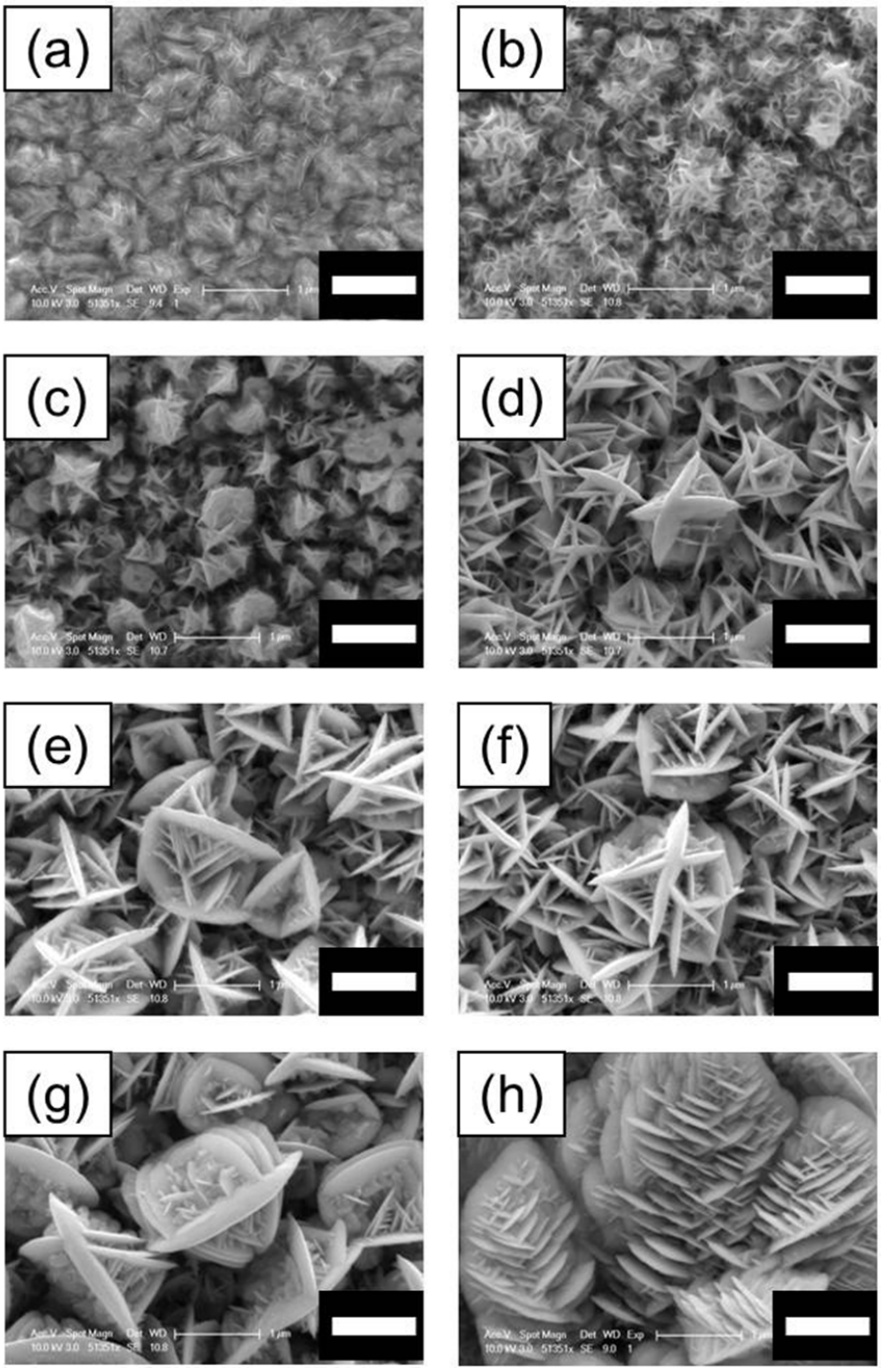

Figure 3.4. Surface morphologies of Bi_xTe_y thin films synthesized by galvanic displacement on sacrificial cobalt thin films for (a) 0, (b) 0.5, (c) 1, (d) 3, (e) 6, (f) 15, (g) 30, and (h) 60 min, respectively. The numbers in this figure correspond to the reaction times shown in Figure 1. Scare bar = 1μm.

morphology and amount of Bi_xTe_y deposits changes with the increase of galvanic displacement time on sacrificial Co thin films. When the reaction time was shorter than 3 min (the first step), it can be clearly seen that the Bi_xTe_y film become rougher due to the formation of Bi_xTe_y nuclei (Figure 3.4(b), 0.5 min) and a star-shaped Bi_xTe_y nanostructures form on the surface of sacrificial Co thin films (Figure 3.4(c)-(d), 1~3 min). This result implies that the Bi_xTe_y deposition occurred at a very short reaction time (~3 min) onto the Co surface in the regions of first step, where the nucleation is assumed to be dominant. As the reaction goes on, the initial star-shape of Bi_xTe_y nanostructures are grown accordingly, and then begins to form the spindle-shapes of Bi_xTe_y with a few branches in the second step (Figure 3.4(e)-(f), 3 ~ 15 min). Finally, the spindle structures of Bi_xTe_y are continuously grown with the formation of additional sub-branches on their nanostructures, demonstrating that the deposition process is completely changed from nucleation stage to growth stages in the third step (15 ~ 60 min) as represented in Figure 3.4(g)-(h). These changes of surface morphology during galvanic displacement reaction are consistent with the OCP and EDS analysis.

The cross-sectional SEM images of the Bi_xTe_y thin films synthesized by galvanic displacement on sacrificial Co thin films for 0.5, 1, 6 and 60 min are given in ESI†. At the beginning of the reaction at 0.5 min (Figure 3.5(a)), a very thin Bi_xTe_y cluster (brighter region in upper part) grows out on the sacrificial Co thin films (darker region in lower part), whereas Bi_xTe_y nuclei become larger in the opposite direction to the sacrificial thin films at 1 min. As shown in Figure 3.5(b)-(c), the cross-section of Bi_xTe_y and sacrificial Co thin films consist of a thin nucleation layer (NL) with a diffusion layer

(DL). The existence of NL is confirmed by line scanning of the EDS analysis, indicating the higher intensity of Te (red) and Bi (blue) rather than Co (black) in the NL. After 6 min of galvanic displacement reaction in second step, there is a sharp transition between

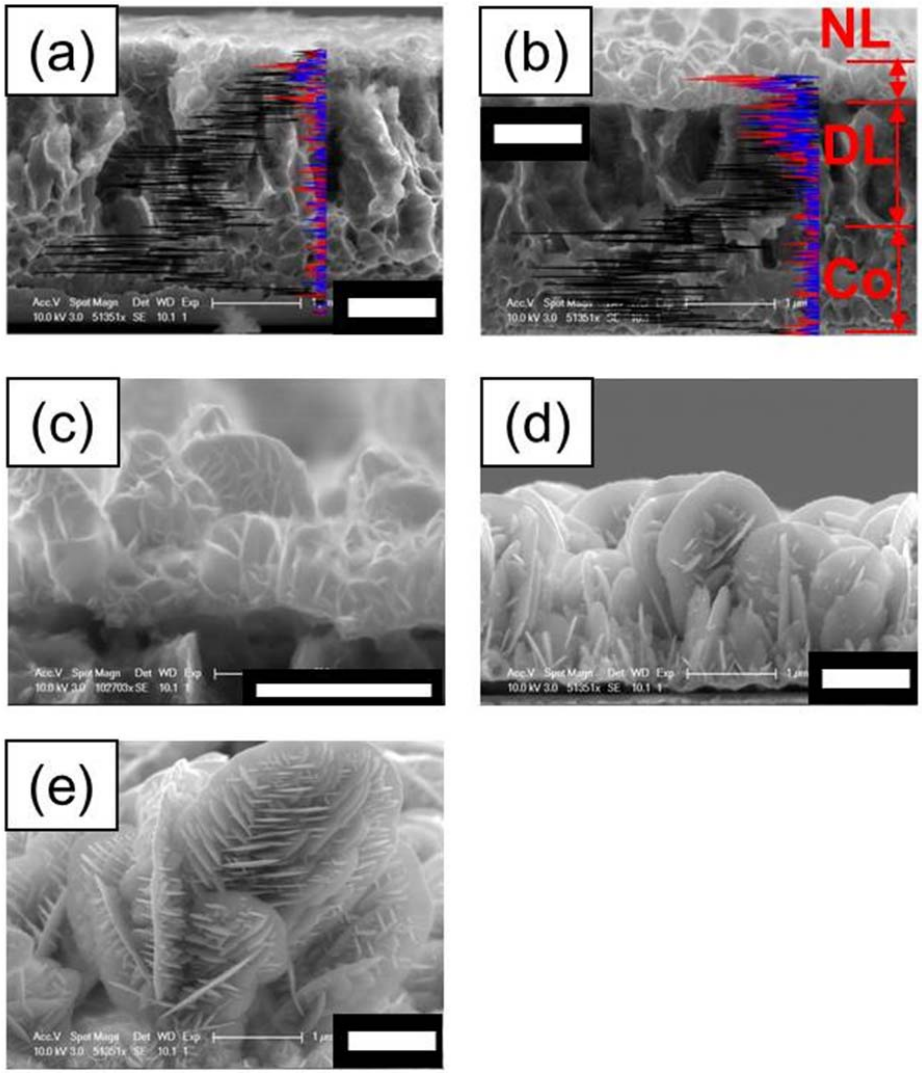

Figure 3.5. Cross-sectional SEM images of Bi_xTe_y thin films synthesized by galvanic displacement on sacrificial cobalt thin films for (a) 0.5, (b-c) 1, (c) 6, and (d) 60 min, respectively. Black, red, and blue lines on (b) represent EDS line scan profiles of Co, Te and Bi. Also, NL, DL, and Co indicate the nucleation, diffusion, and sacrificial cobalt layer, respectively. Fig. S1(c) shows the magnification image of NL in Fig. S1(b). Scare bar = 1μm.

the nucleation stage and the growth stage as observed by SEM in Figure 3.5(d). The gradual growth of Bi_xTe_y nanostructures can be clearly seen until it changes into the spindle-structures with a few branches. Moreover, Figure 3.5(d) shows that there is no sacrificial Co thin film underneath Bi_xTe_y nanostructure at 6 min, which is expected from the results of the EDS analysis as described previously in Figure 3.3. Therefore, this observation supports the conclusion that the rate of the reduction (Bi^{3+} and $HTeO_2^+$) is high enough to increase OCP sharply by consuming all of sacrificial Co thin films in the second step. In the third step, occurring after 60 min of reaction, the spindle-shape morphology of Bi_xTe_y is well preserved as the size of nanostructures grow with additional sub-branches compared to the original structures, as shown in Figure 3.5(e).

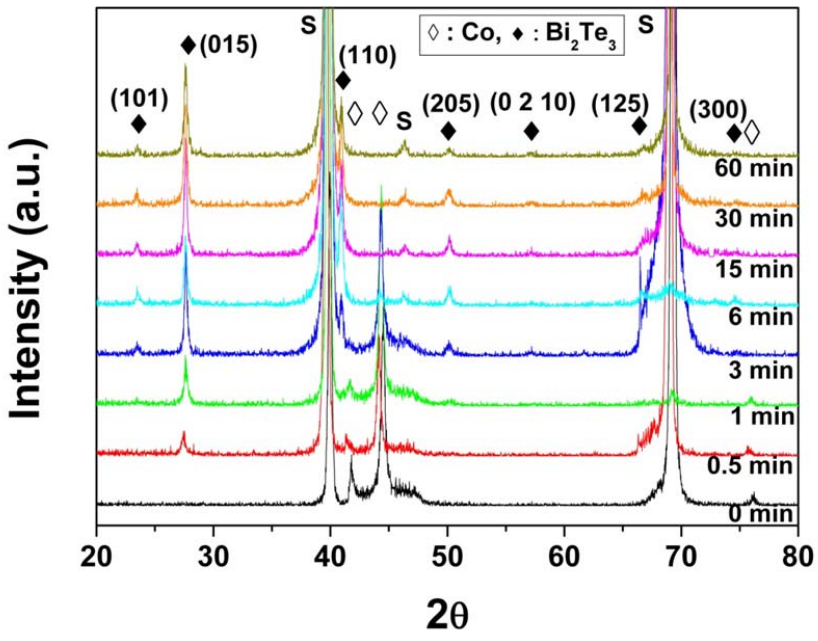

Figure 3.6. XRD patterns of the galvanically synthesized Bi_xTe_y thin films on sacrificial cobalt thin films as a function of time. (S : substrates – Pt and Si)

Figure 3.6 shows XRD patterns of electrodeposited Co and galvanically deposited Bi_xTe_y on the sacrificial Co thin films. It can be seen that the peak of sacrificial Co are mixed structures with fcc (face-centered cubic) and hcp (hexagonal close packed) phases, whereas all the Bi_xTe_y deposits are typical polycrystalline rhombohedral structures along with (101), (015), (110), (205), (0 2 10), (125), and (300) directions according to standard JCPDS 15-0863. The peak intensity of sacrificial Co gradually decreases in the first step (~ 3min), and then shows no further sacrificial peak after 6 min, indicating that all sacrificial Co has already reacted with Bi^{3+} and/or $HTeO_2^+$ ions by galvanic displacement. It is in good agreement with EDS analysis and cross-sectional SEM images as shown in Figure 3.3 and 3.5. However, there is no difference in the XRD patterns of the galvanically deposited Bi_xTe_y films except the increase in the magnitude of the peaks at different reaction time. In order to further understand the predominant peaks of Bi_xTe_y deposits, we calculated the texture coefficient (TC) in the stronger diffraction spectra with (101), (015), (110), and (205) directions (eq. 1) [15].

$$TC_{(hkl)} = \frac{\frac{I_{(hkl)}}{I_{o(hkl)}}}{\frac{1}{N}\sum_N\left(\frac{I_{(hkl)}}{I_{o(hkl)}}\right)} \qquad \text{(eq. 1)}$$

where TC is texture coefficient, I*(hkl)* is the observed intensity of the *(hkl)* plane, I_0*(hkl)* is the standard data (JCPDS 15-0863) of the *(hkl)* plane, and N is the total number of diffraction peaks. Once the TC value is greater than unit, it indicates that the preferred orientation exists along with *(hkl)* plane in the sample. Figure 3.7 shows the TC of

galvanically deposited Bi_xTe_y as a function of reaction time. As shown in Figure 3.7, the predominant orientation of Bi_xTe_y deposits is (101) and (110) planes, which show the TC value is larger than 1. Furthermore, the TC of all planes increases as reaction is started (~ 3min), while there is no further significant changes in the second and third step (after 3 min). It is evident that remarkable increases in TC occurrs due to the vigorous nucleation of Bi_xTe_y in the first step, and the plateau region of TC in the second and third steps confirms transition from nucleation to the growth stage.

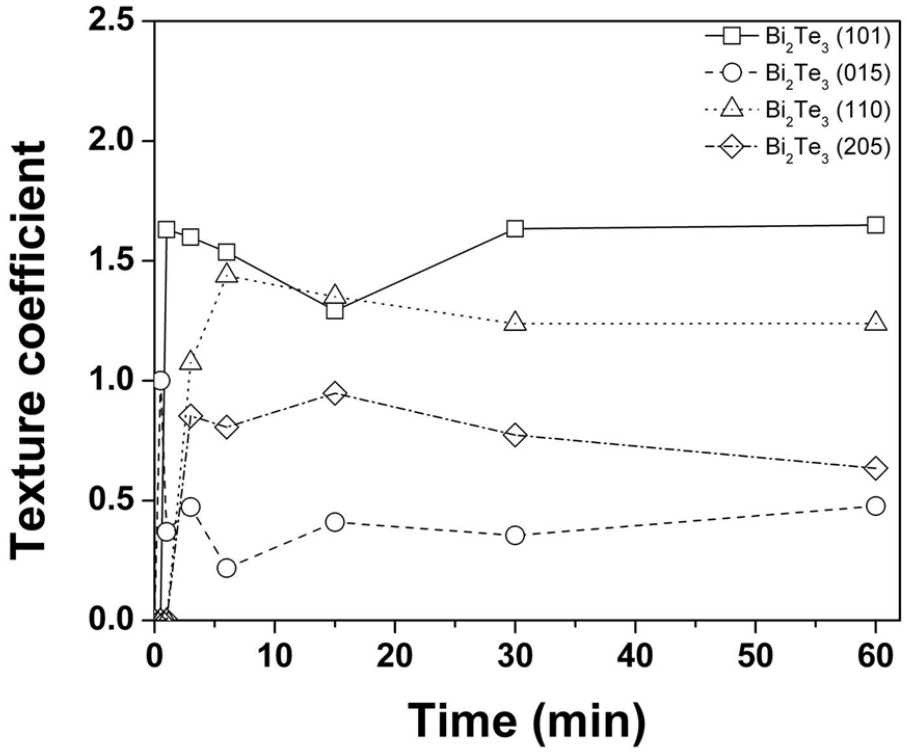

Figure 3.7. Texture coefficient of the galvanically synthesized Bi_xTe_y thin films as a function of reaction time

3.5 Conclusions

In summary, we demonstrated a three-step growth mechanism of galvanically synthesized Bi_xTe_y thin films with 6 mM Bi^{3+} + 10 mM $HTeO_2^+$ + 1 M HNO^3 for 1 h on sacrificial Co thin films. Through OCP analysis, the galvanic displacement reaction and growth mechanism can be clearly predicted as follows: (a) the formation of nucleation and star-shaped Bi_xTe_y in the initial stage (0.5 to 3 min), (b) the growth of star-shape nanostructure to form spindle-shaped Bi_xTe_y with a few branches between 3 to 15 min, and (c) the continuous growth of spindle structures and formation of additional sub-branches on the initial nanostructure (up to 60 min). This study provides a means for the synthesis of Bi_xTe_y nanostructures by galvanic displacement from sacrificial Co thin films, and contributes to an understanding of its growth mechanism. This study will facilitate the fabrication of other chalcogenide nanostructures by galvanic displacement reactions.

3.6 References

[1] R. S. Mane and C. D. Lokhande, Mater. Chem. Phys., 2000, 65, 1-31

[2] R. Y. Wang, J. P. Feser, X. Gu, K. M. Yu, R. A. Segalman, A. Majumdar, D. J. Milliron and J. J. Urban, Chem. Mater., 2010, 22, 1943-1945.

[3] M. Fardy, A. I. Hochbaum, J. Goldberger, M. M. Zhang and P. Yang, Adv. Mater., 2007, 19, 3047-3051

[4] M. Bouroushian, Electrochemistry of Metal Chalcogenides, Springer, 1st edn., 2010

[5] K. Rajeshwar, Adv. Mater., 1992, 4, 23-29.

[6] D. M. Rowe, CRC Handbook of Thermoelectrics, CRC Press, 1st edn., 1995

[7] B. Y. Yoo, C. K. Huang, J. R. Lim, J. Herman, M. A. Ryan, J. P. Fleurial and N. V. Myung, Electrochim. Acta, 2005, 50, 4371-4377.

[8] X. B. Zhao, X. H. Ji, Y. H. Zhang, T. J. Zhu, J. P. Tu and X. B. Zhang, Appl. Phys. Lett., 2005, 86, 062111.

[9] L. Jongmin and et al., Nanotechnology, 2008, 19, 365701.

[10] C. H. Chang, Y. Rheem, Y.-H. Choa, D.-Y. Park and N. V. Myung, Electrochim. Acta, 2010, 55, 1072-1080

[11] H. Jung, Y. Rheem, N. Chartuprayoon, J.-H. Lim, K.-H. Lee, B. Yoo, K.-J. Lee, Y.-H. Choa, P. Wei, J. Shi and N. V. Myung, J. Mater. Chem., 2010, 20, 9982-9987

[12] F. Xiao, B. Yoo, K. H. Lee and N. V. Myung, J. Am. Chem. Soc., 2007, 129, 10068-10069.

[13] M. S. Milan Paunovic, Fundamentals of Electrochemical Deposition, Wiley-Interscience, 2nd edn., 2006.

[14] M. Martin-Gonzalez, A. L. Prieto, R. Gronsky, T. Sands and A. M. Stacy, J. Electrochem. Soc., 2002, 149, C546-C554.

[15] A. K. Singh, Advanced x-ray techniques in research and industry IOS Press, Amsterdam, 1st edn., 2005.

Chapter 4

Electrochemical Synthesis of Bi and Te Nanostructures

4.1 Abstract

Bismuth (Bi) and tellurium (Te) thin films were formed by galvanic displacement of different sacrificial iron group thin films [i.e. nickel (Ni), cobalt (Co) and iron (Fe)] where the formation was systematically investigated by monitoring the change of open circuit potential (OCP), surface morphology and microstructure. The surface morphologies and crystal structures of galvanically displaced Bi or Te thin films strongly depended on the type and thickness of the sacrificial materials. Continuous Bi thin films were successfully deposited with the sacrificial Co. However, dendrites and nanoplatelets were formed from the Ni and Fe thin films. Te thin films were synthesized with all the three sacrificial thin films. Chemical dissolution rate of the sacrificial thin films and mixed potential strongly influenced formation of Bi or Te thin films.

4.2 Introduction

Bismuth (Bi) and tellurium (Te) are one of well-knownmaterials used in thermoelectric devices, which convert thermal energy from temperature gradient into electrical energy (the Seebeck effect), or vice versa (the Peltier effect), without any moving parts [1]. Bi with a low melting point (271 $^{\circ}$C) and a rhombohedral crystal structure has been extensively studied because of its unusual electronic properties; small

effective electron mass (0.001 m_e), large carrier mean free path (～100 nm at 300 K and ～400 μm at 4 K), large Fermi wavelength λ_F (40 nm at room temperature), highly anisotropic Fermi surface, small band overlap (～38 meV at 77 K) and low charge-carrier density [2,3]. Most of research works for Bi have been focused on fabrication methods, electronic properties, thermoelectric properties, and its applications. One- or two-dimensional Bi nanostructures (i.e. nanowires, nanotubes or thin films) have been recently used to investigate quantum confinement [2], finite-size effect [4], magnetoresistance (MR) effect [5,6], and thermoelectric effect [7] due to the potential applications in thermoelectric devices, photonics and optoelectronics. Several different methods such as electrodeposition [3,5], high-pressure injection [8], evaporation or sputtering [9], electron-beam lithography [2], low-temperature hydrothermal reduction [10], room temperature aqueous chemical route [11], solvothermal method [12], and vapor-phase deposition technique [13] were used to synthesize these nanostructures.

Te with a p-type narrow band gap (direct band gap energy: 0.35 eV) and a highly anisotropic crystal structure has been studied because of several potential applications in high-efficiency photoconductors, thermoelectric and piezoelectric devices, electronic and optoelectronic devices [14,15]. Te exhibits several interesting chemical and physical properties such as catalytic activity, piezoelectricity, thermoelectricity, non-linear optical response, and photoconductivity [15,16]. Specially, trigonal tellurium (t-Te) shows a highly anisotropic crystal structure which consists of helical chains of covalently bonded Te atoms and is bound together through van der Waals interactions in a hexagonal lattice

[14,16]. This anisotropic structure results in one-dimensional growth (e.g. nanowire, nanorod, nanobelt or nanotube) [16].

In addition, various functional materials can be synthesized using the reaction between tellurium and other elements (Bi [1], Cd [17], Pb [18–20] and Sb [21]). Most of research works for Te have been focused on synthesis of nanostructures and thin films by using the various techniques including refluxing [16], microwaveassisted synthesis [22], thermal decomposition [23], solvothermal or hydrothermal methods [24], biomolecule-assisted routes [25] and chemical vapor deposition [14,26].

Among different techniques to synthesize Bi, Te and its alloys, electrochemical processes such as electrodeposition, electroless (autocatalytic) deposition and galvanic displacement (also called as immersion plating or cementation) are considered as one of the promising processes due to several advantages over vacuum processes [27]. Galvanic displacement among other electrochemical methods can be considered as a simple and fast process to deposit Bi and Te thin films on the substrate and to tailor the morphology, crystal structure and composition by varying experimental conditions (e.g. sacrificial material, temperature, composition of electrolyte). Also, galvanic displacement can offer the advantage of selective deposition because reduction of metal ions in electrolyte is coupled with oxidation and dissolution of the sacrificial material on substrate. For example, galvanic displacement has been used to selectively deposit Cu and other metals onto Si for applications such as integrated circuits, microelectromechanical systems (MEMS), surface-enhanced Raman spectroscopy, catalysis and microchannel chemical reactors [28–30]. Recently, galvanic displacement has been utilized to deposit pure

metals and binary alloys by several research groups [31–46] including noble (i.e. Au, Ag, Pt and Pd) [32–37] and less-noble (i.e. Ni, Cu and Pb) [38–42] metals. Xia and co-workers have also synthesized binary alloys including Au–Ag, Pd–Ag and Pt–Ag [43,44]. However, galvanic displacement has not been utilized to synthesize less common metals and semiconducting materials, although extensive studies for Bi, Te and their alloyswere investigated [1–7,14–16]. In our prior work, we demonstrated the feasibility of synthesizing of Bi_xTe_y nanotubes and thin films by galvanic displacement [45,46]. However, there is a lack of systematic studies on the formation of pure Bi and Te from sacrificial metals.

In this chapter, we conducted systematic investigation to monitor the formation of Bi and Te by galvanic displacement of the sacrificial iron group metallic films (Fe, Co and Ni). Electrochemical technique such as open circuit potential (OCP) measurement was utilized to monitor the process. SEM and XRD were utilized to observe the surface morphology and microstructure.

4.3 Experimental Section

In order to synthesize Bi and Te thin films by galvanic displacement, three different sacrificial iron group (i.e. Ni, Co and Fe) thin films with approximately 3μm thickness were electrodeposited on Pt-coated Ti/SiO_2/Si substrates from chloride baths where the substrates consist of Pt(200 nm)/Ti(20 nm)/SiO_2(100 nm)/Si. Pt (platinum) and Ti (titanium) were formed on SiO_2/Si substrate by electron-beam evaporation process. Pt was used as a seed layer and Ti was used as an adhesion layer between Pt and SiO_2 layer.

Electrodeposition was conducted using a Princeton Applied Research Potentiostat (VMP2) at current density of 5mAcm^{-2} androomtemperature without stirring. Saturated calomel electrode (SCE) and Pt-coated Ti anode were used as a reference and a counter electrode, respectively. Electrolyte compositions and operation conditions for electrodeposition of the sacrificial thin films can be found elsewhere [46]. Calcium chloride was used as a supporting electrolyte and l-ascorbic acid was used to prevent oxidation of Fe^{2+} in the electrolyte for electrodeposition of Fe thin film. Solution pH was controlled to be 3 with HCl or NaOH.

For galvanic displacement, electrodeposited Ni, Co and Fe thin films were immersed into the bismuth or tellurium containing electrolytes for 1 h (or 3 h). Solution pH for galvanic displacement was fixed at 1. OCP during galvanic displacement reaction was measured in a three-electrode cell to monitor the effect of the sacrificial materials. Electrolyte compositions for galvanic displacement are listed in Table 1. Bismuth nitrate [$Bi(NO_3)_3 \cdot 5H_2O$], tellurium oxide (TeO_2, 99.99%; Alfa Aesar) and nitric acid (HNO_3)were used tomake the electrolytes for galvanic displacement. Concentrations of metal ion sources (Bi^{3+} for Bi thin film or $HTeO_2^+$ for Te thin film) were fixed at 10 mM and HNO_3 at 1 M for comparison.

Surface morphology and film composition of the thin films obtained from electrodeposition and galvanic displacement were examined using a scanning electron microscope (SEM) (model: XL30-FEG, Phillips) and an energy-dispersive spectroscopy (EDS) (model: EDAX, Phoenix). An X-ray diffractometer (XRD) (model: D8 advance diffractometer, Bruker) with Cu Kα radiation (operating at 40 kV) was used for the

identification of the phase in the thin films. The conditions of XRD were a scanning range of 20–80° with 0.02° increments and a 0.5 s collection time per increment.

Table 4.1. Bath compositions and operation conditions for galvanic displacement to synthesize Bi_xTe_y thin films.

Composition	Electrolyte	Temperature [°C]	Agitation
Bi	10mM Bi^{3+} + 1M HNO_3	RT	No
Te	10mM $HTeO_2^+$ + 1M HNO_3	RT	No

4.4 Results and discussion

4.4.1 Effect of Type of Sacrificial Materials

Open circuit potentials (OCP) as a function of reaction time during galvanic displacement were measured to monitor the reactions between metal ions (Bi^{3+} and $HTeO_2^+$) in electrolytes and the sacrificial metal films (Ni, Co and Fe) as shown in Figure 4.1. The sacrificial thin films are galvanically displaced to form Bi or Te thin films because there exists the difference of redox potentials between metal ions (Bi^{3+} or $HTeO_2^+$) in electrolyte and the sacrificial thin films (Ni, Co and Fe) as the following equations [1,20,45,47]:

$$Bi^{3+} + 3e^- \rightarrow Bi\ (s) \qquad E^0 = 0.317\ V\ vs\ SHE \qquad (1)$$

$$HTeO_2^+ + 3H^+ + 4e^- \rightarrow Te\ (s) + 2H_2O \qquad E^0 = 0.551\ V\ vs\ NHE \qquad (2)$$

$Ni^{2+} + 2e^{-} \rightarrow Ni\ (s)$ $E^0 = -0.257$ V vs SHE (3)

$Co^{2+} + 2e^{-} \rightarrow Co\ (s)$ $E^0 = -0.28$ V vs SHE (4)

$Fe^{2+} + 2e^{-} \rightarrow Fe\ (s)$ $E^0 = -0.44$ V vs SHE (5)

Galvanic displacement occurs spontaneously because Bi or Te metals are more noble (easier to reduce) than the sacrificial materials (Ni, Co and Fe) [45]. Figure 4.1(a) shows three OCP curves of Bi^{3+} ions for galvanic displacement with the sacrificial Ni, Co and Fe thin films during 60 min. It was observed in Figure 4.1(b) that OCP curves started from negative potential values (−0.37 V for Fe < −0.15 V for Co < −0.07 V for Ni) at early initial stage of galvanic displacement reaction and the starting potential values in OCP curve were matched to the sequence of standard redox potential values (−0.44 V vs. SHE for Fe < −0.28 V vs. SHE for Co < −0.257 V vs. SHE for Ni). The negative potential at the early initial stage in OCP curve may indicate the mixed potentials between reduction of Bi^{3+} in the electrolyte and oxidation of the sacrificial metal thin films. The driving force for galvanic displacement reaction is the difference of redox potentials between Bi^{3+} in the electrolyte and the sacrificial metal thin films [1,20,45]. After the early initial stage, OCP curve for the sacrificial Ni thin film leveled off without showing step I. However, OCP curve exhibited very short step I for the sacrificial Fe thin film and clear step I for the sacrificial Co thin film, respectively. Clear three steps were observed only for the sacrificial Co thin film and not for the sacrificial Ni and Fe thin films. Existence of step I during galvanic displacement reaction strongly depend on type

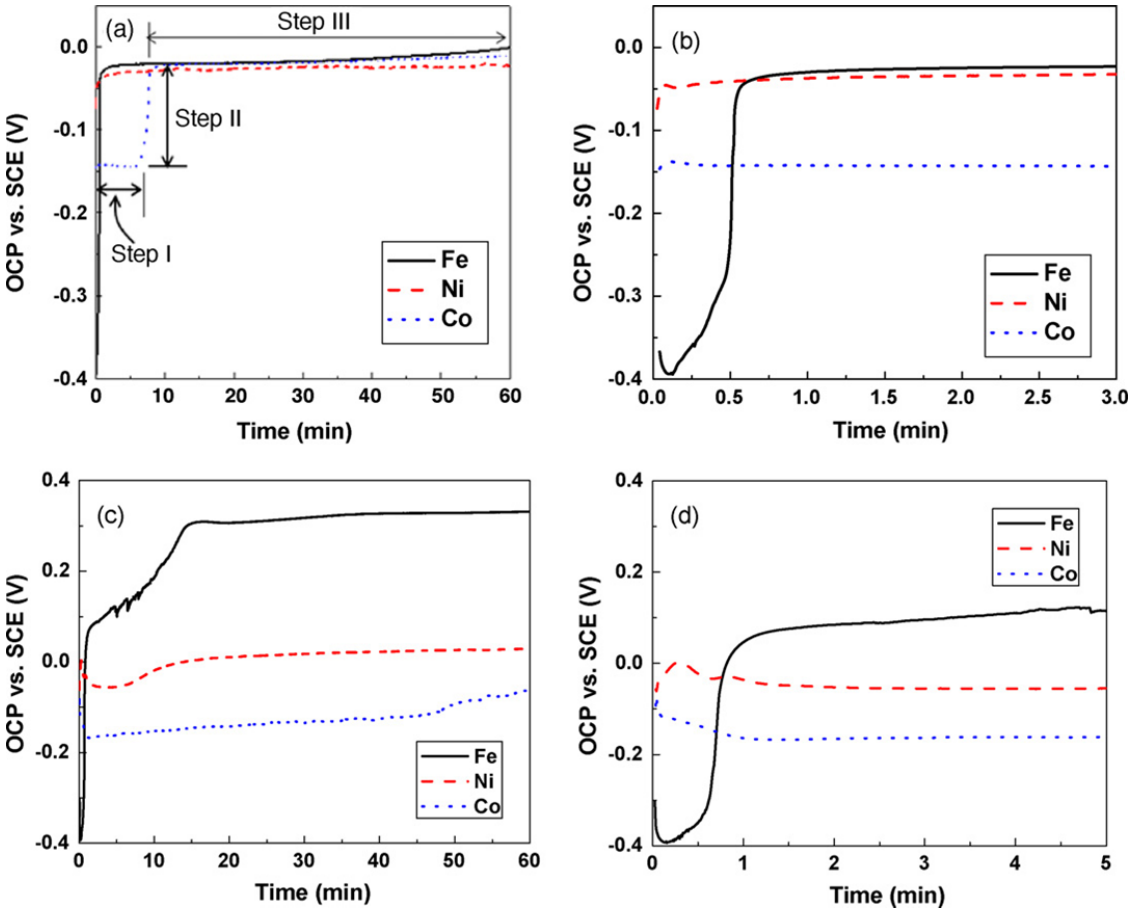

Figure 4.1. Open circuit potential (OCP) as a function of galvanic reaction time; the sacrificial materials (Ni, Co and Fe) are immersed into nitric acid baths containing (a) 10 mM Bi^{3+}, (b) initial stages of OCP curves in (a) within 3 min, (c) 10 mM $HTeO_2^+$, and (d) initial stages of OCP curves in (c) within 5 min. Solid, dash, and dotted lines represent Fe, Ni, and Co, respectively.

of the sacrificial thin film. OCP curve sharply increase again (step II) as soon as the sacrificial thin film is completely covered by Bi thin film. After finishing galvanic displacement reaction, OCP curve reached to be another steady-state value at near 0 V vs SCE (step III). Reaction time for galvanic displacement with the sacrificial Co thin film was measured to be approximately 10 min and less than 1 min for the sacrificial Fe and

Ni thin films. Absence of clear three steps in OCP curve for the sacrificial Ni thin films may be attributed to much slower dissolution rate of the sacrificial Ni layer than reduction rate of Bi^{3+} ions in the electrolyte. However, much faster dissolution rate of the sacrificial Fe layer than reduction rate of Bi^{3+} ions in the electrolyte is responsible for very short step I. Effects of extremely slow dissolution rate of the sacrificial Ni layer and very fast dissolution rate of the sacrificial Fe layer on formation of Bi thin film will be discussed further with SEM microscopic images in details. As the surface coverage of Bi or Te increased with the reduction of sacrificial film surface, it shifted the open circuit potential value toward more positive value during step II. After Bi thin films completely covered the surface, the potential reached a steady state mixed potential between Bi/Bi^{3+} and dissolved oxygen oxidation. Figure 4.1(c) shows OCP curves of $HTeO_2^+$ (with a concentration of 10 mM) ion with the sacrificial Ni, Co and Fe thin films for galvanic displacement during 60 min. Clear step I in OCP curve for all the sacrificial thin films (Co, Ni and Fe) were observed. Reaction time for galvanic displacement with the sacrificial Fe thin film was measured to be approximately 15 min. However, reaction times for the sacrificial Ni and Co thin films were measured to be greater than 60 min. From comparison of open circuit potential values at step III in OCP curves of Bi^{3+} [~ -0.03 V for the sacrificial Ni, Co and Fe thin films in Figure 4.1(a)] and $HTeO_2^+$ [~ 0.3 V for the sacrificial Fe, ~ 0 V for the sacrificial Ni, and ~ -0.1 V for the sacrificial Co thin films in Figure 4.1(c)] ions, it can be suggested that the sacrificial Ni and Co thin films were not completely displaced by Te during galvanic displacement reaction. In order to completely displace the sacrificial Ni, Co and Fe thin films with Bi

or Te metals by galvanic displacement, surface morphologies during galvanic displacement reaction should be porous for metal ions (Bi^{3+} or $HTeO_2^+$) in the electrolyte to reach to the sacrificial layers. If the metal ions (Bi^{3+} or $HTeO_2^+$) in the electrolyte cannot reach and contact the sacrificial layers, galvanic displacement cannot be continued. This will be discussed further in Figure 4.6. It was clearly observed that shape of OCP curve or potential value after finishing galvanic displacement reaction strongly depend on both type of the metal ion in the electrolyte and that of the sacrificial materials.

After finishing galvanic displacement reaction with the sacrificial metal thin films (Ni, Co and Fe) for 60 min, surface morphologies of galvanically synthesized Bi were observed using SEM, as shown in Figure 4.2. Figure 4.2(a) shows the surface morphology of electrodeposited sacrificial Ni thin film from chloride bath before galvanic displacement reaction [46]. Surface morphology of Bi galvanically synthesized with the electrodeposited Ni thin film exhibited several isolated particles [marked with red arrows in Figure 4.2(b)], in the absence of uniform thin film. Needle-like shape surface in Figure 4.2(a) and (b) comes from the electrodeposited Ni thin film. Those particles in Figure 4.2(a) were verified to be Bi using EDS analysis. Therefore, it can be concluded that dissolution (oxidation) rate of the electrodeposited Ni thin film during galvanic displacement in nitric acid solution is extremely slow. On the other hand, surface morphology of the galvanically synthesized Bi thin film (Figure 4.2(d)) with the electrodeposited Co thin film as a sacrificial thin film exhibits a granular structure with a polygon shape arrangement and somewhat similar to surface morphology of the

electrodeposited Co thin film (Figure 4.2(c)). EDS analysis confirm the formation of Bi thin film.

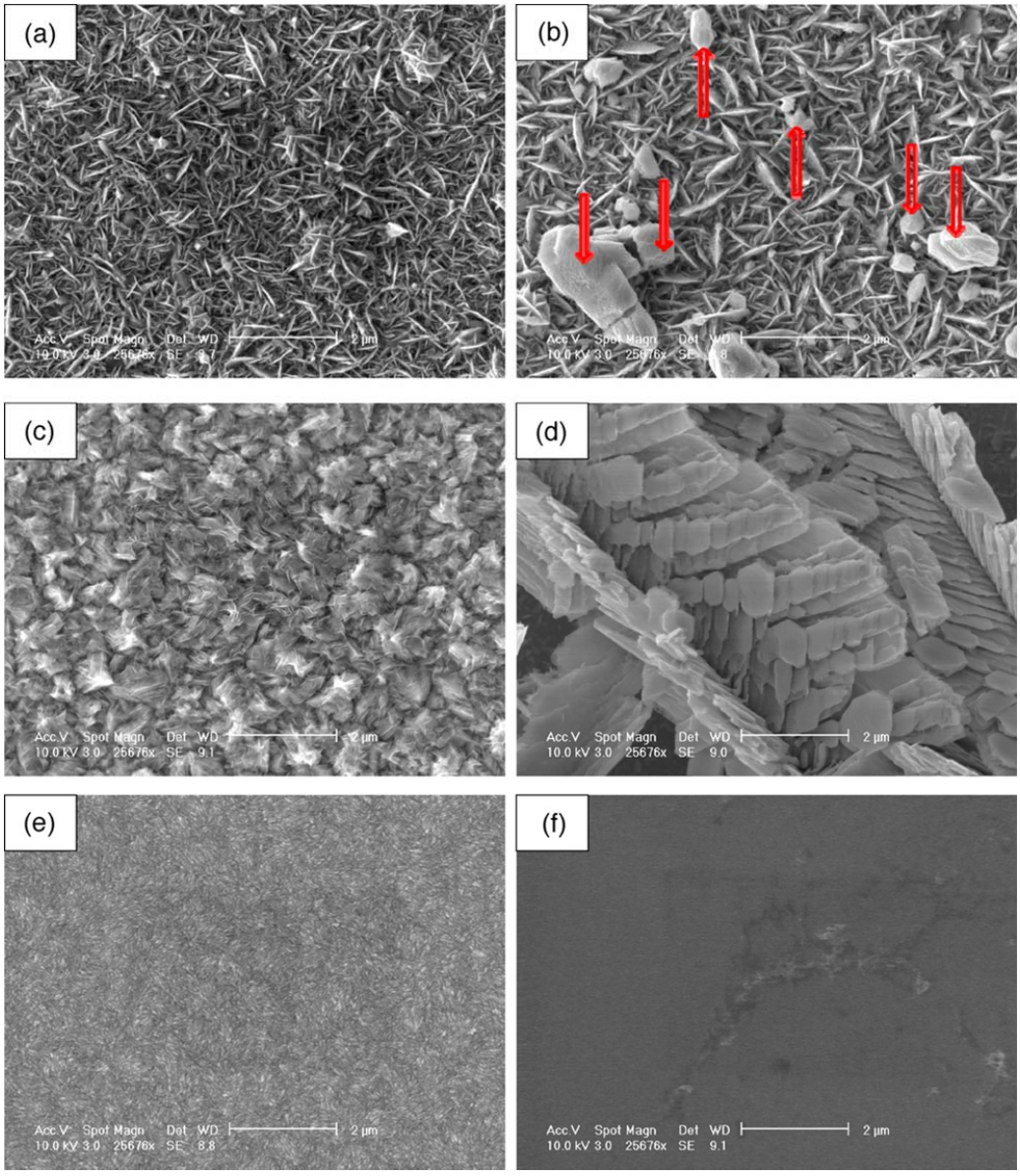

Figure 4.2. Surface morphologies of sacrificial (a) Ni, (c) Co and (e) Fe thin films electrodeposited from chloride baths. Surface morphologies of Bi thin films deposited by galvanic displacement reaction for 60 minutes with the sacrificial (b) Ni, (d) Co and (f) Fe thin films.

Three-micron thick electrodeposited Fe film had dense and uniform deposit (Figure 4.2(e)). However, Bi thin film was not formed by galvanic displacement reaction (Figure 4.2(f)). EDS also confirmed the finding which might be attributed to complete chemical dissolution of Fe thin film prior to galvanic displacement. To further investigate the process, the effect of film thickness of Fe on the formation of Bi was conducted which will be discussed in later section. Also, only Bi particles were obtained using the sacrificial Ni thin film during galvanic displacement reaction. The exact mechanism leading to those phenomena in Figure 4.2(b and f) has not yet been identified. It is obvious that formation of the galvanically synthesized Bi thin films with the sacrificial Ni, Co and Fe thin films strongly depend on type of the sacrificial thin films. From SEM observation in Figure 4.2, it is clear that the galvanically synthesized Bi particles resulted from extremely slow dissolution rate of the sacrificial Ni thin films. Also, very fast dissolution rate of the sacrificial Fe thin films resulted in no formation of Bi thin film by galvanic displacement of thin Fe films (approx. 3 μm).

Surface morphology of galvanically synthesized Te thin films with the sacrificial metal thin films (Ni, Co and Fe) for 60 min was observed using SEM, as shown in Figure 4.3. Te thin films were successfully deposited with the three sacrificial thin films by galvanic displacement reaction. Te thin films deposited by galvanic displacement with the electrodeposited Ni (Figure 4.3(a)), Co (Figure 4.3(b)) and Fe (Figure 4.3(c)) thin films showed completely different surface morphology compared to the surface morphologies of the electrodeposited sacrificial Ni (Figure 4.2(a)), Co (Figure 4.2(c)), and Fe (Figure 4.2(e)) thin films [46]. Surface morphology of the galvanically

synthesized Te thin film with the electrodeposited Ni thin film exhibited awell-defined polygon shape as shown in Figure 4.3(a). On the other hand, surface morphology of the galvanically synthesized Te thin film with the electrodeposited Co thin film in Figure 4.3(b) showed a flower-like granular structure with very fine polygon shapes. Also, galvanically synthesized Te thin film with the electrodeposited Fe thin film had very fine polygon shape as shown in Figure 4.3(c). It is clear that surface morphologies of galvanically synthesized Te thin films with the sacrificial Ni, Co and Fe thin films were not depended on those of the sacrificial thin films (Figure 4.2(a) for Ni, Figure 4.2(c) for Co and Figure 4.2(e) for Fe).

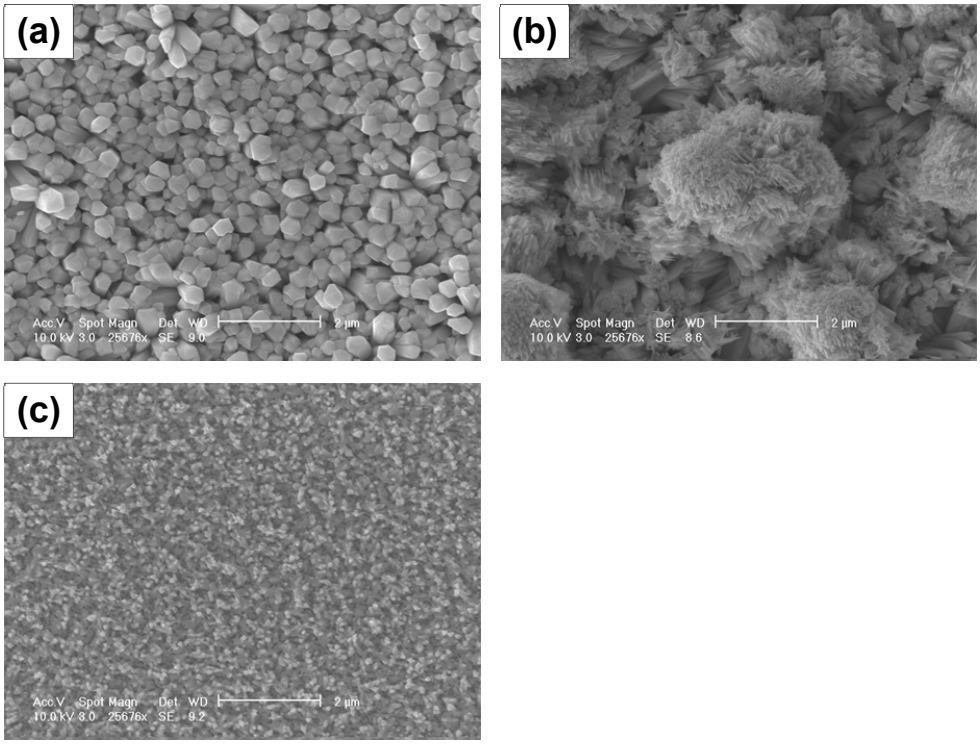

Figure 4.3. Surface morphologies of galvanically displaced Te thin films with sacrificial (a) Ni, (b) Co, and (c) Fe thin films.

Figure 4.4 shows XRD patterns of Bi thin films deposited by galvanic displacement with the different sacrificial Ni, Co, and Fe thin films. Bi thin film was clearly formed by galvanic displacement only with the sacrificial Co thin films as shown in Figure 4.4(b). Bi thin film in Figure 4.4(b) exhibits a typical XRD pattern of Bi with a dominant (0 1 2) planes and a rhombohedral structure (JCPDS No. 05-0519). However, only a very weak peak of Bi was observed during galvanic displacement with the sacrificial Ni thin films as shown in Figure 4.4(a). The weak Bi peak resulted from the formation of Bi particles instead of the formation of continuous Bi thin film. This XRD result is in good agreement with SEM observation of Bi particles in Figure 4.2(b). Therefore, it is clear from SEM, EDS and XRD analyses that only some amounts of Bi particles with the sacrificial Ni thin film were deposited by galvanic displacement due to extremely slow dissolution rate of Ni thin films into the electrolyte and low mixed potential to drive the reaction. On the other hand, no peak for Bi from XRD analysis of Figure 4.4(c) was observed by galvanic displacement with the sacrificial Fe thin film. Further analysis was conducted using EDS because it is not clear whether Bi thin film was formed by galvanic displacement with the sacrificial Fe thin film, or not. Neither Bi nor Fe was not detected at all in EDS analysis. This result indicates that Bi thin film was not formed during galvanic displacement reaction with 3 μm thick Fe thin film.

Figure 4.5 shows XRD patterns of Te thin films obtained by galvanic displacement with the different sacrificial metals such as Ni (Figure 4.5(a)), Co (Figure 4.5(b)), and Fe (Figure 4.5(c)). From XRD results, it is obvious that Te thin films were successfully synthesized by galvanic displacement with the sacrificial Ni and Co films, even with the

sacrificial Fe thin film, compared to XRD results of Bi thin films (Figure 4.4(a and c)). The galvanically synthesized Te thin films with the sacrificial Ni, Co and Fe thin films show a hexagonal structure (JCPDS No. 36-1452).

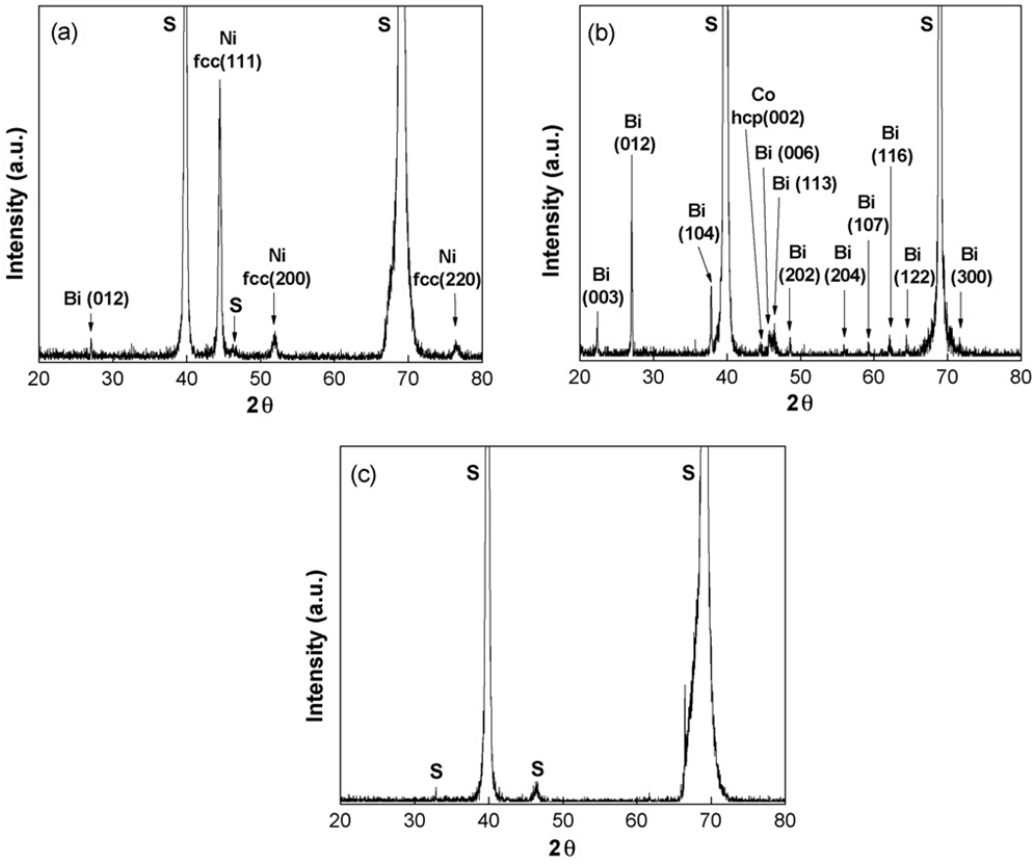

Figure 4.4. XRD patterns of the galvanically displaced Bi thin films with sacrificial (a) Ni, (b) Co, and (c) Fe thin films. (S: substrate – Pt and Si)

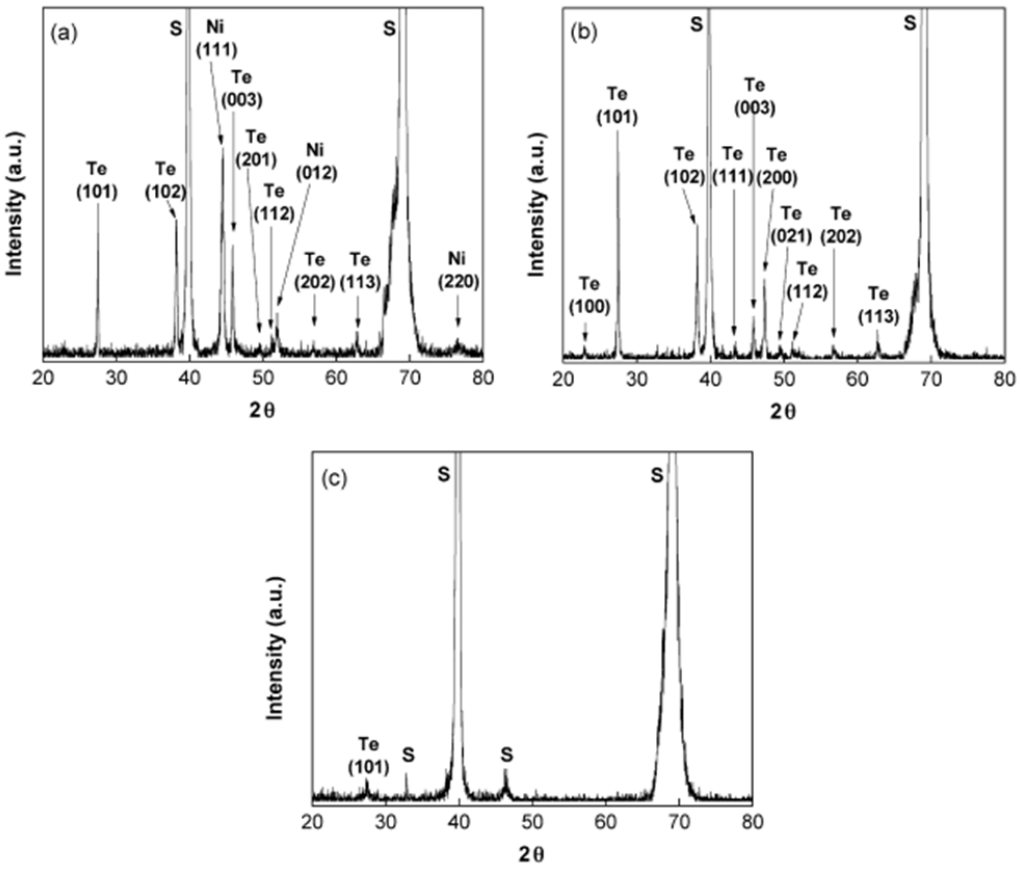

Figure 4.5. XRD patterns of galvanically displaced Te thin films with sacrificial (a) Ni, (b) Co, and (c) Fe thin films. (S: substrate – Pt and Si)

4.4.2 Effect of Thickness of Sacrificial Thin Films and Reaction Time

It is difficult to clearly observe total film thickness of the galvanically deposited Bi thin film using cross-sectional SEM image because of the formation of Bi particles instead of Bi thin film as shown in Figure 4.2(b) and no formation of Bi thin film as shown in Figure 4.2(f). Therefore, it is meaningless to compare thickness of Bi thin film obtained by galvanic displacement with the three different sacrificial thin films. However,

Te thin films were successfully formed during galvanic displacement with the three different sacrificial thin films. Thicknesses of Te thin films galvanically synthesized from nitric acid baths for 60 min and the sacrificial Ni, Co and Fe thin films electrodeposited from chloride baths could be clearly observed using cross-sectional SEM image as shown in Figurea 4.6–8. Nickel thin film with a thickness of ~3 μm electrodeposited from chloride bath has a typical dimple structure (sponge-like structure) of ductile metal as shown in Figure 4.6(a). After galvanic displacement for 60 min, Ni thin film was partially replaced by Te thin film with a polygon shape and thickness of Te thin film was measured to be ~0.8 μm thick. Te thin film exhibited columnar growth (Figure 4.6(b and c)). Columnar growth is commonly observed in the thin/thick films fabricated by other electrochemical processes such as electrodeposition [27,48] or electroless deposition [49–52]. Figure 4.6(b) exhibits Te thin film with ~0.8 μm thick after galvanic displacement reaction for 60 min with the sacrificial Ni thin film. The sacrificial Ni thin film with ~2.8 μm thick still remained as shown in Figure 4.6(b). This result may come from much slower dissolution rate of the sacrificial Ni thin film compared to reduction rate of $HTeO_2^+$ ion in nitric acid solution and is in good agreement with the result of OCP curve for the sacrificial Ni thin film Figure 4.1(c)). That is, OCP value for the galvanically deposited Te thin film with the sacrificial Ni thin film in Figure 4.1(c) was measured to be −0.04 V and indicated that the sacrificial Ni thin film was partially displaced by galvanic displacement. Te thin film with ~0.8 μm thick was formed by galvanic displacement the sacrificial Ni thin film for 1 h. After galvanic displacement reaction for

3 h, thickness of Te thin film was measured to be ~2.5 μm as shown in Figure 4.6(c). It was observed that growth rate of Te thin film was linearly proportional to time of galvanic displacement reaction.

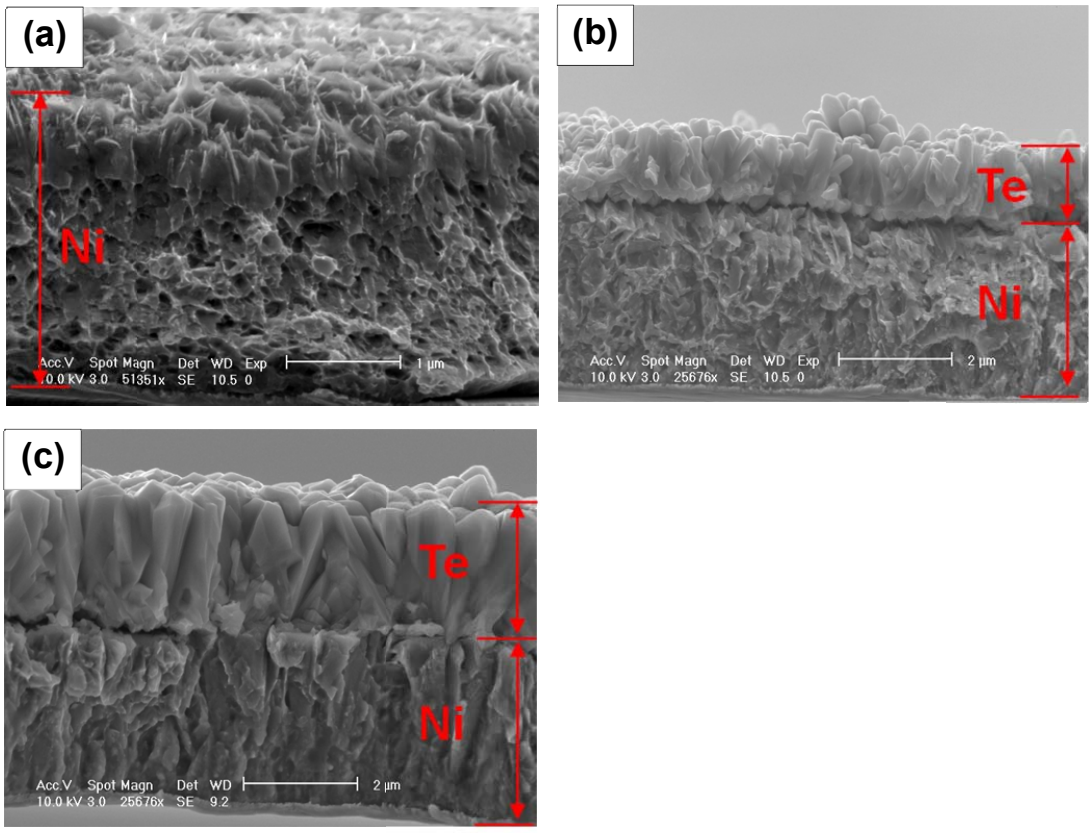

Figure 4.6. Cross-sectional SEM images of Te thin films deposited with the sacrificial Ni thin film by galvanic displacement; (a) the sacrificial Ni thin films electrodeposited from chloride bath, (b) Te thin film deposited by galvanic displacement with the sacrificial Ni thin film for 1 hr, and (c) Te thin film deposited by galvanic displacement with the sacrificial Ni thin film for 3 hrs.

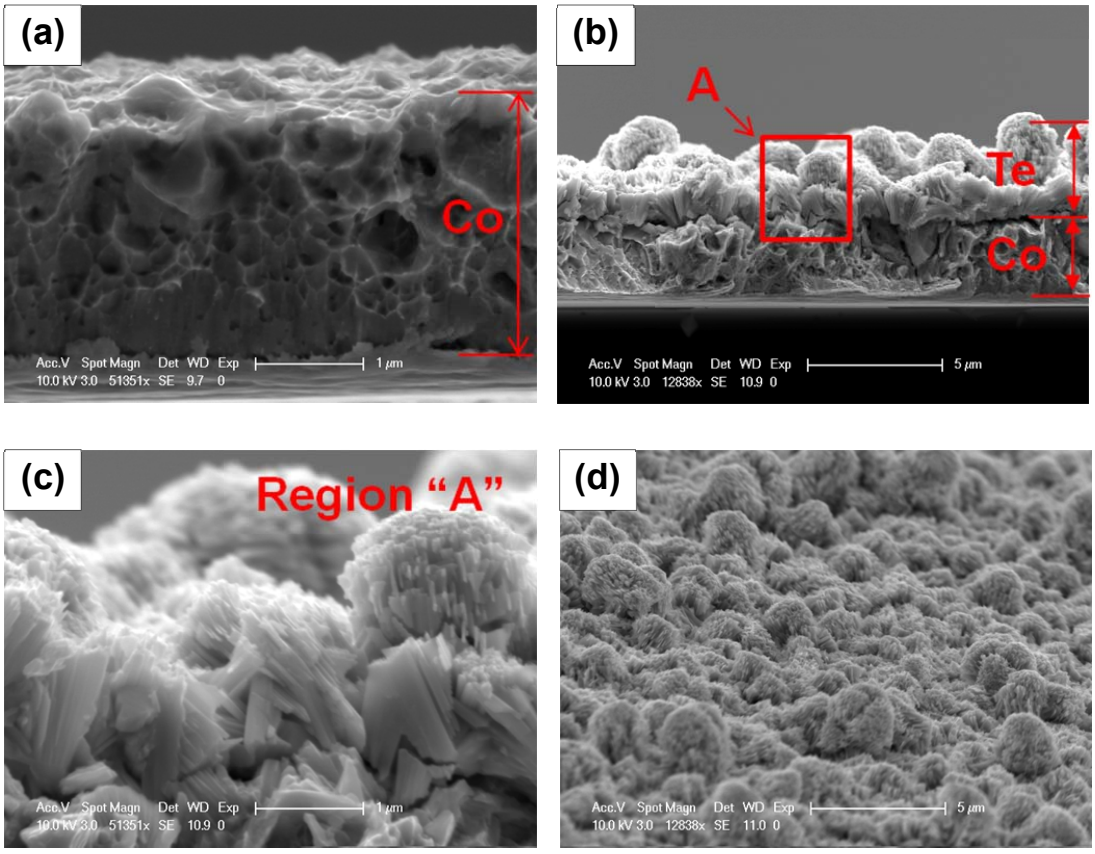

Figure 4.7. Cross-sectional SEM images of Te thin films deposited with the sacrificial Co thin film by galvanic displacement; (a) the sacrificial Co thin films electrodeposited from chloride bath, (b) Te thin film deposited by galvanic displacement with the sacrificial Co thin film for 1 hr, and (c) high magnification of Te thin film marked as region "A" in Fig. 7(b), (d) Tilting top view of Te thin film in Fig. 7(b).

Figure 4.7(a) shows the electrodeposited sacrificial Co thin film with ~3 μm thick. After galvanic displacement reaction with the sacrificial Co thin film for 1 h, thickness of Te thin film was ~1.8 μm thick as shown in Figure 4.7(b). Te thin film was deposited galvanically in powdery form and showed very rough surface as shown in Figure 4.7(d). After galvanic displacement for 1 h, significant amount of the sacrificial Co thin film in

Figure 4.7(b) still remained. This result may come from much slower dissolution rate of the sacrificial Co thin film compared to reduction rate of $HTeO_2^+$ ion and is in good agreement with result of OCP curve for the sacrificial Co thin film (Figure 4.1(c)).

On the other hand, cross-sectional SEM image for the electrodeposited Fe thin film with a thickness of ~3 μm is shown in Figure 4.8(a). After galvanic displacement reaction for 1 h, Te thin films with triangular and spine-shape was formed. Thickness of Te thin film in Figure 4.8(b) was measured to be ~0.4 μm. Compared to the sacrificial Ni and Co layers, much faster dissolution rate of the sacrificial Fe thin film than reduction rate of $HTeO_2^+$ ion in nitric acid solution was observed. This result is in good agreement with the result of OCP curve for the sacrificial Fe thin film in Figure 4.1(c); time to reach ~0.3 V, at which Te thin film was completely displaced by galvanic displacement reaction with the sacrificial Fe thin film, was ~15 min. Dissolution rates of the sacrificial Ni, Co, and Fe thin films in nitric acid solution (pH 1 in this study) were measured to be in order of Co≈Ni < Fe from galvanic displacement reaction. Dissolution rate of the sacrificial layer may strongly depend on surface morphologies of Te deposited galvanically on the sacrificial layers at the initial stage of galvanic displacement; after covering initially the sacrificial layer by galvanic displacement, more porous surface of Te thin film on the sacrificial layer result in faster dissolution rate of the sacrificial layer. It was also observed that surface morphologies of Te thin films with both sacrificial Ni (Figure 4.3(a) or Figure 4.6(b)) and Co (Figure 4.3(b) or Figure 4.7(d)) layers were formed in more compact than that of Te with the sacrificial Fe layer (Figure 4.3(c) or Figure 4.8(b)). In order to investigate the influence of the sacrificial Fe layer thickness on

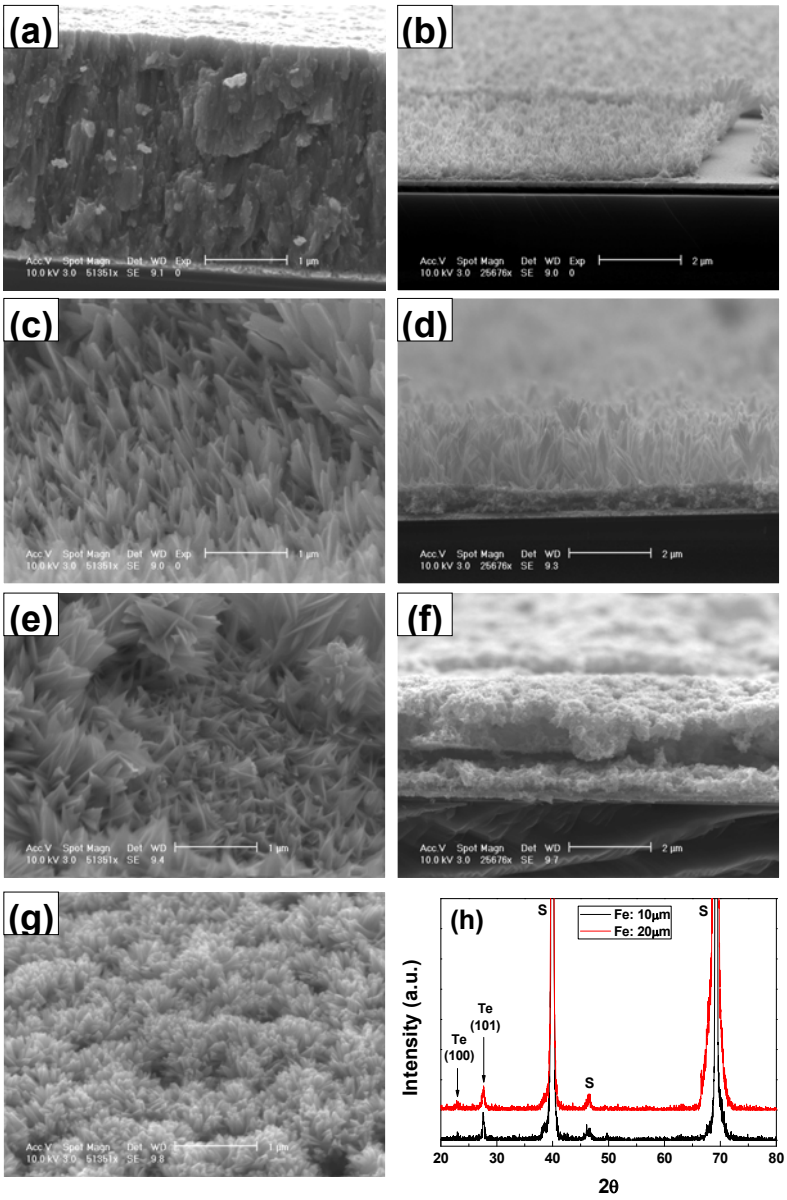

Figure 4.8. Cross-sectional SEM images of Te thin films deposited with increasing thickness of the sacrificial Fe thin film by galvanic displacement; (a) the sacrificial Fe thin film (3μm thick) electrodeposited from chloride bath, (b) Te thin film deposited by galvanic displacement with the sacrificial Fe thin film (3μm thick) for 1 hr, (c) tilted top view of Te thin film of Fig. 8(b), (d) Te thin film deposited by galvanic displacement with the sacrificial Fe thin film (10μm thick) for 1 hr, (e) tilted top view of Te thin film of Fig. 8(d), (f) Te thin film deposited by galvanic displacement with the sacrificial Fe thin film (20μm thick) for 1 hr, (g) top view of Te thin film in Fig. f(8), and (h) XRD patterns of Te thin film for Fig. 8(d) and (f).

surface morphology and thickness of Te thin film, thickness of the sacrificial Fe layer was changed from 3 to 10 and 20 μm. Thicker and more compact Te thin films by galvanic displacement were formed with increasing thickness of the sacrificial Fe layer as shown in Figure 4.8(b, d and f). From XRD analysis in Figure 4.8(h), (1 0 1) peak (JCPDS No. 36-1452) was more clearly observed compared to XRD result in Figure 4.5(c). Also, it can be suggest from XRD results that Te thin film may be very close to amorphous phase rather than crystalline phase.

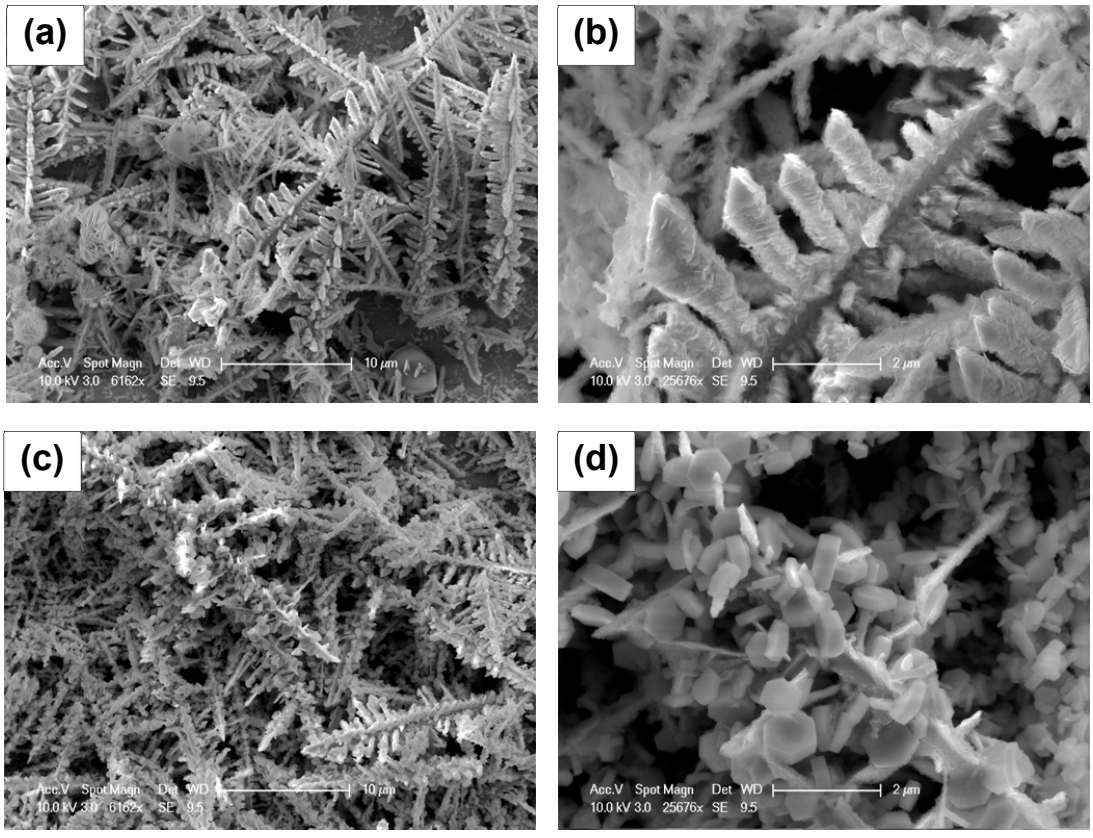

Figure 4.9. Surface morphologies of galvanically displaced Bi thin films from sacrificial Fe thin films with a thickness of (a) 10μm, low magnification (b) 10μm, high magnification (c) 20μm, low magnification and (d) 20μm, high magnification for 1hr.

To understand the effects of Fe layer thickness on the formation of Bi similar to Te, the thickness was varied from 3 to 10 and 20 μm. Although Bi was not deposited from ~3 μm thick Fe film (Figure 4.2(f)), the dendrites and hexagonal nanoplatelets of Bi were deposited via galvanic displacement with increasing film thickness (Figure 4.9). The morphology of the deposits was strongly influenced by the sacrificial film thickness where dendrites were observed with ~10 μm thick Fe thin film (Figure 4.9(a–b)). Approximately 20 μm thick Fe thin films led to the formation of hexagonal Bi nanoplatelets on the dendrites (Figure 4.9(c–d)). The X-ray diffraction patterns confirmed the formation of Bi with preferred orientation in (0 1 2) and (1 0 4) planes (JCPDS No. 05-0519) (Data not shown).

From OCP measurements (Figure 4.1) and SEM results (Figures 4.2 and 4.9 for Bi thin film, and Figures 4.6–8 for Te thin films), it was obvious that the deposited thickness of galvanically synthesized Bi or Te thin films strongly depends on type of the sacrificial thin films. Also, it can be suggested that faster dissolution rate of the sacrificial Fe thin film than reduction rate of Bi ions in galvanic displacement for Bi thin film resulted in very short step I in OCP curve as shown in Figure 4.1(a). Furthermore, extremely slow dissolution rate of the sacrificial Ni thin film may be caused absence of step I in OCP curve. On the other hand, clear step I in OCP curve was observed in galvanic displacement of Te thin film due to relatively slow dissolution rate of the sacrificial Co and Ni than reduction rate of Te ions. Therefore, galvanic displacement reactions to fabricate Bi or Te thin films could be successfully monitored by OCP measurements. Also, it is clear from the observation of cross section morphologies that type of sacrificial

materials has a strong influence on the structure of Te thin film. In other words, microstructure of the galvanically deposited thin film could be adjusted by the type of the sacrificial materials.

4.5 Conclusions

Bi and Te thin films were synthesized by galvanic displacement with three different types of the sacrificial thin films (Ni, Co and Fe). The sacrificial Ni, Co and Fe thin films were electrodeposited on Pt(nm)/Ti(nm)/SiO_2(nm)/Si substrate at room temperature without stirring. Galvanic displacement reactions to fabricate Bi and Te thin films could be successfully monitored by OCP measurements. It was clearly observed that a good agreement between OCP measurement, XRD analysis and SEM observation for the galvanically deposited Bi and Te thin films is existed. Surface morphologies and crystal structures of the as-synthesized thin films by galvanic displacement strongly depend on the type of the sacrificial materials.

Bi thin films were successfully deposited with the sacrificial Co thin films. However, only small amounts of Bi particles were deposited by galvanic displacement with the 3 μm thick sacrificial Ni thin films due to slow dissolution rate. Similar to nickel, Bi was not galvanically displaced on the 3 μm thick Fe thin films. By increasing the Fe film thickness, dendrites with hexagonal nanoplatelets of Bi were deposited.

Te thin films were successfully deposited using the sacrificial Ni, Co, and Fe thin films during galvanic displacement. Thicker sacrificial Fe films led to the formation of thicker and more compact of Te. Moreover, Te thin films exhibited different surface

morphologies compared to the surface morphologies of the sacrificial thin films. The galvanically deposited Bi and Te thin films were successfully investigated using open circuit potential (OCP), surface morphology and microstructure.

4.6 References

[1] M.S. Mart´_n-Gonzalez, A.L. Prieto, R. Gronsky, T. Sands, A.M. Stacy, J. Electrochem. Soc. 149 (2002) C546.

[2] S.B. Cronin, Y.-M. Lin, O. Rabin, M.R. Black, J.Y. Ying, M.S. Dresselhaus, P.L. Gai, J.-P. Minet, J.-P. Issi, Nanotechnology 13 (2002) 653.

[3] T.W. Cornelius, J. Brotz, N. Chtanko, D. Dobrev, G. Miehe, R. Neumann, M.E. Toimil Molares, Nanotechnology 16 (2005) S246.

[4] M. Lu, R.J. Zieve, A. van Hulst, H.M. Jaeger, T.F. Rosenbaum, S. Radelaar, Phys. Rev. B 53 (1996) 1609.

[5] F.Y. Yang, K. Liu, C.L. Chien, P.C. Searson, Phys. Rev. Lett. 82 (1999) 3328.

[6] K. Liu, C.L. Chien, P.C. Searson, K. Yu-Zhang, Appl. Phys. Lett. 73 (1998) 1436.

[7] A. Boukai, K. Xu, J.R. Heath, Adv. Mater. 18 (2006) 864.

[8] Z. Zhang, X. Sun, M.S. Dresselhaus, J.Y. Ying, J.P. Heremans, Appl. Phys. Lett. 73 (1998) 1589.

[9] N. Garcia, Y.H. Kao, M. Strongin, Phys. Rev. B 5 (1972) 2029.

[10] Y. Li, J. Wang, Z. Deng, Y. Wu, X. Sun, D. Yu, P. Yang, J. Am. Chem. Soc. 123 (2001) 9904.

[11] B. Yang, C. Li, H. Hu, X. Yang, Q. Li, Y. Qian, Eur. J. Inorg. Chem. 2003 (2003) 3699.

[12] X.-Y. Liu, J.-H. Zeng, S.-Y. Zhang, R.-B. Zheng, X.-M. Liu, Y.-T. Qian, Chem. Phys. Lett. 374 (2003) 348.

[13] J. Heremans, C.M. Thrush, Y.-M. Lin, S. Cronin, Z. Zhang, M.S. Dresselhaus, J.F. Mansfield, Phys. Rev. B 61 (2000) 2921.

[14] P. Mohanty, T. Kang, B. Kim, J. Park, J. Phys. Chem. B 110 (2006) 791.

[15] G. Xi, Y. Peng, W. Yu, Q. Tian, Cryst. Growth Des. 5 (2005) 325.

[16] B. Mayers, Y. Xia, J. Mater. Chem. 12 (2002) 1875.

[17] K. Arai, S. Hagiwara, S. Takayama, K. Murase, T. Hirato, Y. Awakura, Electrochem. Commun. 8 (2006) 605.

[18] M.R. Khairulaev, D.Kh. Dadaev, M.M. Rasulov, Russ. J. Inorg. Chem. 51 (2006) 1706.

[19] G. Henshaw, I.P. Parkin, G.A. Shaw, J. Chem. Soc. Dalton Trans. (1997) 231.

[20] F. Xiao, B.Y. Yoo, M.A. Ryan, K.-H. Lee, N.V. Myung, Electrochim. Acta 52 (2006) 1101.

[21] R. Venkatasubramanian, T. Colpitts, E. Watko, M. Lamvik, N. El-Masry, J. Cryst. Growth 170 (1997) 817.

[22] Y.J. Zhu, W.W. Wang, R.J. Qi, X.L. Hu, Angew. Chem. Int. Ed. 43 (2004) 1410.

[23] Z. Tang, Y. Wang, K. Sun, N.A. Kotov, Adv. Mater. 17 (2005) 358.

[24] X.L. Li, G.H. Cao, C.M. Feng, Y.D. Li, J. Mater. Chem. 14 (2004) 244.

[25] Q. Lu, F. Gao, S. Komarneni, Adv. Mater. 16 (2004) 1629.

[26] B. Geng, Y. Lin, X. Peng, G. Meng, L. Zhang, Nanotechnology 14 (2003) 983.

[27] D.-Y. Park, N.V. Myung, M. Schwartz, K. Nobe, Electrochim. Acta 47 (2002) 2893.

[28] C. Carraro, R. Maboudian, L. Magagnin, Surf. Sci. Rep. 62 (2007) 499.

[29] C. Carraro, L. Magagnin, R. Maboudian, Electrochim. Acta 47 (2002) 2583.

[30] C.-H. Wang, D.-C. Sun, X.-H. Xia, Nanotechnology 17 (2006) 651.

[31] V. Bansal, H. Jani, J. Du Plessis, P.J. Coloe, S.K. Bhargava, Adv. Mater. 20 (2008) 717.

[32] Y.G. Sun, B.T. Mayers, Y.N. Xia, Nano Lett. 2 (2002) 481.

[33] Y.G. Sun, B. Mayers, Y.N. Xia, Adv. Mater. 15 (2003) 641.

[34] L.A. Porter, H.C. Choi, A.E. Ribbe, J.M. Buriak, Nano Lett. 2 (2002) 1067.

[35] L.A. Porter, H.C. Choi, J.M. Schmeltzer, A.E. Ribbe, L.C.C. Elliott, J.M. Buriak, Nano Lett. 2 (2002) 1369.

[36] M.R.H. Nezhad, M. Aizawa, L.A. Porter Jr., A.E. Ribbe, J.M. Buriak, Small 1 (2005) 1076.

[37] M. Aizawa, A.M. Cooper, M. Malac, J.M. Buriak, Nano Lett. 5 (2005) 815.

[38] O.M.R. Chyan, J.-J. Chen, H.Y. Chien, J. Sees, L. Hall, J. Electrochem. Soc. 143 (1996) 92.

[39] J.S. Jeon, S. Raghavan, H.G. Parks, J.K. Lowell, I. Ali, J. Electrochem. Soc. 143 (1996) 2870.

[40] D. Niwa, T. Homma, T. Osaka, J. Phys. Chem. B 108 (2004) 9900.

[41] D. Niwa, T. Homma, T. Osaka, J. Electrochem. Soc 152 (2005) C54.

[42] C.Y. Wang, M.Y. Lu, H.C. Chen, L.J. Chen, J. Phys. Chem. C 111 (2007) 6215.

[43] Y. Sun, Y. Xia, Adv. Mater. 16 (2004) 264.

[44] J. Chen, B. Wiley, J. McLellan, Y. Xiong, Z.-Y. Li, Y. Xia, Nano Lett. 5 (2005) 2058.

[45] F. Xiao, B.Y. Yoo, K.-H. Lee, N.V. Myung, J. Am. Chem. Soc. 129 (2007) 10068.

[46] C.H. Chang, Y.W. Rheem, Y.-H. Choa, D.-Y. Park, N.V. Myung, Electrochim. Acta, 55 (2010) 1072

[47] http://www.webelements.com.

[48] M. Schwartz, in: R.F. Bunshah (Ed.), Handbook of Deposition Technologies for Films and Coatings, Second ed., Noyes Publications, Park Ridge, NJ, 1994, p. 524.

[49] Electroless plating: fundamentals and applications, in: G.O. Mallory, J.B. Hajdu (Eds.), American Electroplaters and Surface Finishers Society, Orlando, Florida, 1990, p. 111, 476.

[50] T. Homma, Y. Kita, T. Osaka, J. Electrochem. Soc. 147 (2000) 160.

[51] T. Homma, K. Inoue, H. Asai, K. Ohrui, T. Osaka, IEEE Trans. Magn. 27 (1991) 4909.

[52] A. Brenner, D.W. Couch, E.K. Williams, J. Res. Nat. Bur. Stand. 44 (1950) 109.

Chapter 5

Electrochemical Synthesis of Te Nanotubes

5.1 Abstract

Tellurium nanotubes with controlled diameter and wall thickness were synthesized by galvanic displacement of cobalt nanowires and their temperature dependent field effect transistor and magnetoresistance properties were systematically investigated. The nanotube diameter was slightly larger than the sacrificial cobalt nanowire diameter with a wall thickness of range from 15 to 30 nm depending on the diameter of cobalt nanowires. Te nanotubes show p-type semiconducting property with the field effect carrier mobility of approx. 0.01cm^2/Vs which is relatively lower than other 1D nanostructure. Low mobility might be attributed to porous morphology with small grain size (<10 nm). Temperature dependent mobility also exhibiting a Conwell–Weisskopf relationship to temperatures below 250 K, indicating that the dominant scattering sites are ionized impurity centers. Unique MR behavior was observed from nanotube with a maximum magnetoresistance ratio of 37 % at 260 K.

5.2 Introduction

Tellurium is a p-type semiconductor with a direct band gap energy of 0.35 eV at room temperature. It has been applied for high-efficiency photoconductors [1], piezoelectric devices [2], and carbon monoxide [3] and ammonia [4] gas sensors. Additionally,

tellurium and its alloys are considered important semiconductor materials for thermoelectric generators and coolers because of their high thermopower [5]. Unfortunately, the thermoelectric figure of merit of pure bulk tellurium is relatively low because of its high thermal conductivity. However, one-dimensional (1D) nanostructures have been proposed to increase the thermoelectric figure of merit by decreasing thermal conductivity via phonon scattering. Thus, the synthesis of one-dimensional tellurium nanostructures is of great interest. Furthermore, Te nanotubes, in particular, are attractive 1D nanostructures as their wall thickness allows their physical properties to be tuned by much smaller characteristic lengths compared to their diameter. Previous reports have synthesized Te nanotubes via hydro/solvo-thermal [6,7] and physical vapor deposition [8]. However, these processes are limited by low yield (<30 %) and inability to produce high aspect ratio nanotubes, which is essential for nanostructure-based thermoelectric devices. Alternatively, galvanic displacement reactions, which are induced by the difference in redox potentials between materials, are site-specific electrochemical processes producing structural features determined by those of the sacrificial material. Galvanic displacement reaction is simple and versatile route to create nanostructures with controllable hollow interiors and porous walls. The requirement for achieving such hollow nanostructures is the availability of noble metal ions in the presence of less-noble nanoconstructures. Various hollow metal nanostructures including nanocubes and nanotubes have been synthesized via this reaction [9]. Recently, we demonstrated the synthesis of semiconducting nanostructures using galvanic displacement [10]. In this chapter, Te nanotubes with controlled diameters and wall thickness were systematically

synthesized by galvanic displacement of sacrificial cobalt nanowires. The nanotube diameter was adjusted by the diameter of the sacrificial nanowires. Temperature dependent electron- and magneto-transport properties of single tellurium nanotube were also investigated.

5.3 Experimental Section

The sacrificial cobalt nanowires with average diameters of 70, 120 and 220 nm were synthesized by a template-directed electrodeposition method using polycarbonate membranes as scaffolds. A gold thin film with a thickness of 200 nm was deposited on one side of the template with an Emitech K550 table-top sputter to serve as the seed layer for the electrodeposition of cobalt nanowires. The nanowires were galvanostatically deposited by applying current density of 5mA/cm^2 using EG&G PAR VMP2 multichannel potentio/galvanostat. The cobalt electrolyte consisted of 1 M $CoCl_2$ + 1 M $CaCl_2$ at pH of 3. After electrodeposition, the nanowires were released in isopropyl alcohol by dissolving the template in 1-methyl-2-pryrrolidinone. Tellurium nanotubes were synthesized by galvanically displacing the cobalt nanowires. The galvanic displacement electrolyte (0.01 M $HTeO_2^+$ + 1 M HNO_3, pH of 1) for the tellurium nanotubes was prepared by dissolving TeO_2 in concentrated nitric acid followed by addition of deionized water to reach the final volume. Electron- and magneto-transport characterization of single tellurium nanotubes required a back gated two-point electrical contact configuration. To create a robust electrical and mechanical contact between nanowire and microfabricated electrodes, device fabrication began by dispersing

suspended cobalt nanowires (average diameter of 220 nm) on a boron doped silicon substrate (ρ = 0.01 – 0.02 Ωcm) coated with a HfO_2 dielectric layer (150 nm thickness). After assembly of nanowires, Au/Cr electrodes (200 μm × 200 μm, t_{Au} = 280 nm, tCr =20 nm) with 3 μm gap were fabricated on top of the nanowires by e-beam evaporation and standard lift-off lithography (Figure 5.1). Substrates with contacted cobalt nanowires were immersed in the tellurium electrolyte to form tellurium nanotubes. The reaction was carried out with no agitation at ambient temperature and a fixed time of 30 min. The temperature dependence of electro- and magneto-transport properties of single tellurium nanotube were measured using a source-measureunit (Keithley 2636) and a physical property measurement system (PPMS, Quantum Design), respectively.

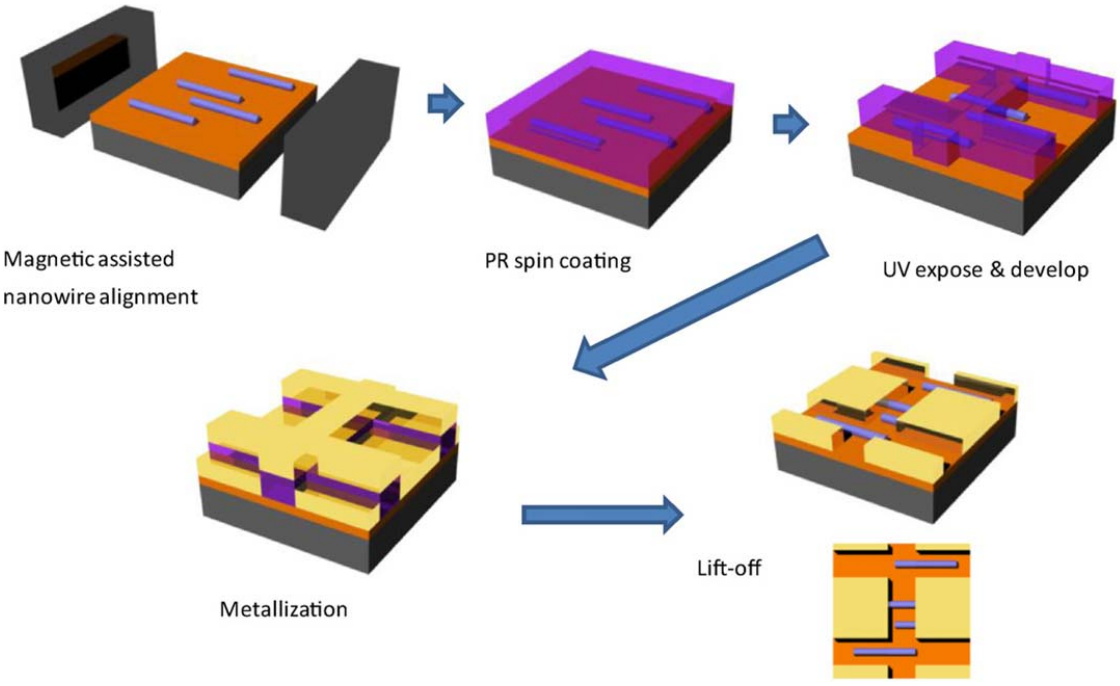

Figure 5.1. Schematic representation of fabrication procedure to create top areal electrode contact on nanowires.

5.4 Results and discussion

5.4.1 Effect of Diameter of Sacrificial Co Nanowires

Figure 5.2 shows the transmission electron microscopy (TEM) image of electrodeposited cobalt nanowires with average diameters of 70 nm and tellurium nanotubes subsequently synthesized from these wire by galvanic displacement. Selected area electron diffraction (SAED) pattern of the nanowires indicates a nanocrystalline microstructure (Figure 5.2(a)). When cobalt nanowires are immersed into the acidic nitric solution containing $HTeO_2^+$ ions, cobalt nanowires are galvanically displaced to form tellurium, because of the difference in the redox potentials (i.e., $Co^{2+} + 2e^- \rightarrow Co$ ($E^0 = -0.28$ V vs NHE) and $HTeO_2^+ + 3H^+ + 4e^- \rightarrow Te + 2H_2O$ ($E^0 = +0.551$ V vs NHE)) [11], where the galvanic displacement of cobalt nanowires to tellurium nanotubes can be represented as follows:

$$HTeO_2^+(aq) + 3H^+(aq) + 2Co^0(s) \rightarrow Te^0(s) + 2H_2O + 2Co^{2+} \quad (1)$$

Homogeneous tellurium nanotubes with well-defined void spaces were formed as shown in Figure 5.2(b) where the SAED pattern also confirms the formation of tellurium nanotubes. The final outer diameter of the tellurium nanotubes was slightly larger than the cobalt nanowires. These results are in accord with the proposed mechanism for tube formation, in which the displacement reaction occurs at the surface of the nanowire creating an incomplete thin tellurium sheath at the cobalt nanowire surface. The reactants and products diffuse across the porous tellurium sheath, building a continuous tellurium

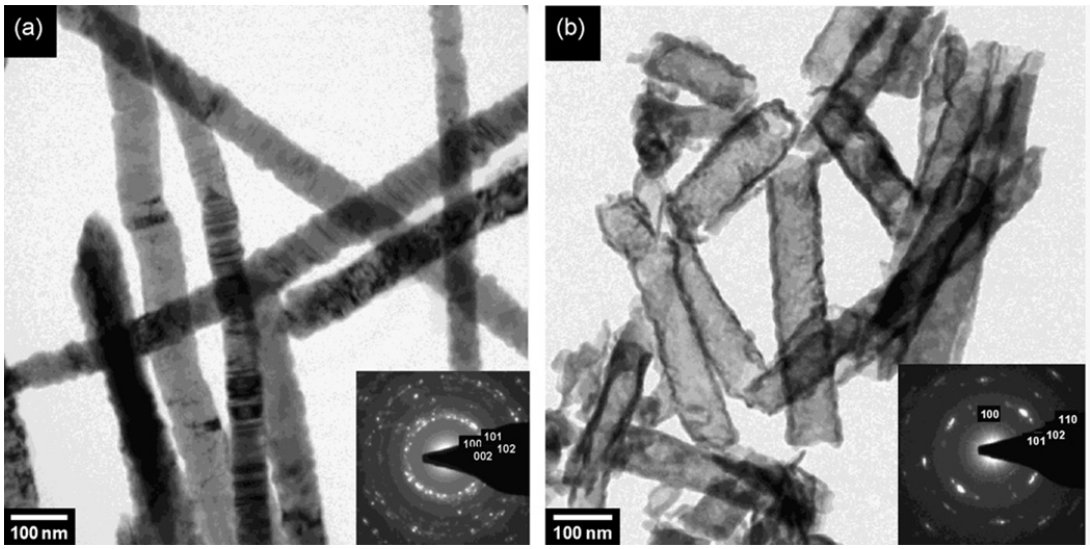

Figure 5.2. TEM images and selected area electron diffraction patterns of (a) electrodeposited cobalt nanowires and (b) tellurium nanotubes.

nanotube on the exterior wall of the initial tellurium sheath. The tellurium nanotubes also have a nanocrystalline microstructure with a grain size <10 nm and wall thickness around 15 nm which was measured using TEM images. The nanocrystalline microstructure of the Te nanotube implies the crystallinity of the sacrificial Co nanowire may be induced upon the Te nanotube during the displacement reaction. Figure 5.3 shows the histogram of outer diameter distribution of sacrificial cobalt nanowires and tellurium nanotubes where the average diameter of the Te nanotubes were determined to be 85, 140, and 250 nm for sacrificial cobalt nanowires diameters of 70, 120 and 220 nm, respectively. As expected, the outer diameter of Te nanotubes was greater than the diameter of sacrificial cobalt nanowire. In addition, the wall thickness increased from 15, 20 and 30 nmwhich increased in the diameter of cobalt nanowires from 70, 120, and 220 nm. These clearly

indicated that the tube diameter and wall thickness can be tuned by adjusting the diameter of sacrificial nanowires.

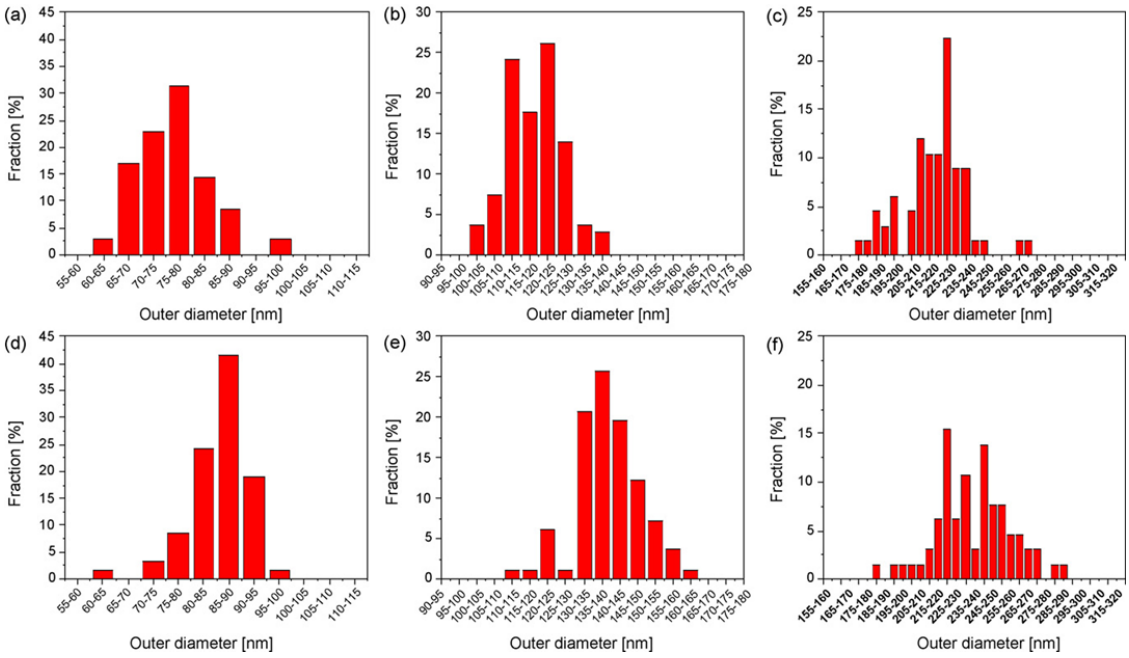

Figure 5.3. Outer diameter distribution of Co nanowires (a–c) and Te nanotubes (d–f). The mean diameter of Co nanowires are (a) 70, (b) 120, and (c) 220 nm, respectively.

5.4.2 Electron- and magneto-transport Property

To determine the thermal activation energy of synthesized Te nanotubes, temperature dependent electrical resistance were measured from 20 to 300 K. Figure 5.4(a) shows the Arrhenius plot of temperature dependent resistance of a single tellurium nanotube (220 nm in diameter). Two linear regions are observed with activation energies of 87 and 6.8 meV obtained for temperatures above and below 200 K. These values fall within the range of activation energies, between 6 and 178 meV, reported by Goswami and Ojha [12] for thermally evaporated tellurium thin films with variation in film thickness and

fabrication conditions. The transition temperature (200 K) of tellurium nanotubes is also similar to that of tellurium thin films. To determine semiconducting properties of single Te nanotubes, field effect transistor (FET) transfer characteristics were measured. Figure 5.4(b) shows a series of the source-drain current (I_{SD}) versus voltage (V_{SD}) curves measured at different gate voltage (V_G) from −20 to +20 V with a step of 10 V under ambient condition. The back gate was formed by contacting highly doped silicon substrate back-side with metal electrode using conductive silver paint (PELCO Conductive Silver 187). The I_{SD}–V_{SD} curves at different V_G are all linear, which indicate ohmic contact between gold electrodes and Te nanotube. The dependence of I_{SD}–V_{SD} on the V_G indicates that the synthesized tellurium nanotube is a p-type semiconductor. The transfer characteristics of the tellurium nanotube are shown in Figure 5.4(c) with fixed V_{DS} of 1V. The conductance of the tellurium nanotube decreased with the increase in V_G indicating the tellurium nanotube has typical characteristics of a p-channel semiconductor field effect transistor (FET). In addition, we investigated the carrier mobilities at temperatures from 50 to 300 K using a cold-finger cryogenic system (Janis CCS-350SH). The mobility of the carriers can be estimated from the transconductance of the FET, $dI_{SD}/dV_G = \mu(C/L^2)V_{SD}$, where μ is the carrier mobility. The approximate nanotube capacitance $C = 2\pi\varepsilon\varepsilon_0 L / \ln(2h/r)$, where ε is dielectric constant of HfO_2, h is the thickness of the HfO_2 layer, L is the nanotube length, and r is radius of tellurium nanotube [13]. The temperature dependence of carrier mobility of tellurium nanotube (Figure 5.4(d)) shows that the field effect carrier mobility monotonically increased with increase in temperature up to 250 K, and slightly decreased with further increases in

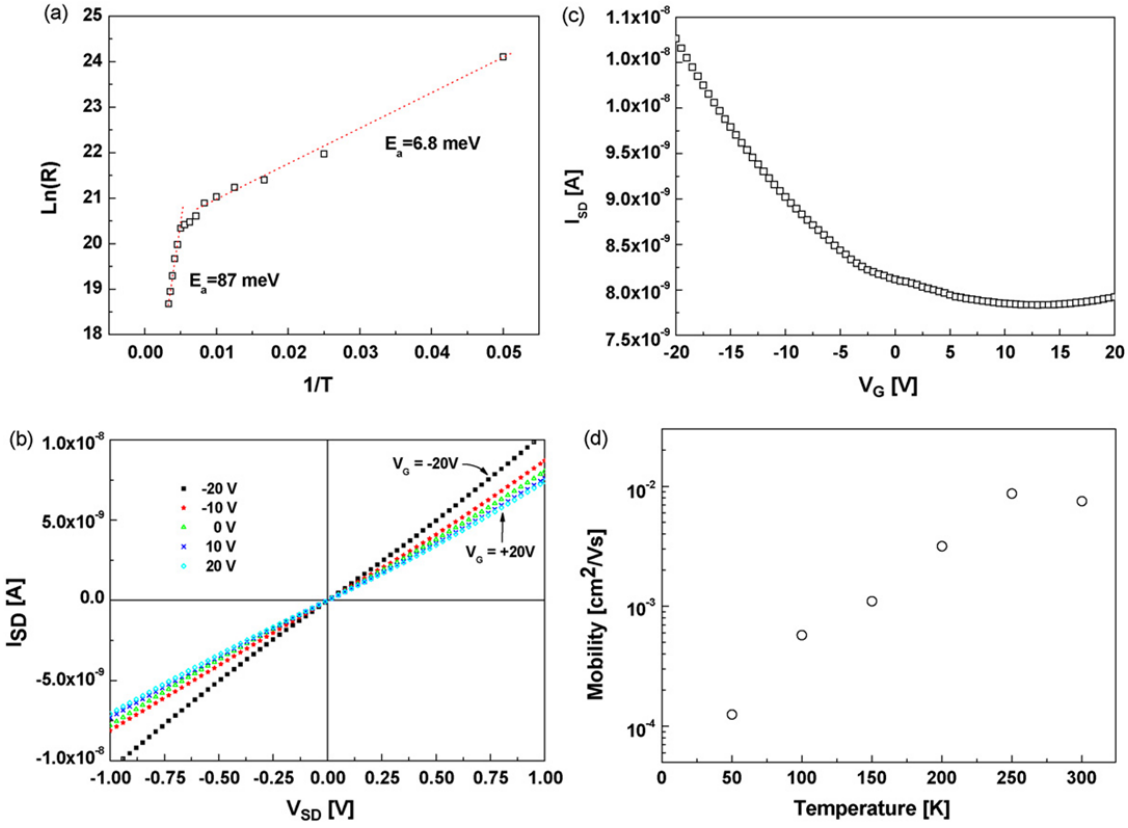

Figure 5.4. Electron transport properties of tellurium nanotube device; (a) temperature dependence of electrical resistance, (b) the gate voltage dependent I_{SD}–V_{SD} curves, (c) I_{SD}–V_G characteristics measured at V_{SD} = 1V, and (d) temperature dependence of field effect carrier mobility.

temperature. The field effect mobility at 300 K was approx. 0.01 cm^2/Vs which is relatively lower than other reported semiconducting nanostructures. For example, field effect mobility of single-walled carbon nanotubes network is in the range of 0.1–10 cm^2/Vs [14]. The lower mobility might be attributed to porous morphology of Te nanotubes with small grain size. The field effect carrier mobility below 250 K seems to obey the Conwell–Weisskopf relation [15], indicating that ionized impurity center scattering is the dominant factor in this region [16]. In the temperature region above 250

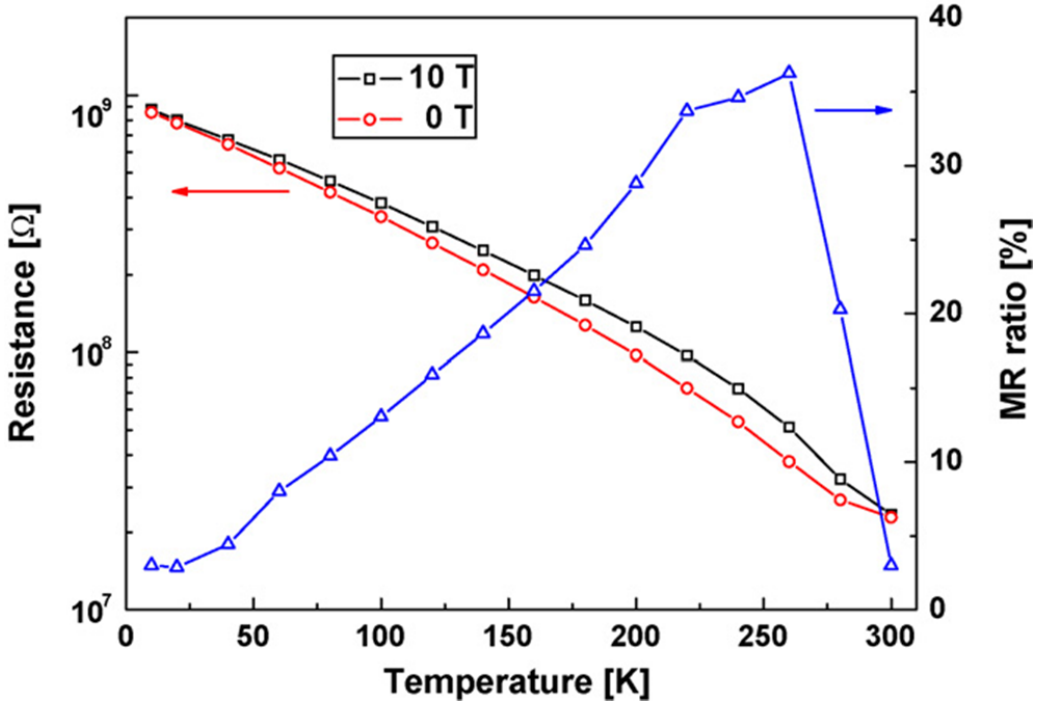

Figure 5.5. Temperature dependence of resistance of tellurium nanotube device in the absence and presence of external magnetic field (H= 10 T) inthe transverse direction. The triangle symbol shows the temperature dependence of the magnetoresistance ratio of the nanotube device.

K, the mobility is affected by lattice scatteringmodefollowing $T^{-3/2}$ law. The field effect carrier mobility was estimated based on transconductance. Magnetoresistance (MR) properties of tellurium nanotube in the temperature range from 10 to 300 K were measured using a PPMS with a two-probe contact. The temperature dependence of resistance with zero magnetic field and applied field of H=10T, and MR ratio are shown in Figure 5.5. The magnetic field was applied in the transverse direction. The resistance curves show the ordinary semiconductor properties with higher resistance under an applied magnetic field at all temperatures. The MR ratio has maximum value of 37 % at 260 K and decreases gradually with decreasing temperature. It is known that the

transverse magnetoresistance of the medium with one kind of carrier increases with magnetic field as $(\mu H)^2$ relation, where μ and H are the carrier mobility and magnetic field strength, respectively [17]. However, the MR mechanism of tellurium is not clear at this moment [18–20].

5.5 Conclusions

For the first time, we reported the synthesis of Te nanotubes with controlled diameter and wall thickness from sacrificial Co nanowires by galvanic displacement reaction at room temperature. The diameter and wall thickness of the nanotubes were controlled by adjusting the diameter of the sacrificial nanowires. The length can be also controlled by adjusting the length of sacrificial nanotube. As expected, the diameter and wall thickness of nanotube increased with increases in the diameter of cobalt nanowires. Assynthesized Te nanotubes show nanocrystalline microstructure with an average grain size below 10 nm. The wall thickness of nanotubes ranged from 15 to 30 nm depending on the diameter of cobalt nanowire. Synthesized nanotubes show typical p-type semiconductor with field effect mobility of approx. 0.01 cm^2/Vs. In addition, unique MR behavior was observed from single Te nanotube.

5.6 References

[1] Y. Wang, Z. Tang, P. Podsiadlo, Y. Elkasabi, J. Lahann, N. Kotov, Advanced Materials 18 (2006) 518.

[2] S. Fukuda, T. Shiosaki, A. Kawabata, Ultrasonics Symposium (1979) 9.

[3] D. Tsiulyanu, S. Marian, H.D. Liess, Sensors and Actuators B: Chemical 85 (2002) 232.

[4] S. Sen, K.P. Muthe, N. Joshi, S.C. Gadkari, S.K. Gupta, Jagannath, M. Roy, S.K. Deshpande, J.V. Yakhmi, Sensors and Actuators B: Chemical 98 (2004) 154.

[5] P. Bodiul, N. Bondarchuk, T. Huber, L. Konopko, A. Nikolaeva, O. Botnari, 25th International Conference on Thermoelectrics (2006) 607.

[6] G. Xi, Y. Peng, W. Yu, Y. Qian, Crystal Growth and Design 5 (2005) 325.

[7] H. Zhang, D. Yang, X. Ma, D. Que, Journal of Crystal Growth 289 (2006) 568.

[8] S. Sen, U.M. Bhatta, V. Kumar, K.P. Muthe, S. Bhattacharya, S.K. Gupta, J.V. Yakhmi, Crystal Growth and Design 8 (2008) 238.

[9] X. Lu, J. Chen, S.E. Skrabalak, Y. Xia, Proceedings of the Institution of Mechanical Engineers, Part N: Journal of Nanoengineering and Nanosystems 221 (2007) 1.

[10] F. Xiao, B. Yoo, K.H. Lee, N.V. Myung, Journal of the American Chemical Society 129 (2007) 10068.

[11] D.R. Linde, W.M. Haynes, CRC Handbook of Chemistry & Physics, CRC Press, Cleveland, OH, 2006.

[12] A. Goswami, S.M. Ojha, Thin Solid Films 16 (1973) 187.

[13] R. Martel, T. Schmidt, H.R. Shea, T. Hertel, P. Avouris, Applied Physics Letters 73 (1998) 2447.

[14] J.H. Lim, N. Phiboolsirichit, S. Mubeen, M.A. Deshusses, A. Mulchandani, N.V. Myung, Electroanalysis, Epub ahead of print.

[15] E. Conwell, V.F. Weisskopf, Physical Review 77 (1950) 388.

[16] R.W. Dutton, R.S. Muller, Proceedings of the IEEE 59 (1971) 1511.

[17] J.L. Olsen, Electron Transport in Metals, Interscience Publishers a division of John Wiley & Sons, New York, London, 1962.

[18] C. Albers, H. Gertig, Physica Status Solidi (a) 34 (1976) K125.

[19] X.-L. Li, G.-H. Cao, C.-M. Feng, Y.-D. Li, Journal of Materials Chemistry 14 (2004) 244.

[20] K. Takita, K. Suzuki, S. Tanaka, Journal of the Physical Society of Japan 34 (1973) 677.

Chapter 6

Electrochemical Synthesis of Pb_xTe_y Nanostructures

6.1 Abstract

In this chapter, we demonstrated a simple methodology for synthesizing novel lead telluride (Pb_xTe_y) nanostructures with tunable composition and surface morphology by galvanic displacement reaction. Furthermore, a systematic investigation was performed to understand the effects of $[Pb^{2+}]/[HTeO_2^+]$ ratio in the electrolyte, the thickness of sacrificial layer, and the reaction time on the surface morphology and film composition of Pb_xTe_y thin films. The deposited content can be controlled from Te-rich ($Pb_{20}Te_{80}$) to Pb-rich ($Pb_{69}Te_{31}$), and its surface morphology varied from x-shaped, cucumber-like, flower-like to dendrite structures. The time-dependent galvanic displacement reaction was also investigated to understand the growth process of Pb_xTe_y nanostructures. TEM analysis showed that Pb_xTe_y grew in a single crystalline face-centered cubic (FCC) structure along the [100] and [110] directions.

6.2 Introduction

Lead chalcogenides (e.g., PbS, PbSe and PbTe) are important IV-VI semiconductor materials for their potential applications in thermoelectric and infrared (IR) photoelectric devices, due to their narrow band gaps, large exciton Bohr radius, and low thermoconductivity [1-4]. As one of several promising lead chalcogenide materials, lead

telluride (PbTe) is a direct band gap semiconductor with a narrow band gap (E_g = 0.31 eV at 300K) and a relatively large exciton Bohr radius (r_B = 46 nm). Furthermore, its semiconductor conductivity type (*e.g.* n-type or p-type) can be tuned by controlling the deposit composition in proportion to its stoichiometry (Pb-rich PbTe is n-type, while Te-rich PbTe is p-type). These properties of PbTe lead to a high thermoelectric figure of merit (ZT) in the intermediate temperature range of up to 1000 K, a quantum confinement of the carriers, and an optical tunability in the mid- and far-infrared spectral regime through adjustment of alloy composition [5-7]. As a consequence, PbTe is a good candidate material for various optoelectric and thermoelectric devices, including IR detectors, laser diodes, optical switches, and thermoelectric power generators [8-11].

Various PbTe nanostructures, such as quantum dots, nanorods, nanowires, and nanotubes, have been synthesized by wet-chemical techniques which include sonoelectrochemistry, hydrothermal and solvothermal synthesis, and electrodeposition [12-17]. Among these methods, galvanic displacement is a cost-effective, simple, and versatile approach compared to conventional methods since this technique provides a critical key for the formation of composite Pb_xTe_y nanostructures with easily tunable composition and surface morphology. Specifically, galvanic displacement occurrs due to the difference in redox potential between sacrificial materials and metal ions in the electrolyte, and thus the composition and surface morphology can be controlled by adjusting experimental conditions such as the electrolyte composition and reaction time, as well as modulating the sacrificial materials (*i.e.* material type and thickness). There has been no reported literature regarding work done on synthesis of lead chalcogenide

semiconductors (Pb_xTe_y) by galvanic displacement reaction, other than bismuth chalcogenide materials (Bi_xTe_y [18-20]. Consequently, systematic investigation of the synthesis of Pb_xTe_y nanostructures by galvanic displacement reaction has an intense scientific interest.

In this chapter, Pb_xTe_y thin films with nanostructures were synthesized by galvanic displacement reaction from sacrificial Co thin films in acidic nitrate baths. Their surface morphology and film composition were systematically investigated by varying the ratio of $[Pb^{2+}]/[HTeO_2^+]$ in the electrolyte, changing the thickness of sacrificial layer, and modifying the reaction time.

6.3 Experimental Section

The sacrificial Co thin films were galvanostatically electrodeposited from the 1 M $CoCl_2$ in 1 M $CaCl_2$ electrolyte on Pt-coated $Ti/SiO_2/Si$ substrate at room temperature without agitation. The electrodeposition was carried out using a Princeton Applied Research Potentiostat (VMP2) at current density of 5 mA cm^{-2} with a traditional three-electrode cell. A platinum substrate with a surface area of 1 cm^2, a saturated calomel electrode (SCE) and a platinum-coated titanium anode were used as a working, reference and counter electrode, respectively. The electrolyte pH was maintained at 3 with HCl and NaOH.

For galvanic displacement, electrodeposited Co thin films were immersed into the electrolyte containing 10 mM $HTeO_2^+$ with varying Pb^{2+} concentration from 50 to 500 mM. Nitric acid concentration was fixed at 1 M and the solution pH was maintained at

pH 1. Open circuit potential (OCP) during galvanic displacement was continuously measured in a three-electrode cell to monitor the effects of $[Pb^{2+}]/[HTeO_2^+]$ in the electrolyte.

Scanning electron microscope (SEM, XL30-FEG, Phillips) imaging and energy-dispersive spectroscopy (EDS, EDAX, Phoenix) were used to examine the surface morphology and film composition of samples. Phase identification of the thin films was carried out by X-ray diffractometer (XRD, D8 Advance Diffractometer, Bruker) measurement with Cu Kα radiation (operating at 40 kV). TEM and HRTEM images were obtained with transmission electron microscopy (TEM, JEM-2100F, JEOL) operated at 300 kV acceleration to investigate the crystallography of Pb_xTe_y nanostructures.

6.4 Results and Discussion

6.4.1 Electrochemical Study and Effect of Ratio of $[Pb^{2+}]/[HTeO_2^+]$

The open circuit potential (OCP) was measured to monitor the reaction during the galvanic displacement between sacrificial Co thin films and metal ions (Pb^{2+} and $HTeO_2^+$) as shown in Figure 6.1(a). The electrolyte for galvanic displacement consisted of 10 mM $HTeO_2^+$ + 1M HNO_3 with varying Pb^{2+} concentration from 50 to 500 mM. As shown in this figure, the three-step reaction is clearly observed in all ratios of $[Pb^{2+}]/[HTeO_2^+]$ during galvanic displacement, which is consistent with the typical reaction step reported in previous works [19-21]. When the galvanic deposition (reduction of Pb^{2+} and $HTeO_2^+$ ions) occurred simultaneously with oxidation of sacrificial Co thin films, OCP curves started from a negative potential at initial stage of reaction.

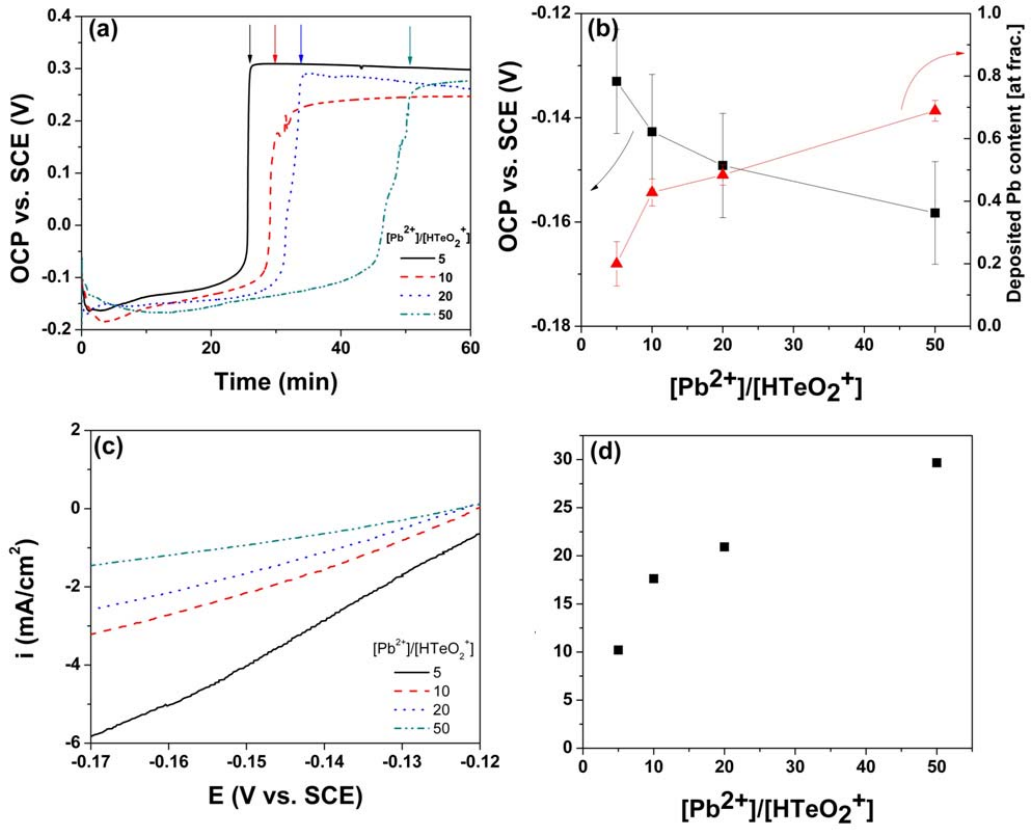

Figure 6.1. Dependence of (a) open circuit potentials (OCP), (b) steady-state potential in the first step and deposited Pb content in Pb_xTe_y thin films, and (c) polarization curves and (d) polarization resistance (R_p) on the different ratio of $[Pb^{2+}]/[HTeO_2^+]$ in the electrolyte. $[HTeO_2^+]$ was fixed at 10 mM while varying $[Pb^{2+}]$ concentration from 50 to 500 mM.

Then, the potential sharply increased to a positive value in the second step as a result of an increase in cathodic current due to the reduction of Pb^{2+} and $HTeO_2^+$ ions and a decrease in anodic current (oxidation) caused by covering deposited Pb_xTe_y thin films onto sacrificial Co thin films. In the final step, the positive steady-state value was reached, which indicated the completion of galvanic displacement. Among these steps, the negative potential (mixed potential) in the first step is the most important factor since

it acts as the driving force for galvanic displacement reaction between the sacrificial Co thin films and metal ions (Pb^{2+} and $HTeO_2^+$). For this galvanic displacement of Pb_xTe_y, the mixed potential consisted of the oxidation potential of sacrificial thin films (*i.e.* Co^{2+}/Co^0: $E^0 = -0.28$ V vs SHE) and the reduction potential of metal ions (*i.e.* Pb^{2+}/Pb^0: $E^0 = -0.13$ V vs. SHE, $HTeO_2^+/Te^0$: $E^0 = 0.551$ V vs. SHE). Also, the overall process can be represented as the following equation [22]:

$$HTeO_2^+ (aq) + Pb^{2+} (aq) + 3Co^0 (s) + 3H^+ (aq) \rightarrow$$
$$PbTe (s) + 3Co^{2+} (aq) + 2H_2O (aq) \quad (1)$$

Further analysis of mixed potential in the first step of OCP curves was performed to understand the effects of the ratio of $[Pb^{2+}]/[HTeO_2^+]$ in the electrolyte on galvanic displacement. Figure 6.1(b) shows the dependence of steady-state potential (mixed potential) and deposited Pb content on the different ratios of $[Pb^{2+}]/[HTeO_2^+]$ in the electrolyte. The mixed potential gradually decreased from −0.13V to −0.16V vs. SCE as Pb^{2+} ion concentration was increased from 50 to 500 mM in the bath. Coincidentally, the galvanically deposited Pb content in Pb_xTe_y thin film increased as mixed potential decreased. The lowest deposited Pb content ($Pb_{20}Te_{80}$) was obtained from the lowest mixed potential (−0.13V vs. SCE), whereas the highest Pb content ($Pb_{69}Te_{31}$) in Pb_xTe_y thin film was measured at the highest mixed potential (−0.16V vs. SCE). Furthermore, it was found that near stoichiometric PbTe deposits could be acquired from the electrolyte containing 200 mM Pb^{2+} + 10 mM $HTeO_2^+$ + 1 M HNO_3, with a mixed potential of -

0.15V vs SCE. In other words, the driving force of galvanic displacement could be controlled by adjusting the ratio of $[Pb^{2+}]/[HTeO_2^+]$ in the electrolyte, resulting in a change of the mixed potential. Consequently, it contributed to the modulation of composition in Pb_xTe_y thin films during the galvanic displacement from sacrificial Co thin films. This relationship between mixed potential and deposited Pb content can be explained by two-step deposition mechanism, having critical effects on the composition of the alloy. The $HTeO_2^+$ ions were first reduced to deposit Te(s) on the sacrificial layer, followed by the underpotential deposition (UPD) of Pb^{2+} ions with first deposited Te precursor to form the PbTe compound [23,24].

$$HTeO_2^+ (aq) + 3H^+ (aq) + 4e^- \rightarrow Te (s) + 2H_2O (aq) \quad (2)$$

$$Pb^{2+} (aq) + Te (s) + 2e^- \rightarrow PbTe (s) \quad (3)$$

The greatest increase in cathodic current was caused by underpotential deposition of Pb onto first deposited Te(s) (eq 3) compared to overpotential deposition of Te(s) (eq 2) in the region of mixed potential between −0.13 and −0.16V vs. SCE [24]. Therefore, the decrease of the mixed potential resulting from increasing in the ratio of $[Pb^{2+}]/[HTeO_2^+]$ in the electrolyte can be attributed to an increase in the deposited Pb content in Pb_xTe_y thin films. These tendencies are consistent with a previous report of galvanically deposited Bi_xTe_y (*e.g.* thin films, nanowires, and nanotubes) from a sacrificial iron group (*i.e.* Ni, Co and Fe), where the deposited Bi content increased up to 40% when the ratio of $[Bi^{3+}]/[HTeO_2^+]$ increased from 0 to 20 mM [18,20-21]. Therefore, it is implied that

the composition of Pb_xTe_y thin films can be tuned by simply varying the ratio of electrolyte composition for galvanic displacement.

As represented by the arrow in Figure 6.1(a), the completion of galvanic displacement reaction can be clearly observed in the second step of OCP curves with different ratios of $[Pb^{2+}]/[HTeO_2^+]$ in the electrolyte. The galvanic deposition time for Pb_xTe_y thin films with varying electrolyte composition was 25, 29, 34, and 50 min, respectively, which follows the same pattern as the ratio of $[Pb^{2+}]/[HTeO_2^+]$. This gradual increase of galvanic deposition time may result in the under reaction rate control of displacement process. The polarization curves were further investigated for galvanic displacement between sacrificial Co thin films and metal ions (Pb^{2+} and $HTeO_2^+$) by measuring various ratios of $[Pb^{2+}]/[HTeO_2^+]$ in the range of ± 0.6V vs. OCP (mixed potential) at a scan rate of 1 mV s^{-1}. As shown in Figure 6.1(c), the polarization curves are shifted towards positive current density as the ratio of $[Pb^{2+}]/[HTeO_2^+]$ in the electrolyte increases, indicating that the measured curves showed them to be dependent of ratio of electrolyte. Based on the approximately linear polarization behavior, the polarization resistance (R_p) was determined graphically using the Stern-Geary equation [25],

$$Rp = \frac{1}{2.303 i_{corr}} \frac{b_a b_c}{(b_a + b_c)} \tag{4}$$

where i_{corr} is corrosion current density (mA cm^{-2}), b_a and b_c are anodic/cathodic Tafel slops (V), and R_p is polarization (corrosion) resistance (Ω cm^2). Since polarization

resistance behaves like a resistor for the oxidation of sacrificial materials, the high R_P of a metal implies high corrosion resistance which means the dissolving rate (oxidation) of sacrificial Co thin films is slow compared to the reduction of metal ions (Pb^{2+} and $HTeO_2^+$) during galvanic displacement reactions. This lead to increase the reaction time with higher R_p. As shown in Figure 6.1(d), R_p increased continuously from 10 to 30 Ω cm^2 as a function of electrolyte composition, resulting in an increase of galvanic deposition time from the electrolyte containing relatively higher ratio of $[Pb^{2+}]/[HTeO_2^+]$. The detail electrolyte composition-dependent corrosion rate, therefore, has a considerable factor to galvanic displacement reaction and merits for future study.

The effect of the $[Pb^{2+}]/[HTeO_2^+]$ ratios on the surface morphology of Pb_xTe_y thin films are shown in Figure 6.2. SEM images of Pb_xTe_y nanostructures were obtained by galvanic displacement from 3μm thick sacrificial Co thin films in a fixed 10 mM $HTeO_2^+$ + 1 M HNO_3 electrolyte with varying Pb^{2+} concentration from 50 to 500 mM. Figure 6.2(a) represents the novel Pb_xTe_y nanostructures with many x-shaped platse when the concentration of Pb^{2+} is at 50 mM. The x-shaped nanostructures have a length ranging from 1 to 2μm (inset, Figure 6.2(a)), and each nanostructure is stacked with another x-shaped plate to longitudinal directions of up to a few μm in thickness. Furthermore, the stacked nanoplates were connected at the center to form flower shaped structures. Figure 6.2(b) shows that smaller sizes (hundreds of nm length) of x-shaped Pb_xTe_y with dendritic structures are formed in the electrolyte as the concentration of Pb^{2+} is increased to 100 mM. When the concentration of Pb^{2+} increased from 200 to 500 mM, the feather-like dendrites of Pb_xTe_y were grown with an average size of tens of micrometers (Figure

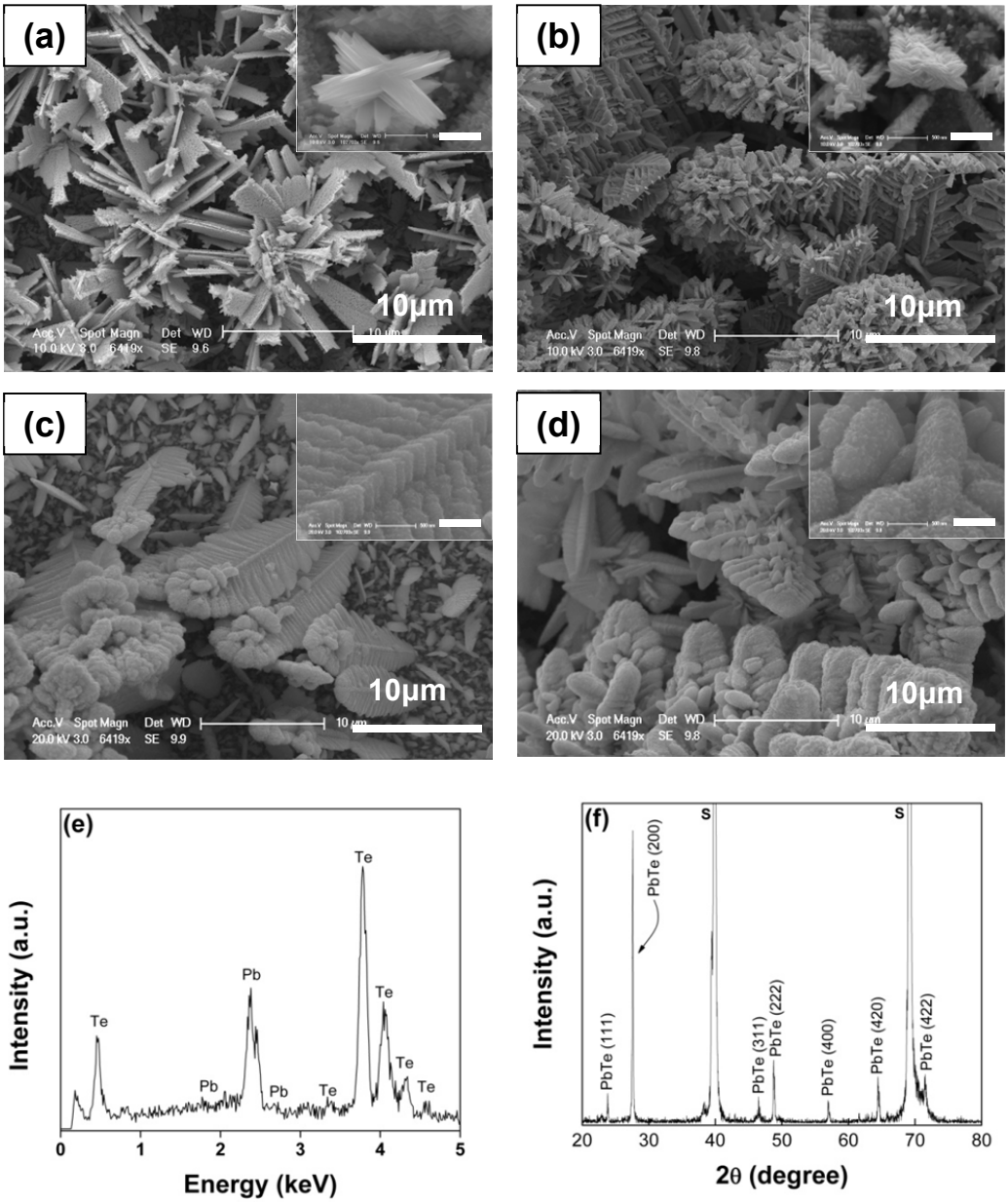

Figure 6.2. SEM images of the Pb_xTe_y thin films synthesized by galvanic displacement with Co sacrificial thin films at different ratio of electrolyte: $[Pb^{2+}]/[HTeO_2^+]$ = (a) 5, (b) 10, (c) 20, and (d) 50, respectively. (e) EDS spectrum and (f) XRD pattern of near-stoichiometric $Pb_{48}Te_{52}$ thin films prepared at electrolyte ratio of $[Pb^{2+}]/[HTeO_2^+]$ = 20, as shown in Fig. 2(c). The displacement time was fixed for 60 min. Scale bar (inset) = 500nm. (S in Fig. 2(f): substrates – Pt and Si).

6.2 (c),(d)). These results imply that high concentrations of Pb^{2+} might be favorable for the anisotropic growth of Pb_xTe_y for galvanic displacement from sacrificial Co thin films. Figure 6.2 (e),(f) shows the EDS spectrum and XRD pattern of near-stoichiometric $Pb_{48}Te_{52}$ thin films synthesized by galvanic displacement with 3μm thick sacrificial Co thin films at an electrolyte ratio of $[Pb^{2+}]/[HTeO_2^+]$ = 20. According to the EDS spectrum, all of the peaks correspond to Pb and Te on the substrate, indicating that sacrificial metal Co with 3μm thick is completely displaced. Moreover, galvanically deposited $Pb_{48}Te_{52}$ thin film is face-centered cubic (FCC) pattern as demonstrated by the characterization of diffraction peak (111), (200), (311), (222), (400), (420), and (422). Among these diffraction peaks, the intensity of diffraction peak (200) is much larger than of other peaks, indicating that Pb_xTe_y nanostructures highly preferred for this direction, along with the [100] direction based on the standard (JCPDS, 38-1435).

6.4.2 Effect of Thickness of Sacrificial Thin Films

The thickness of electrodeposited Co thin films is another important factor for galvanic displacement reaction. In order to investigate the influence of the sacrificial Co thin film thickness on surface morphology of Pb_xTe_y thin films, thickness of the sacrificial Co layer was changed from 1 to 5 μm by adjusting the electrodeposition time. The electrolyte for galvanic displacement was fixed at 50 mM Pb^{2+} + 10 mM $HTeO_2^+$ + 1 M HNO_3. Figure 6.3 (a)-(c) shows that the more dense, compact and uniform Pb_xTe_y thin films were formed by galvanic displacement with decreasing thickness of the sacrificial Co layer. Galvanically deposited Pb_xTe_y from 1 μm thickness of sacrificial Co thin films

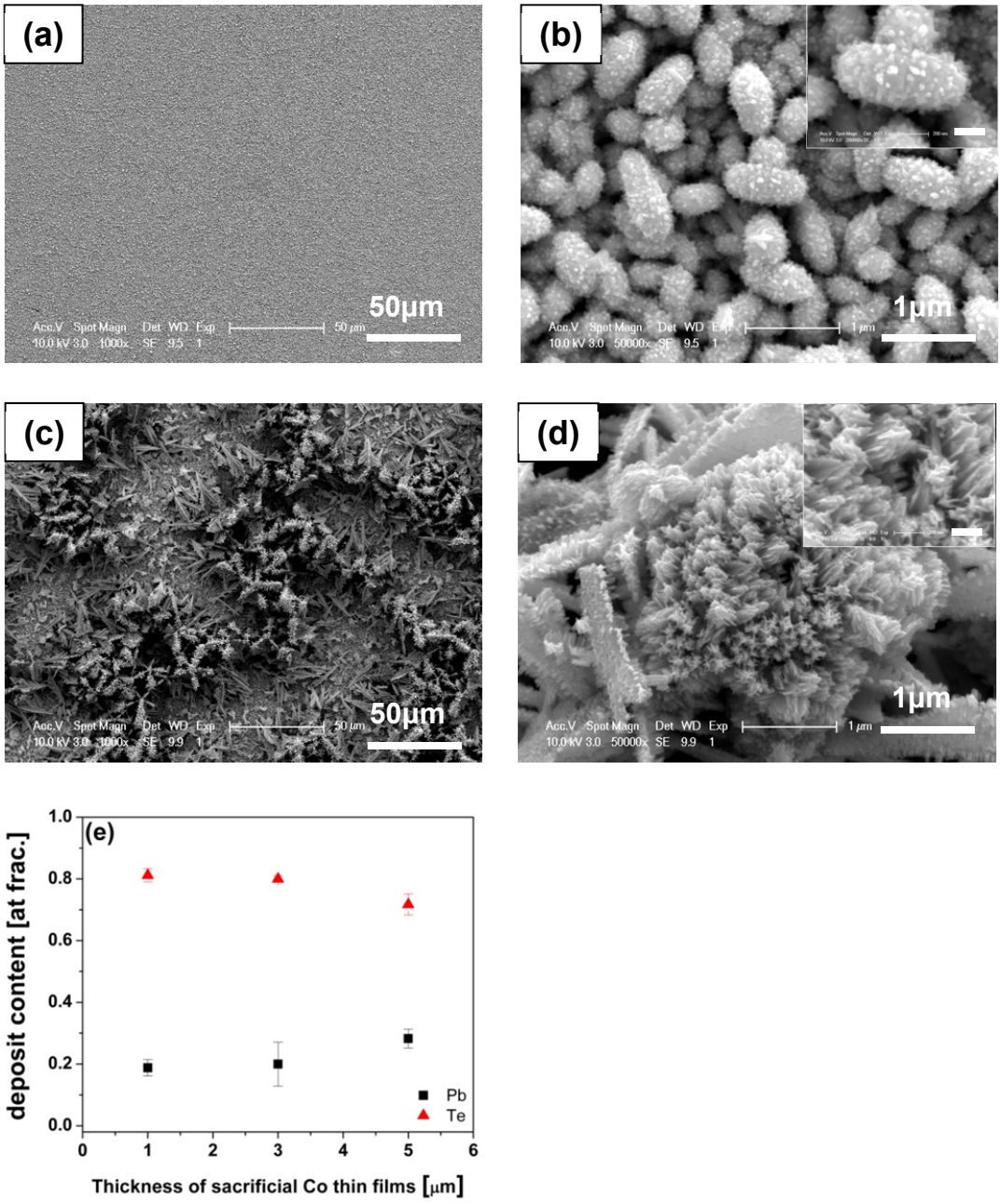

Figure 6.3. Surface morphology of the Pb_xTe_y thin films synthesized by galvanic displacement with different thickness of Co sacrificial thin films: (a-b) 1 and (c-d) 5µm. (e) Deposited content in the galvanically prepared Pb_xTe_y thin films as a function of thickness of sacrificial Co thin films. The electrolyte consisted of 50 mM Pb^{2+} + 10 mM $HTeO_2^+$ + 1 M HNO_3. Scale bar (inset) = 200nm.

consisted of a cucumber-like nanostructure with a uniform length of ~1 μm (Figure 6.3(b)), whereas synthesized Pb_xTe_y by galvanic displacement from 5 μm thickness of sacrificial Co thin films exhibited flower-like morphology with tapering features and stacked x-shaped plates around the flower-like structures (Figure 6.3(d)). On the other hand, the Pb_xTe_y nanostructures synthesized from 3 μm thickness of sacrificial Co thin films showed x-shaped nanostructures, which are shown in Figure 6.2(a). Therefore, the increase of the sacrificial Co thin film thickness will significantly influence the morphology of Pb_xTe_y nanostructures during galvanic displacement, where morphology changes from cucumber (1 μm), x shape (3 μm) to small flowerlike structures (5 μm). However, the film composition of Pb_xTe_y remained almost constant around 22 at.% Pb and 78 at.% Te as shown in Figure 6.3(e), which means the composition of Pb_xTe_y thin films was independent of the sacrificial Co thin films thickness.

6.4.3 Effect of Reaction Time

To investigate the effect of reaction time on galvanic displacement, the experiment was carried out with 3 μm thickness of sacrificial Co thin films at 50 mM Pb^{2+} + 10 mM $HTeO_2^+$ + 1 M HNO_3 for 3, 15, and 60 min. The sacrificial Co and galvanically deposited Pb and Te content were measured as a function of reaction time by energy dispersive X-ray spectroscopy (EDS). As shown in Figure 6.4(a), galvanic displacement proceeded quickly at early reaction stage (~15min) by dissolving sacrificial Co thin films with 1 M HNO_3 in the electrolyte. As the sacrificial Co content approached zero within 15 min, very fast nucleation of Pb_xTe_y occurred simultaneously, resulting in a sharp increase of

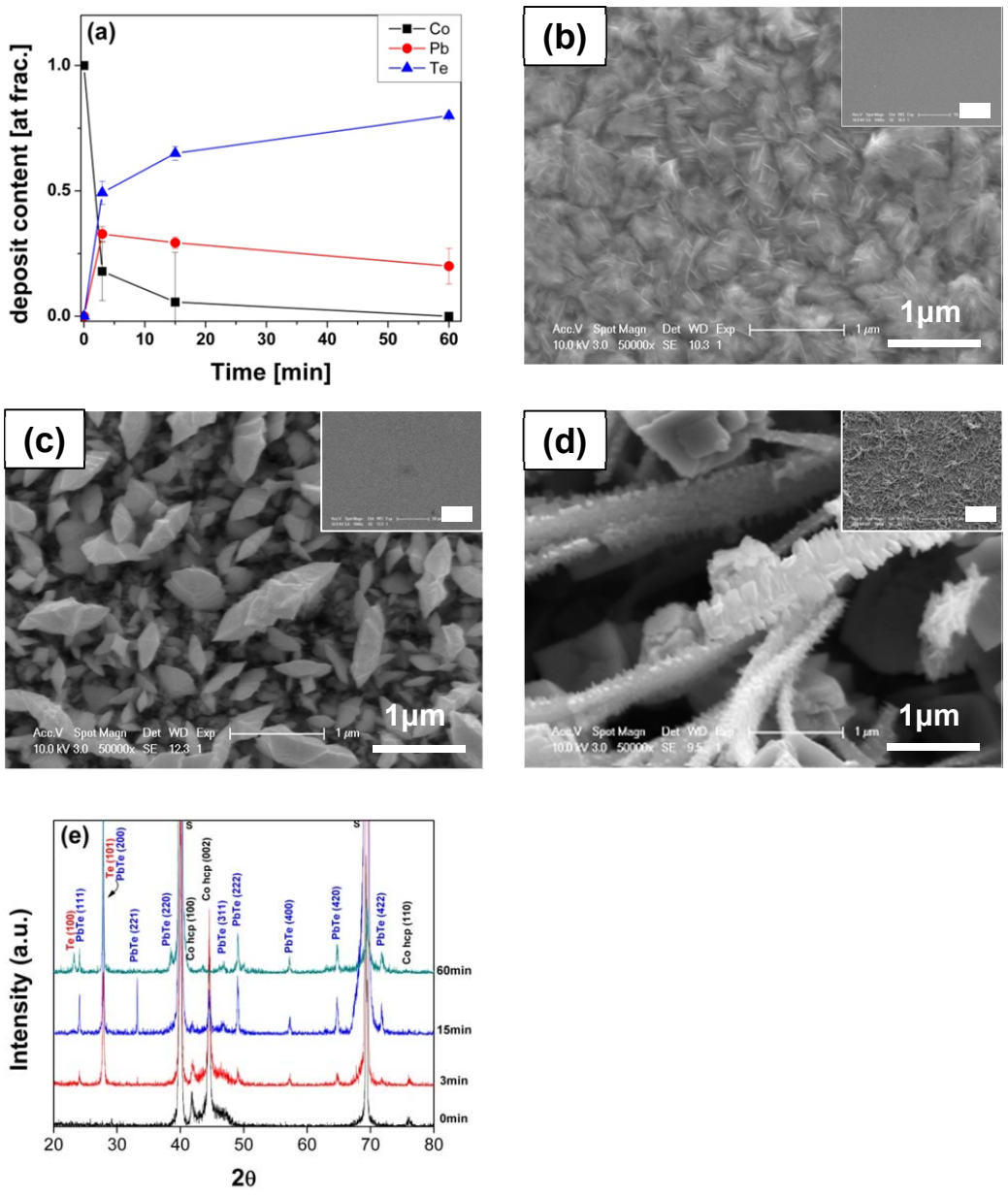

Figure 6.4. The content of sacrificial cobalt thin films, and as-deposited lead and tellurium on Pb_xTe_y thin films as a function of galvanic displacement time. Surface morphology of the galvanically deposited Pb_xTe_y prepared by reacting for (b) 0, (c) 3, and (d) 15min, respectively. And (e) XRD patterns with varying displacement time from 0 to 60 min. The ratio of $[Pb^{2+}]/[HTeO_2^{+}]$ in the electrolyte was fixed at 5. Scale bar (inset) = 50μm. (S: substrates – Pt and Si)

the galvanically deposited Pb and Te content in this stage. Afterwards, the deposited Te content was further increased up to 80 at.%, while deposited Pb content (20 at.%) decreased relatively in Pb_xTe_y thin films. It could be caused by the faster deposition rate of Te(s) (eq 2) compared to UPD of Pb^{2+} to form Pb_xTe_y compound (eq 3) during galvanic displacement.

The corresponding time-dependent morphology of galvanically deposited Pb_xTe_y thin films on sacrificial Co thin films is also shown in Figure 6.4(b),(c) and e. The electrodeposited Co thin films with around 3 μm thickness exhibited a granular structure with small and narrow needle-like structures (Figure 6.4(b)). As galvanic displacement started (~3 min), the Pb_xTe_y nuclei formed on the surface of sacrificial Co thin films, and gradually grew upward to form rhomboid structure of ~1 μm in size (Figure 6.4(c)). After the fast nucleation process, rhomboid structures grew in the longitudinal direction with x-shaped nanosheet of Pb_xTe_y as shown in Figure 6.4(d), whereas the stacked nanosheets continued to growth and eventually fully developed the x-shaped nanosheet architectures with up to a few μm thicknesses upon further increasing reaction time from 15 to 60 min (Figure 6.2(a)). These observations clearly indicate that the surface morphologies of Pb_xTe_y thin films significantly depend on galvanic displacement reaction time. The corresponding XRD patterns of each reaction time were obtained as shown in Figure 6.4(e). The electrodeposited sacrificial Co thin films (0 min) represent the typical hcp (hexagonal close packed) structures according to standard JCPDS 05-0727. All the diffraction peaks of sacrificial Co thin films gradually decrease as galvanic displacement reaction goes on until they almost disappear at around 15 min, indicating that most of the

sacrificial Co thin films are displaced with metal ions (Pb^{2+} and $HTeO_2^+$) in the electrolyte. It is consistent with the EDS analysis as shown in Figure 6.4(a). Galvanically deposited Pb_xTe_y thin films shows a FCC structure along with (111), (200), (221), (220), (311), (222), (400), (420), and (422) planes (JCPDS 38-1435). Although the peak intensity of Pb_xTe_y changes depending on the galvanic displacement time, there is no difference in the XRD patterns. Meanwhile, the tellurium peak along with (100) plane (JCPDS 36-1452) is observed at 60 min. This observation might be attributed to the relatively higher deposited Te content (80 at.%) compared to deposited Pb content (20 at.%).

Figure 6.5(a) shows the TEM image with selected area electron diffraction (SAED) pattern of galvanically deposited Pb_xTe_y nanostructures with sacrificial Co thin films at 50 mM Pb^{2+} + 10 mM $HTeO_2^+$ + 1 M HNO_3 for 60 min. The TEM image represents the stacked nanostructures of Pb_xTe_y, which is also in agreement with the SEM image shown in the Figure 6.5(a) inset. The SAED pattern reveals that a stacked Pb_xTe_y with x-shaped nanosheet consists of single crystalline FCC structure with a lattice parameter of a = 6.459 Å. The growth directions of Pb_xTe_y nanostructures are [100] and [110] (indicated by the arrow) as determined by SAED and high-resolution TEM (HRTEM). As shown in Figure 6.5(b), HRTEM image indicates a perfect order of crystalline lattice with spacing of 3.2 and 2.3 Å corresponding to the (100) and (110) planes, respectively. On the basis of TEM analysis, the proposed growth direction for x-shaped Pb_xTe_y nanostructures is [100], and the x-shaped nanosheet is [110].

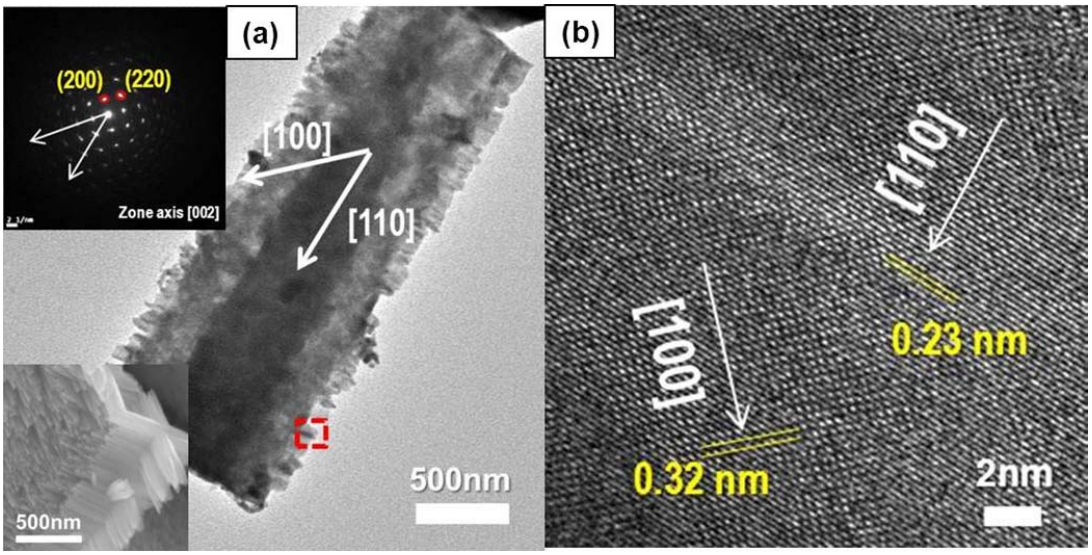

Figure 6.5. (a) TEM image (with an inset of SAED patterns and SEM image) of Pb_xTe_y nanostructures synthesized by galvanic displacement reaction. (b) HRTEM image of the Pb_xTe_y nanostructures (observed in red box as shown in Figure 5a)

6.5 Conclusions

In summary, we have demonstrated a simple approach to the synthesis of novel Pb_xTe_y nanostructures by galvanic displacement reaction between sacrificial Co thin films and metal ions (Pb^{2+} and $HTeO_2^+$) in the electrolyte. By varying the ratio of $[Pb^{2+}]/[HTeO_2^+]$ in the electrolyte, the film composition of Pb_xTe_y can be easily tuned from Te-rich ($Pb_{20}Te_{80}$) to Pb-rich ($Pb_{69}Te_{31}$). Furthermore, surface morphology of Pb_xTe_y varied from x-shaped, cucumber-like, flower-like to dendrite structures according to their composition and thickness of sacrificial thin films. We also demonstrated that growth of x-shape Pb_xTe_y nanostructures were dependent on reaction time of galvanic displacement. With obvious advantages, galvanic displacement is a facile method toward the synthesis of Pb_xTe_y nanostructures with controlled composition and morphology, thus allowing for further synthesis of lead chalcogenide materials.

6.6 References

[1] Zogg, H.; Kellermann, K.; Alchalabi, K.; Zimin, D., Optically pumped lead-chalcogenide mid-infrared emitters on silicon substrates. Infrared Phys Techn 2004, 46, (1-2), 155-159.

[2] Fardy, M.; Hochbaum, A. I.; Goldberger, J.; Zhang, M. M.; Yang, P., Synthesis and Thermoelectrical Characterization of Lead Chalcogenide Nanowires. Adv. Mater. 2007, 19, (19), 3047-3051.

[3] Shchennikov, V. V.; Ovsyannikov, S. V., Thermoelectric power, magnetoresistance of lead chalcogenides in the region of phase transitions under pressure. Solid State Commun. 2003, 126, (7), 373-378.

[4]Sergey, V. O.; et al., Application of the high-pressure thermoelectric technique for characterization of semiconductor microsamples: PbX-based compounds. J. Phys. D: Appl. Phys. 2004, 37, (8), 1151.

[5] Dughaish, Z. H., Lead telluride as a thermoelectric material for thermoelectric power generation. Physica B 2002, 322, (1-2), 205-223.

[6] Rowe, D. M., CRC Handbook of Thermoelectrics. 1st edn. ed.; CRC Press: 1995.

[7] Heremans, J. P.; Thrush, C. M.; Morelli, D. T., Thermopower enhancement in lead telluride nanostructures. Phys. Rev. B 2004, 70, (11), 115334.

[8] Maissen, C.; Masek, J.; Zogg, H.; Blunier, S., Photovoltaic infrared sensors in heteroepitaxial PbTe on Si. Appl. Phys. Lett. 1988, 53, (17), 1608-1610.

[9] Feit, Z.; McDonald, M.; Woods, R. J.; Archambault, V.; Mak, P., Low threshold PbEuSeTe/PbTe separate confinement buried heterostructure diode lasers. Appl. Phys. Lett. 1996, 68, (6), 738-740.

[10] Rodriguez, E.; Kellermann, G.; Craievich, A. F.; Jimenez, E.; C?ar, C. L.; Barbosa, L. C., All-optical switching device for infrared based on PbTe quantum dots. Superlattices Microstruct. 43, (5-6), 626-634.

[11] Harman, T. C.; Taylor, P. J.; Walsh, M. P.; LaForge, B. E., Quantum Dot Superlattice Thermoelectric Materials and Devices. Science 2002, 297, (5590), 2229-2232.

[12] Urban, J. J.; Talapin, D. V.; Shevchenko, E. V.; Murray, C. B., Self-Assembly of PbTe Quantum Dots into Nanocrystal Superlattices and Glassy Films. J. Am. Chem. Soc. 2006, 128, (10), 3248-3255.

[13] Qiu, X.; Lou, Y.; Samia, A. C. S.; Devadoss, A.; Burgess, J. D.; Dayal, S.; Burda, C., PbTe Nanorods by Sonoelectrochemistry. Angew. Chem. Int. Ed. 2005, 44, (36), 5855-5857.

[14] Wang, C.; Zhang, G.; Fan, S.; Li, Y., Hydrothermal synthesis of PbSe, PbTe semiconductor nanocrystals. J. Phys. Chem. Solids 2001, 62, (11), 1957-1960.

[15] Yang, Y.; Kung, S. C.; Taggart, D. K.; Xiang, C.; Yang, F.; Brown, M. A.; ell, A. G. G.; Kruse, T. J.; Hemminger, J. C.; Penner, R. M., Synthesis of PbTe Nanowire Arrays using Lithographically Patterned Nanowire Electrodeposition. Nano Lett. 2008, 8, (8), 2447-2451.

[16] Tong, H.; Zhu, Y.-J.; Yang, L.-X.; Li, L.; Zhang, L., Lead Chalcogenide Nanotubes Synthesized by Biomolecule-Assisted Self-Assembly of Nanocrystals at Room Temperature. Angew. Chem. Int. Ed. 2006, 45, (46), 7739-7742.

[17] Zou, G.; Liu, Z.; Wang, D.; Jiang, C.; Qian, Y., Selected-Control Solvothermal Synthesis of Nanoscale Hollow Spheres and Single-Crystal Tubes of PbTe. Eur. J. Inorg. Chem. 2004, 2004, (22), 4521-4524.

[18] Xiao, F.; Yoo, B.; Lee, K. H.; Myung, N. V., Synthesis of Bi2Te3 Nanotubes by Galvanic Displacement. J. Am. Chem. Soc. 2007, 129, (33), 10068-10069.

[19] Chang, C. H.; Rheem, Y.; Choa, Y.-H.; Shin, D. H.; Park, D.-Y.; Myung, N. V., Bi and Te thin films synthesized by galvanic displacement from acidic nitric baths. Electrochim. Acta 2010, 55, (3), 743-752.

[20] Jung, H.; Rheem, Y.; Chartuprayoon, N.; Lim, J.-H.; Lee, K.-H.; Yoo, B.; Lee, K.-J.; Choa, Y.-H.; Wei, P.; Shi, J.; Myung, N. V., Ultra-long bismuth telluride nanoribbons synthesis by lithographically patterned galvanic displacement. J. Mater. Chem. 2010, 20, (44), 9982-9987.

[21] Chang, C. H.; Rheem, Y.; Choa, Y.-H.; Park, D.-Y.; Myung, N. V., Galvanic displacement of BixTey thin films from sacrificial iron group thin films. Electrochim. Acta 2010, 55, (3), 1072-1080.

[22] Xiao, F.; Yoo, B.; Ryan, M. A.; Lee, K.-H.; Myung, N. V., Electrodeposition of PbTe thin films from acidic nitrate baths. Electrochim. Acta 2006, 52, (3), 1101-1107.

[23] Lide, D. R., CRC Handbook of Chemistry and Physics. 90th ed.; CRC Press: Cleveland, 2009.

[24] Xiao, F.; Yoo, B.; Bozhilov, K. N.; Lee, K. H.; Myung, N. V., Electrodeposition of Single-Crystal Cubes of Lead Telluride on Polycrystalline Gold Substrate. J. Phys. Chem. C 2007, 111, (30), 11397-11402.

[25] Revie, R. W., Uhlig's Corrosion Handbook. 2nd ed.; Wiley-Interscience: 2000.

Part 2

Electrochemical Synthesis and Characterization of Chalcogenide Nanostructures: PV materials

Chapter 7

Electrochemical Synthesis of CdTe NPs/SWNT Hybrid Nanostructures

7.1 Abstract

We report on an electrodeposition technique for functionalizing single-walled carbon nanotubes (SWNTs) with CdTe nanoparticles (NPs) with well-controlled size, surface morphology and composition of their nanostructures. Based on a systematic investigation of synthetic parameters, the CdTe NPs/SWNT hybrid nanostructures were modulated from the small and nodular structure to the core/shell nanostructures with increases up to 4-fold in their average height, and their compositions were easily tuned from Te-rich ($Cd_{29}Te_{71}$) to Cd-rich ($Cd_{79}Te_{21}$). The electrical and optoelectrical properties of hybrid nanostructures were also tuned through varying the size, surface morphology and composition of CdTe NPs, which corresponded to electrodeposition potential and charge density. Among these conditions, the maximum photosensitivity of hybrid nanostructures of up to 30% was obtained from complete coatings on SWNTs composed of Cd-rich CdTe (n-type). This work presents a new approach to manufacturing functionalized SWNTs with cadmium chalcogenide semiconductor (*e.g.* CdTe) NPs for tuning their electrical and optoelectrical properties, which can be achieved by modulating their material properties.

7.2 Introduction

Single-wall carbon nanotubes (SWNTs) have been widely used for optical, electronic, and biological devices due to their outstanding physical, chemical, and electrical properties [1-2]. Recently, SWNTs/semiconductor hybrid structures have also attracted growing interest for their applications in developing new materials for electronic and optoelectronic applications, such as nano-sensors, solar cells, photodetection devices, and photocatalyses because hybrid materials may enhance the electronic and optical properties correspoding to functional semiconducting materials [3-6]. Several approaches have been adopted to synthesize such hybrid nanomaterials, and these can be categorized into two strategies. One approach is to connect the pre-synthesized nanoparticles (NPs) to functionalized SWNTs through either covalent (e.g. with organic linker) or non-covalent bonds [7-11]. This approach offers advantages of not only well-controlled shape and size of individual NPs but also well-defined coverage between SWNTs and NPs. However, the chemical funtionalization may require more complicated experimental procedures (two-step process) and change the favorable properties of SWNTs or NPs due to the presence of organic linkers between them. The other approach is to directly deposit NPs onto the SWNTs surfaces via either electrodeposition or reduction reaction [12-15]. Direct deposition technique can be used to decorate all types of materials, including metals, semiconductors, and conducting polymers onto the SWNT networks and control the electrical properties of semiconductors (e.g. the conductivity type or bandgap engineering [12,15-19]. Furthermore, the electrochemical deposition technique can be easily utilized to control the size, number, surface morphology, and composition of NPs by adjusting deposition conditions, such as applied charge density and potential.

Moreover, this approach can enhance the electrical and physical properties of NP materials while preserving the intrinsic properties of SWNTs.

In this chapter, we demonstrate a simple, efficienct, controllable, and direct electrochemically assisted approach for decorating SWNTs with cadmium telluride (CdTe) NPs. CdTe semiconductor was selected as a functional material due to its energy band gap (1.44eV), which is very well matched with the solar spectrum [20]. CdTe NPs/SWNT hybrid nanostructures are directly synthesized using electrodeposition methods which control their size, surface morphology, and composition by adjusting various electrodeposition parameters. Analysis of the electrical and optoelectrical properties of the CdTe NPs/SWNT hybrid nanostructures showed photo-induced current, which could be tuned by tailoring the conductivity type (n-type or p-type) and morphology of hybrid nanostructures, achieved by altering the composition (Cd-rich or Te-rich) and size of CdTe NPs.

7.3 Experimental Section

Microfabricated gold electrodes were prepared on highly doped p-type Si substrate. Once a thickness of 100 nm SiO_2 was deposited on Si substrate by thermal CVD, Cr/Au (20/180 nm) electrodes were formed using standard lift-off techniques. The gaps of the gold electrodes were fixed at 3 μm. Suspended SWNTs in *N,N*-dimethylformamide (DMF) solution were prepared by first ultrasonically dispersing 0.1 μg/ml of carboxylated SWNTs (SWNTs-COOH 80 ~ 90% purity from Carbon Solution, Inc. (Riverside, CA, USA)), and further by centrifugation at 31,000 G for 90 min to remove

the non-soluble fraction and aggregates [18]. 0.2 μl of the SWNTs suspension of was dropped on top of gold electrodes bdtween 3 μm gap, and a AC dielectrophoretic field was applied at 3 V peak to peak with 4 MHz frequency for the alignment of SWNTs. The resistance of the aligned SWNTs (initial resistance, R_0) was adjusted by varying the deposition time. The R_0 of bare SWNTs was controlled in the range of 1 – 4 kΩ. After assembly, the devices were rinsed with deionized water, and dried by gentle blowing of nitrogen gas. The samples were annealed at 300 °C for 1 hr in 5% H_2 in reduction environment (i.e. 5% H_2 in N_2) to reduce the contact resistance between the gold electrodes and SWNTs and to remove possible DMF residues.

Prior to electrochemical functionalization of SWNTs with CdTe NPs, linear sweep voltammetry (LSV) was performed with fixed scan rate (-5mV/sec) to investigate the electrochemical reaction at room temperature with a three-electrode configuration. The aligned SWNTs between gold electrodes, platinum wire, and chlorinated sliver wire were employed as working, counter, and reference electrodes, respectively. For ease of comparison, the potential of the pseudo reference electrode (chlorinated sliver wire) was converted to the potential of Ag/AgCl (sat. KCl). The functionalization of SWNTs was conducted by electrodeposition with electrolyte containing 1 M $CdSO_4$ and 0.15 mM TeO_2 in 1 M H_2SO_4. The pH of the electrolyte was maintained at 2.0 by adding NaOH and/or H_2SO_4. Once 3 μl of the electrolyte was placed on top of the aligned SWNTs, the pre-determined potential was applied with varying charge density. Potentials ranging between −0.15, −0.5 and −0.65 V vs. Ag/AgCl were applied to investigate the changes in compositions of CdTe NPs/SWNT hybrid nanostructures. Furthermore, the effects of

charge density on the size and surface morphology of hybrid nanostructures were examined by varying the deposition charge density from 5 up to 2000 mC/cm^2.

The surface morphology and composition of CdTe NPs/SWNT hybrid nanostructures were examined by scanning electron microscope (SEM, XL30-FEG, Phillips) with energy-dispersive spectroscopy (EDS, EDAX, Phoenix). The analysis of topography and average height distribution of SWNT networks before and after the functionalization were performed using an atomic force microscope (AFM, Veeco's Innova). An X-ray diffractometer (XRD, D8 Advance Diffractometer, Bruker) with Cu Kα radiation (operating at 40 kV) was used for phase identification of functionalized SWNTs with CdTe NPs.

Both the electrical and optoelectrical properties of CdTe NPs/SWNT hybrid nanostructures were measured using a dual source measure unit (model 2636A, Keithley) in ambient conditions at room temperature. For FET transfer characteristics, the highly doped Si substrate was used as a back gate, and the gate bias (V_G) was set as a sweep from −20 to 20 V with a constant source-drain voltage (V_{DS}) of +0.5 V. The mercury UV excitation lamp, with three main peaks at 365, 405, and 436 nm with power of 146, 180, and 290 mW/cm^2, respectively, was used to excite the carriers in the CdTe NPs.

7.4 Results and Discussion

7.4.1 Effects of Electrodeposition Parameters on CdTe NPs/SWNT Hybrid Nanostructures

Figure 7.1(a) and (b) illustrate the synthesis processes of CdTe NPs/SWNT hybrid nanostructures on prefabricated silicon substrate with gold electrode (see Experimental Methods for details). Once the SWNT suspension was dropped onto the microelectrode, the AC dielectrophoretic field was applied to align the SWNTs between gold pads, as shown in Figure 7.1(a). After assembly, the CdTe NPs were directly deposited onto the surface of the aligned SWNTs using an electrochemical deposition method with an electrolyte containing 1 M $CdSO_4$ + 0.15 mM TeO_2 + 1 M H_2SO_4. As illustrated in Figure 7.1(b), SWNTs that were aligned between gold electrodes and were chlorinated Ag wire and Pt wire were used as a working, reference, and counter electrode, respectively.

In order to understand the effect of electrodeposition parameters (*e.g.* deposition potential and charge density) on surface morphology and size of CdTe NPs/SWNT hybrid nanostructures, systematic investigation was carried out by varying the deposition potential (−0.15, −0.5, −0.65 V vs. Ag/AgCl selected on the basis of linear sweep voltammogram) and applied charge density (from 5 to 2000 mC/cm^2), respectively. The formation and surface morphology of the bare SWNTs and CdTe NPs/SWNT hybrid nanostructures were examined using scanning electron microscopy (SEM) and atomic force microscopy (AFM), as shown in Figure 7.1 (see also Figure 7.2). Figure 7.1(c) reveals the perpendicularly aligned bare SWNTs to the gold electrode between 3 μm gap, resulting from the AC dielectrophoresis. The functionalization of CdTe NPs through electrodeposition and their firm adhesion to the surface of the aligned SWNTs can be seen in Figure 7.1(d)-(g). The SEM images show that the size and roughness of CdTe NPs/SWNT hybrid nanostructures are significantly influenced by applied charge density.

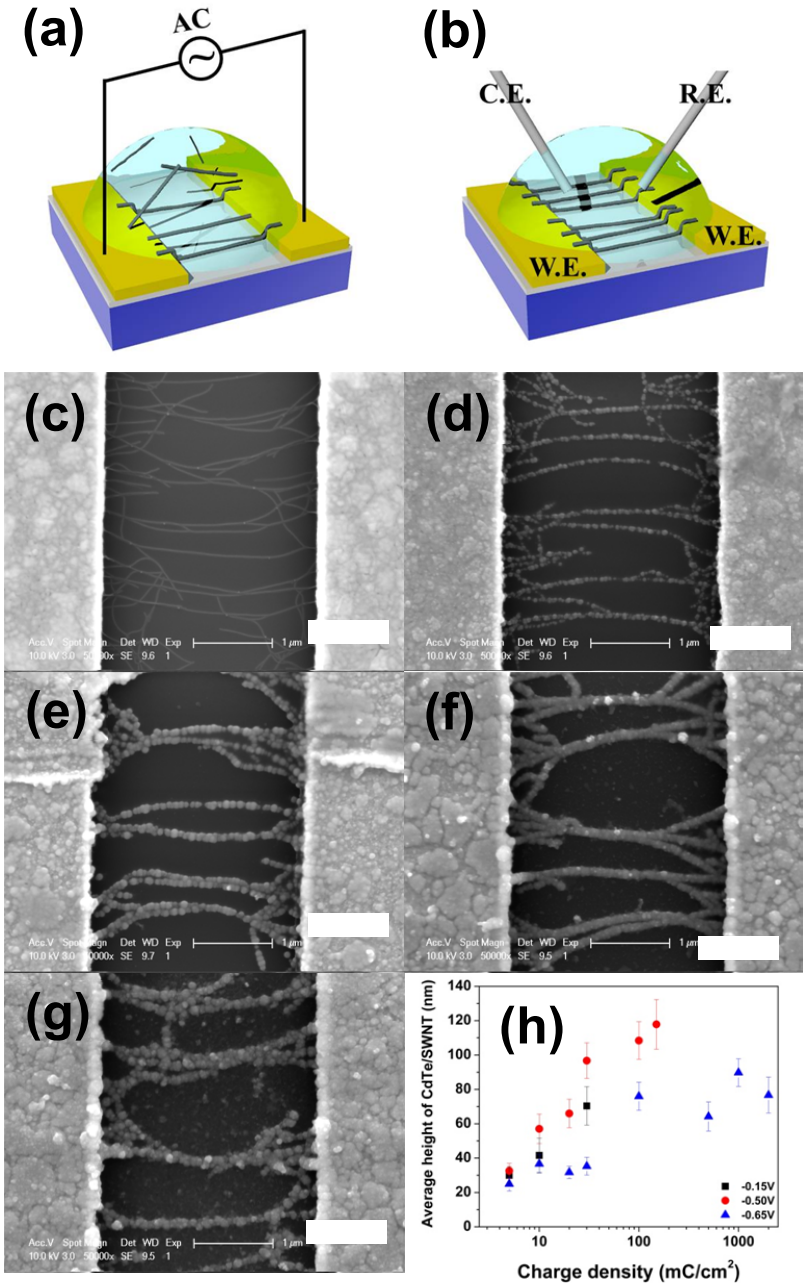

Figure 7.1. Schematic diagrams of electrochemical synthesis of CdTe NPs/SWNT hybrid nanostructures. (a) Dielectrophoretic alignment of SWNTs between 3μm gap of gold electrode. (b) Electrochemcial functionalization of CdTe NPs on aligned SWNTs. SEM images of functionalized SWNTs with CdTe NPs at −0.50 V vs. Ag/AgCl with varying the applied charge density at (c) 0, (d) 10, (e) 30, (f) 100, and (g) 150 mC/cm^2, respectively. (h) Average height of CdTe/SWNT hybrid nanostructures as a function of charge density. Scare bar = 1 μm.

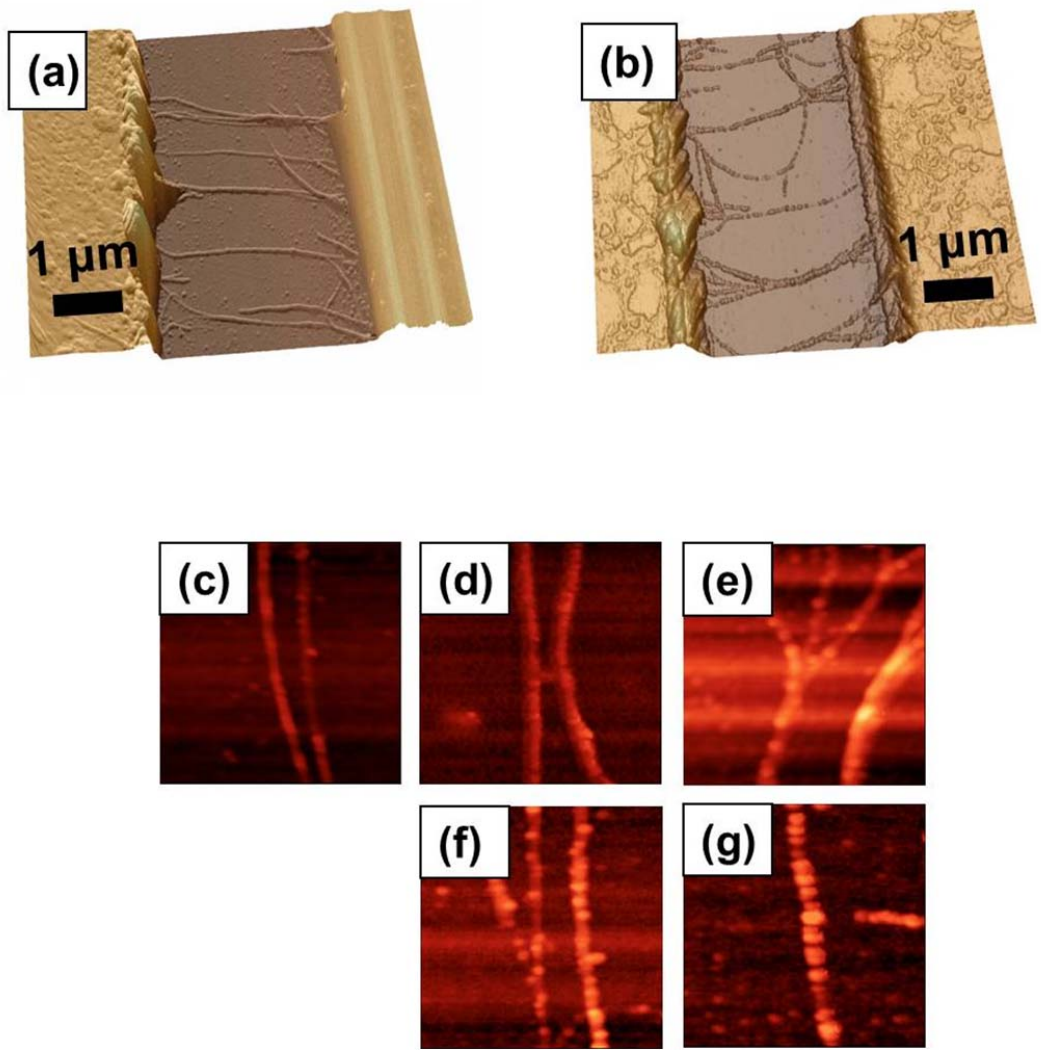

Figure 7.2. AFM images of (a) before and (b) after the functionalization of aligned SWNTs between gold electrode with CdTe NPs (30 mC/cm^2). A topography of (c) bare and (d-g) CdTe NPs/SWNT hybrid nanostructures. The CdTe NPs was electrodeposited at fixed −0.50 V vs. Ag/AgCl with charge density of (d) 5, (e) 10, (f) 20, and (g) 30 mC/cm^2, respectively.

At low applied charge density (Figure 7.1(d) and (e)), the small and nodular NPs were decorated on the SWNTs, whereas the larger and more extensive coverage of CdTe NPs were formed on aligned SWNTs at a relatively higher charge density. For instance, at charge densities of 100 and 150 mC/cm^2, the aligned SWNTs were almost completely covered with CdTe to form the core/shell nanostructures as shown in Figure 7.1(f) and (g). This may be due to continuous growth of CdTe NPs and cohesion with neighboring particles. The average height of CdTe/SWNT hybrid nanostructures was determined through SEM and AFM analysis. Figure 7.1(h) shows that the overall average height of hybrid nanostructures increased up to maximum of 4-times the original value with increasing charge density, implying that the size of CdTe/SWNT hybrid nanostructures are significantly affected by this condition. However, the average height of hybrid nanostructures at the high applied potential (-0.65 V vs. Ag/AgCl) is smaller than that at relatively low applied potential. This may be attributed to the reduced current efficiency of the system resulting from hydrogen gas evolution at higher potential regions [21,22]. The crystal structures of decorated SWNTs with CdTe NPs were analyzed by the XRD patterns. As shown in Figure 7.3, XRD spectra of as-decorated CdTe NPs on aligned SWNTs indicate a mixture of cubic and hexagonal structures with (111), (311) and (511) plane of cubic (JCPDS 15-0770), and (002), (006) plane of hexagonal structures (JCPDS 19-0193), respectively. Examination of the surface morphology and size of hybrid nanostructures clearly indicates their controllability by adjusting the electrodeposition parameters such as deposition potential and applied charge density.

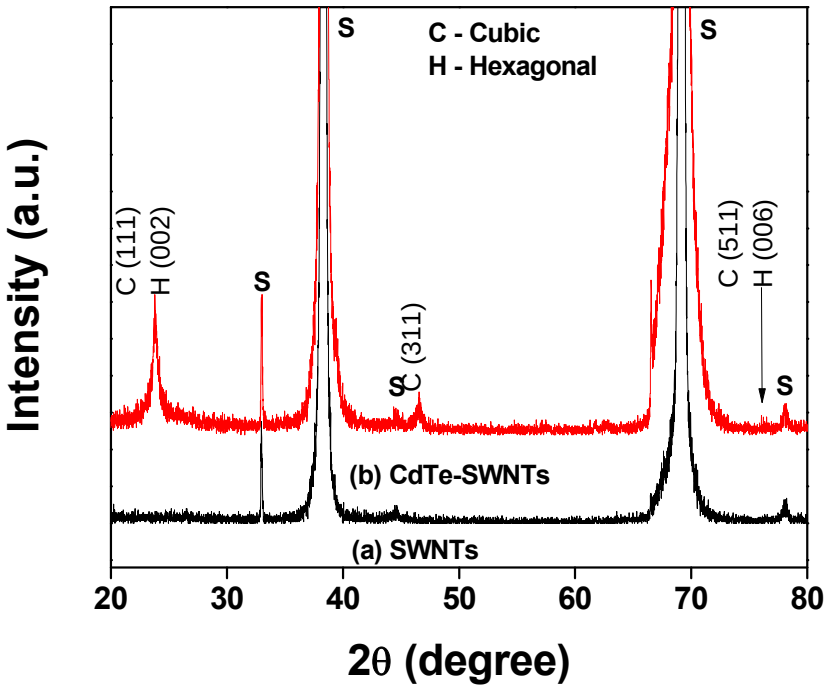

Figure 7.3. XRD pattern of bare and functionalized SWNTs with CdTe NPs. The CdTe NPs was electrodeposited at −0.50 V vs. Ag/AgCl with charge density of 2000 mC/cm^2. (S : substrate – carbon, gold, and silicon)

Linear sweep voltammogram (LSV) of the electrodepostion of CdTe NPs on SWNTs was carried out to investigate the electrochemical reaction and to determine the appropriate potential range. As shown in Figure 7.4(a), two distinguishable reduction waves appeared in the LSV curves as the potential was negatively swept from 0 to −0.70 V vs. Ag/AgCl. The first reduction wave started at around −0.15 V vs. Ag/AgCl corresponding to the over-potential deposition (OPD) of element Te(s) (eq 1), followed by the under-potential deposition (UPD) of Cd^{2+} onto deposited Te(s) (eq 2). The second reduction wave beyond −0.60 V vs. Ag/AgCl shows the OPD of element Cd(s) (eq 3).

The overall electrodeposition mechanism of CdTe NPs can be represented by following elementary steps [20,21]:

$$HTeO_2^+ + 3H^+ + 4e^- \rightarrow Te(s) + 2H_2O, \qquad E_0 = +0.55 \text{ V vs. NHE} \qquad (1)$$

$$Cd^{2+} + Te(s) + 2e^- \rightarrow CdTe(s), \qquad E_0 = +0.10 \text{ V vs. NHE} \qquad (2)$$

$$Cd^{2+} + 2e^- \rightarrow Cd(s), \qquad E_0 = -0.40 \text{ V vs. NHE} \qquad (3)$$

This analysis shows that the electrodeposition in the range of first reduction wave (between −0.15 and −0.60 V vs. Ag/AgCl) favors Te-rich CdTe deposition, while deposition below the −0.60 V vs Ag/AgCl (second reduction wave) favors Cd-rich CdTe deposition. In order to precisely control the composition of CdTe NPs on SWNT networks, potentiostatic electrodeposition was conducted by varying the deposition potential between −0.15 and −0.70 V vs. Ag/AgCl. Figure 7.4(b) shows the deposited Te content in CdTe NPs on aligned SWNT as a function of deposition potentials, illustrating a strong dependence of the composition of CdTe to potential as expected. Higher deposited Te content in the range of UPD of Cd^{2+} (between −0.15 and −0.60 V vs Ag/AgCl) was observed with 56 ~71 at.% (Te-rich). However, the Te content slightly decreased at the composition of 21 ~43 at.% Te (Cd-rich) in the range of OPD of Cd^{2+} (−0.65 ~ −0.7 V vs. Ag/AgCl), which is consistent with the previous LSV analysis. Therefore, the composition of CdTe NPs can be easily tuned from Te-rich ($Cd_{29}Te_{71}$) to Cd-rich ($Cd_{79}Te_{21}$) by simply varying the applied potential.

Overall, it can be concluded that this electrodeposition method allows one to precisely control the size, surface morphology and composition of the CdTe NPs/SWNT hybrid nanostructures by varying the deposition potential and the applied charge density.

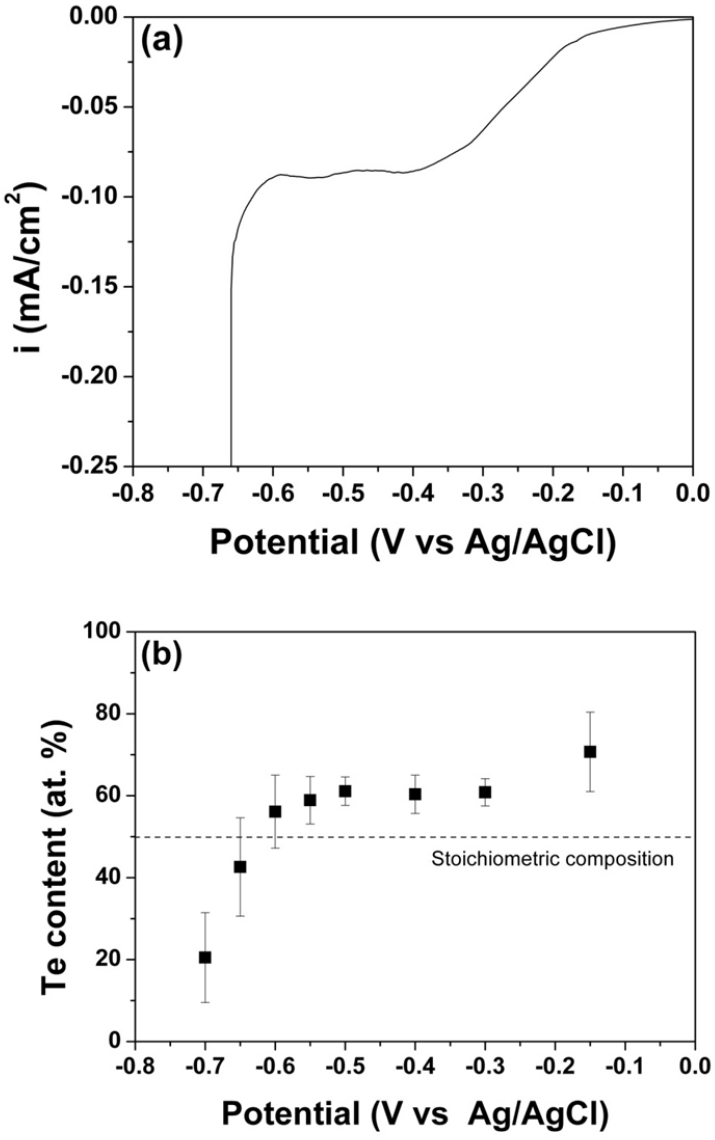

Figure 7.4. (a) Linear sweep voltammogram (LSV) of CdTe NPs electrodeposition in electrolyte containing 1 M $CdSO_4$ + 0.15 mM TeO_2 + 1 M H_2SO_4. (b) Dependence of deposited Te content on applied deposition potential.

7.4.2 Electrical Properties of CdTe NPs/SWNT Hybrid Nanostructures

Further investigation of electrical properties was done by adopting the deposition potential of −0.15 and −0.5, and −0.65 V vs. Ag/AgCl for the synthesis of p-type (Te-rich) and n-type (Cd-rich) CdTe NPs, respectively. Figure 7.5(a) shows the I-V characteristics of CdTe NPs/SWNT hybrid nanostructures with a slightly S-shaped I-V curve, indicating a typical Schottky contact which consists of a semiconductor (SWNTs) connection between two metal contacts (gold pads [23]. With increasing applied charge density from 5 to 150 mC/cm^2, the slope of the I-V curves shows a decrease, implying an increase in the resistance of hybrid nanostructures. Thus, the electrical properties of functionalized SWNTs with CdTe NPs show a strong dependence on electrodeposition parameters such as an applied charge density. For the FET transport measurement (Figure 7.5(b), inset), the gold electrodes were used as source and drain pads, while SiO_2 with a thickness of 100 nm were used as the back-gate dielectric, as reported in previous literature [24,25]. The gate voltage was swept from −20 to 20 V in steps of 0.5 V at fixed source-drain voltage (V_{DS}) of + 0.5 V. As shown in Figure 7.5(b), bare SWNTs produce a typical p-type semiconductor FET transport behavior, resulting from continuously decreasing channel current (I_{DS}) with increasing gate potential (V_G) [26]. After functionalization of SWNTs with CdTe NPs, the FET transport curves of hybrid nanostructures still show a p-type semiconductor behavior, even though the I_{on}/I_{off} ratio slightly decreases from 1.5 (bare SNWNs) to 1.1 (150 mC/cm2). This might be caused by poor uniformity of the CdTe NPs/SWNT hybrid nanostructures over entire surface as the applied charge density is increased [27].

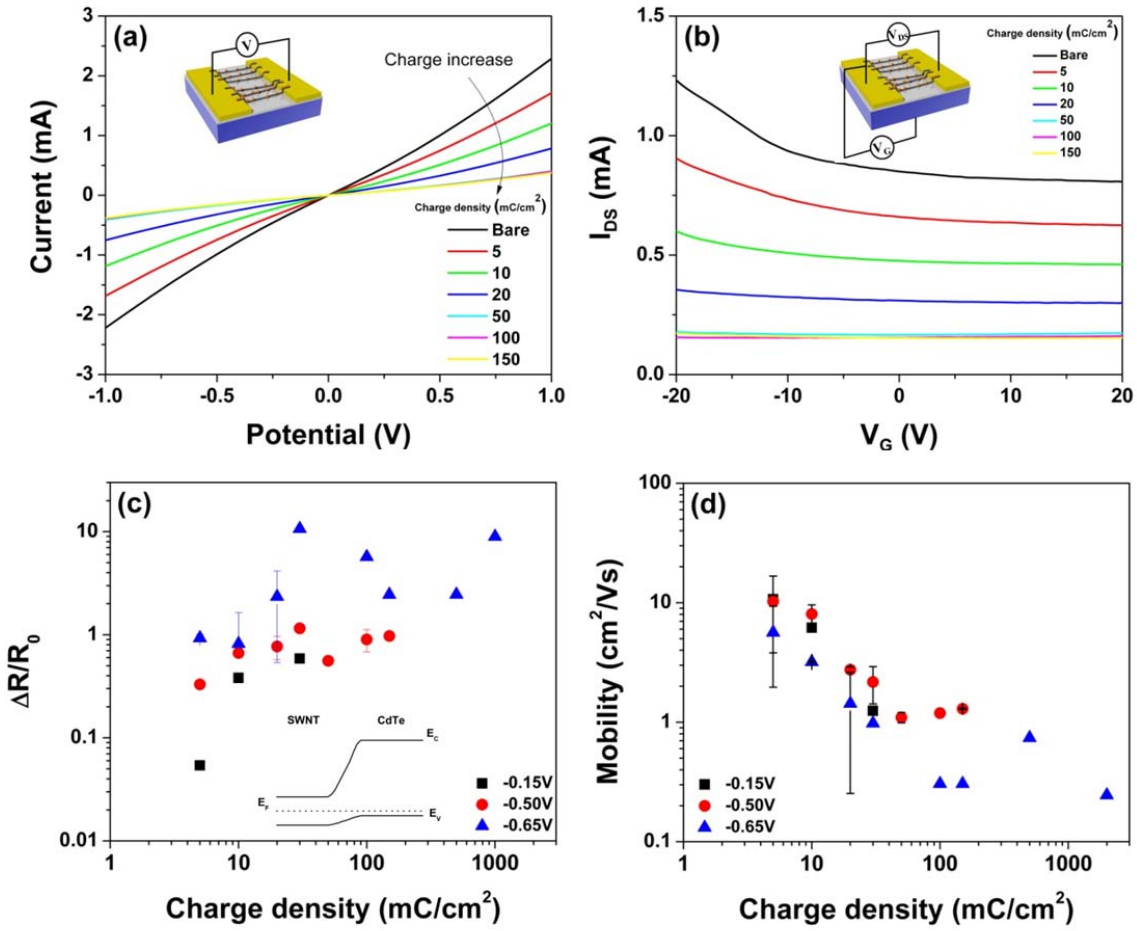

Figure 7.5. Electrical properties of CdTe NPs/SWNT hybrid nanostructures as function of applied charge density. Typical (a) I-V characteristics and (b) FET transport curves with a V_{DS} of + 0.5 V. The electrochemical functionalization with CdTe NPs was conducted at fixed −0.50 V vs. Ag/AgCl. (c) Electrical resistance change and (d) field-effect mobility as a function of applied charge. The initial resistance (R_0) of SWNTs before decoration was in the range of 1−4kΩ.

To understand the effect of electrodeposition parameters on electrical properties of hybrid nanostructures in greater detail, the resistance change ratio ($\Delta R/R_0$) and mobility was determined as shown in Figure 7.5(c) and (d). The initial resistance (R_0) of bare

SWNTs was controlled in the range of 1 – 4 kΩ. Overall, resistance of hybrid nanostructures increased over the entire range of electrodeposition parameters such as deposition potential and applied charge density. For the same deposition potential, $\Delta R/R_0$ of the CdTe NPs/SWNT hybrid nanostructures showed an increasing trend of up to a maximum of 10-fold in increase of applied charge density. The band structure after the formation of a junction between SWNTs and CdTe NPs (Figure 7.5(c) inset) may be the cause of this phenomenon. Electron affinity, work function, and bandgap of SWNT and CdTe were adopted from references [28-30]. Based on the band structure, electrons in CdTe NPs diffused into SWNTs because the conduction band of SWNTs is lower than that of CdTe NPs. As a result, the diffused electrons filled the holes in aligned SWNTs (hole transfer material), resulting in an increased resistance of the CdTe NPs/SWNT hybrid nanostructures. Furthermore, Figure 7.5(c) also illustrates that the $\Delta R/R_0$ in Cd-rich samples (−0.65 V vs. Ag/AgCl) was slightly higher than that in Te-rich samples (−0.15 and −0.5 V vs. Ag/AgCl) over the entire charge density range. The excess Te content appears to give a higher mobility and lower resistivity, resulting in lower resistance change ($\Delta R/R_0$) in Te-rich samples (−0.15 and −0.5 V vs. Ag/AgCl). These result are in good agreement with the results already reported [31]. The field-effect hole mobility was determined using following equation [24,26]:

$$\mu = \frac{dI_{DS}}{dV_G}\frac{L^2}{C_G V_{SD}} \tag{4}$$

where μ is the field effect mobility, dI_{DS}/dV_{G-} is the transconductance obtained from the linear region of the I_{DS}-V_G curves, L is the length of hybrid nanostructures, and C_G is the approximate capacitance, respectively. Figure 7.5(d) shows the FET mobility ranged from 0.2 to 10 cm^2/Vs as a function of applied charge density. Decreases of carrier mobility over the entire deposition potential range were observed with increase of applied charge density. Since the resistance of electrical conducting channel (CdTe NPs/SWNTs hybrid nanostructure) is higher at the higher charge density (Figure 7.5(c)), the high charge density samples were expected to have lower carrier mobility than lower charge density samples. This behavior might be due to CdTe NPs increasing the interface defects [32,33]. Thus, electrical characteristics, such as resistance change ($\Delta R/R_0$) and FET mobility (μ), can be tuned by varying electrodeposition potential and charge density.

7.4.3 Optoelectrical properties of CdTe NPs/SWNT hybrid nanostructures

Figure 7.6(a) shows the schematic illustration of optoelectrical measurement for CdTe NPs/SWNT hybrid nanostructures under UV irradiation. The mercury excitation lamp was used as the light source which has three main peaks at 365, 405, and 436 nm with power of 146, 180, and 290 mW/cm^2, respectively. Figures 7.6(b) and (c) show the typical I-V characteristics and FET transport properties for CdTe NPs/SWNT hybrid nanostructures in the dark and under UV illumination. The current under UV exposure showed a smaller increase compared to current in dark as shown in Figure 7.6(b) inset. This behavior results from the contribution of photo-excited holes in CdTe NPs, which are subsequently transferred to SWNTs, acting as the hole-carrier material in the

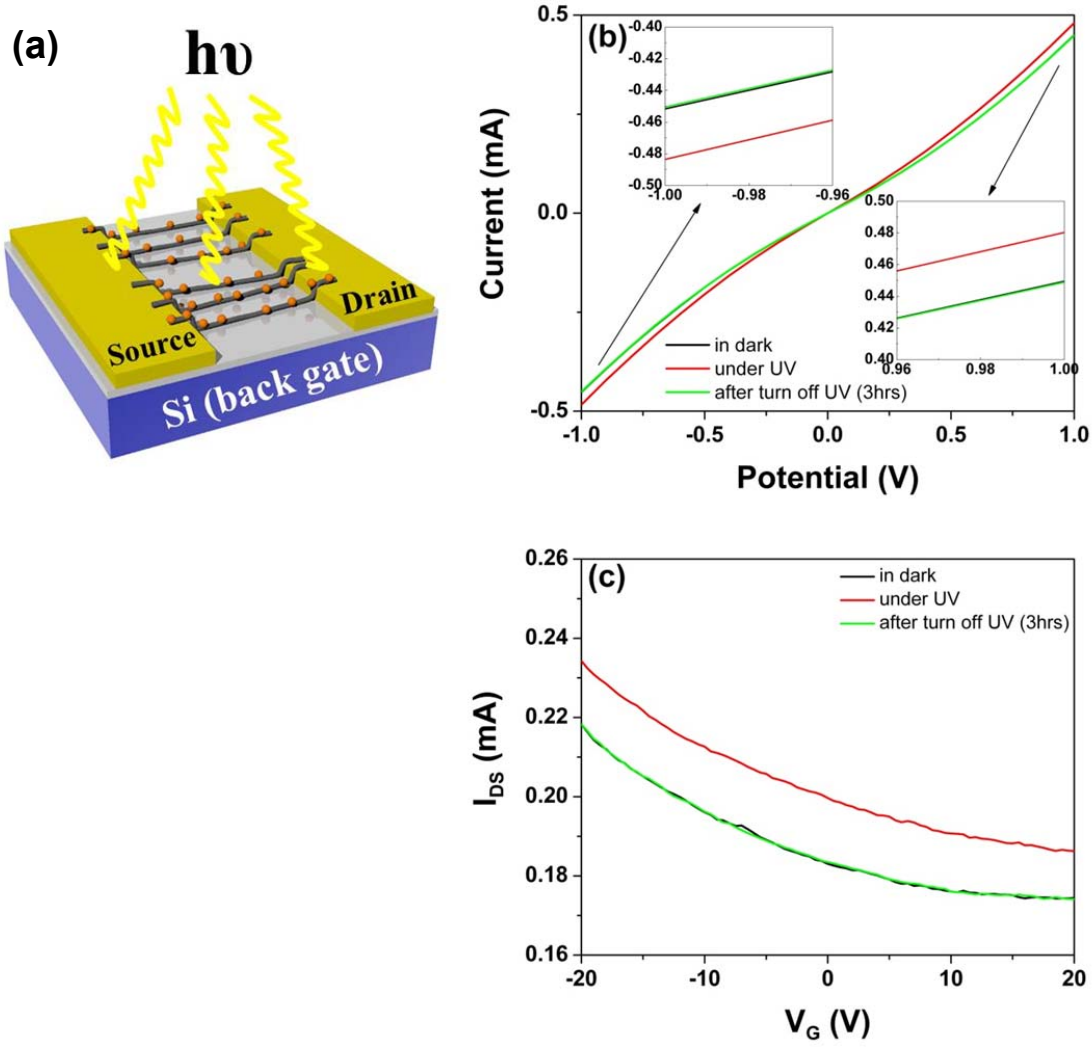

Figure 7.6. (a) Schematic diagrams of optoelectrical measurement under UV irradiation. Typical (b) I-V characteristics and (c) FET transport curves (V_{DS} = + 0.5 V) were measured in the dark, under UV light, after which the UV lights were turned off (3 hrs). The CdTe NPs were functionalized on top of SWNTs at fixed −0.50 V vs. Ag/AgCl with charge density of 150 mC/cm^2.

conduction pathway. Although the I-V curve did not recover to the original value when the device was measured right after the UV light was turned off, the values returned to the original measurement after 3 hours. This delayed response may be due to the very

slow speed with which the accumulated charges in the semiconductor are released. Similar to the I-V characteristics, FET transport properties also show increases in source-drain current (I_{DS}) after exposure of the CdTe NPs/SWNT hybrid nanostructures under UV illumination as shown in Figure 7.6(c). It is clearly shown that the threshold voltage (V_{th}) of transfer curves shifted toward positive voltages from 1 (in dark) to 4 V (under UV) without tilting. This photoinduced V_{th} shift may be attributed to increases in the hole carrier concentration in the CdTe NPs/SWNT hybrid nanostructures under UV irradiation [34].

Figure 7.8(a) shows a typical photocurrent change ($\Delta I/I_0$) as a function of time with varying UV light exposure. The induced current of CdTe NPs/SWNT hybrid nanostructures increased upon exposure to UV light, even though the $\Delta I/I_0$ of bare SWNTs decreased under UV irradiation (Figure 7.7), which is consistent with I-V characteristics in Figure 7.6 and reported results in the literature [11]. It was also observed that the photocurrent change is strongly dependent on applied charge density. The magnitude of photoresponse which increased with increasing charge density was equal to the applied charge density, indicating that the highest contribution to this effect was from the sample with the most amount of deposited CdTe on the SWNTs as shown in schematics. To further exploit optoelectrical properties of hybrid nanostructures, the photosensitivity was determined with three different deposition potential of −0.15, −0.5 (Te-rich) and −0.65 V (Cd-rich) vs. Ag/AgCl and charge density as shown in Figure 7.8(b). Thus, the dependency of photosensitivity on applied charge density and potential can be clearly seen. Higher charge density and deposition potential for the synthesis of

CdTe NPs/SWNT hybrid nanostructures produced a higher photoresponse than the lower charge density and potential. As explained before, as-synthesized hybrid nanostructures with higher applied charge density led to better sensitivity at fixed potential due to the amount of deposited CdTe on aligned SWNTs. On the other hand, the photoresponse of CdTe NPs/SWNT hybrid nanostructures was highest at −0.65V (Cd-rich, n-type) compared to −0.15, −0.5V vs. Ag/AgCl (Te-rich, p-type) over the entire charge density range, which means the p−n (SWNTs − Cd-rich CdTe) junction is better than the p–p (SWNTs − Te-rich CdTe) junction. Thus, it is remarkable that the optoelectrical properties of CdTe NPs/SWNT hybrid nanostructures can be tuned by tailoring of the electrodeposition parameters such as deposition potential and applied charge density.

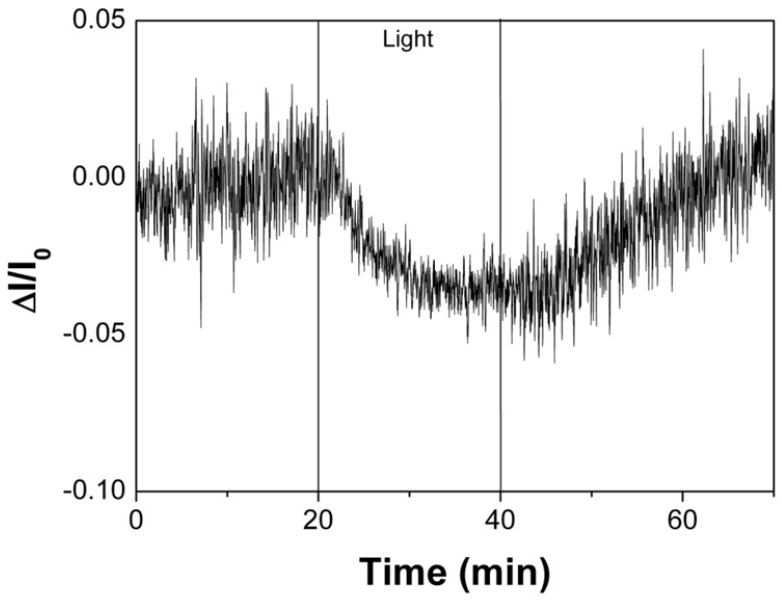

Figure 7.7. Current change of bare SWNTs as a function of time under UV irradiation.

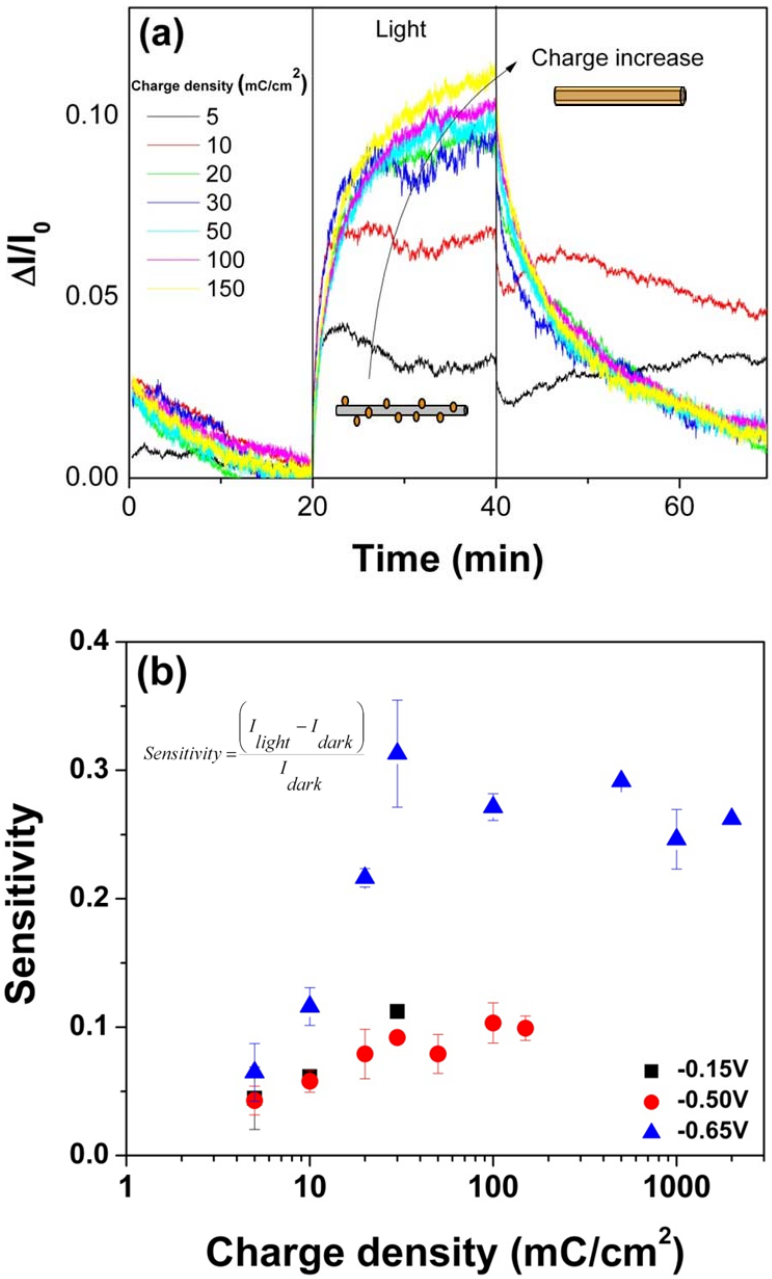

Figure 7.8. (a) Schematic diagrams of optoelectrical measurement under UV irradiation. Typical (b) I-V characteristics and (c) FET transport curves (V_{DS} = + 0.5 V) were measured in the dark, under UV light, after which the UV lights were turned off (3 hrs). The CdTe NPs were functionalized on top of SWNTs at fixed −0.50 V vs. Ag/AgCl with charge density of 150 mC/cm^2.

7.5 Conclusions

In summary, the functionalized SWNTs with CdTe NPs were synthesized with the capability to control their size, surface morphology, and composition by direct electrodeposition. Adjustment of the synthetic conditions such as deposition potential and applied charge density resulted in an increase in the size and surface morphology of hybrid nanostructures of up to 4 times, with structures varying from small and nodular structures to the core/shell nanostructures, respectively. Furthermore, their composition were able to be tuned from Te-rich ($Cd_{29}Te_{71}$) to Cd-rich ($Cd_{79}Te_{21}$) by simply varying the applied potential. Based on these systematic investigations, the electrical and optoelectrical properties were measured, which showed photo-induced current of the CdTe NPs/SWNT hybrid nanostructures under UV irradiation. The photosensitivity of hybrid nanostructures was dependent of their size and conductivity type (p-type or n-type), with enhanced sensitivity up to 30% through complete coatings to the SWNTs with Cd-rich CdTe (n-type). Given these obvious advantages, a facile electrodeposition method can be utilized to manufacture functionalized SWNTs with CdTe NPs with controlled their properties, thus allowing for further synthesis of cadmium chalcogenide materials such as cadmium sulfide (CdS) and cadmium selenide (CdSe).

7.6 References

[1] Dai, H., Carbon Nanotubes: Synthesis, Integration, and Properties. Acc. Chem. Res. 2002, 35, (12), 1035-1044.

[2] Baughman, R. H.; Zakhidov, A. A.; de Heer, W. A., Carbon Nanotubes-the Route Toward Applications. Science 2002, 297, (5582), 787-792.

[3] Laila, S.-H.-I.; Bernhard, B.; Itamar, W., Efficient Generation of Photocurrents by Using CdS/Carbon Nanotube Assemblies on Electrodes. Angew. Chem. Int. Ed. 2005, 44, (1), 78-83.

[4] Kongkanand, A.; Martinez Dominguez, R.; Kamat, P. V., Single Wall Carbon Nanotube Scaffolds for Photoelectrochemical Solar Cells. Capture and Transport of Photogenerated Electrons. Nano Lett. 2007, 7, (3), 676-680.

[5] Cho, N.; Choudhury, K. R.; Thapa, R. B.; Sahoo, Y.; Ohulchanskyy, T.; Cartwright, A. N.; Lee, K. S.; Prasad, P. N., Efficient Photodetection at IR Wavelengths by Incorporation of PbSe-Carbon-Nanotube Conjugates in a Polymeric Nanocomposite. Adv. Mater. 2007, 19, (2), 232-236.

[6] Zhu, L.-P.; Liao, G.-H.; Huang, W.-Y.; Ma, L.-L.; Yang, Y.; Yu, Y.; Fu, S.-Y., Preparation, characterization and photocatalytic properties of ZnO-coated multi-walled carbon nanotubes. Mater. Sci. Eng., B 2009, 163, (3), 194-198.

[7] Hu, L.; Zhao, Y. L.; Ryu, K.; Zhou, C.; Stoddart, J. F.; Grüner, G., Light-Induced Charge Transfer in Pyrene/CdSe-SWNT Hybrids. Adv. Mater. 2008, 20, (5), 939-946.

[8] Banerjee, S.; Wong, S. S., Synthesis and Characterization of Carbon Nanotube-nanocrystal Heterostructures. Nano Lett. 2002, 2, (3), 195-200.

[9] Jiang, K.; Eitan, A.; Schadler, L. S.; Ajayan, P. M.; Siegel, R. W.; Grobert, N.; Mayne, M.; Reyes-Reyes, M.; Terrones, H.; Terrones, M., Selective Attachment of Gold Nanoparticles to Nitrogen-Doped Carbon Nanotubes. Nano Lett. 2003, 3, (3), 275-277.

[10] Han, L.; Wu, W.; Kirk, F. L.; Luo, J.; Maye, M. M.; Kariuki, N. N.; Lin, Y.; Wang, C.; Zhong, C.-J., A Direct Route toward Assembly of Nanoparticle-Carbon Nanotube Composite Materials. Langmuir 2004, 20, (14), 6019-6025.

[11] Jeong, S.; Shim, H. C.; Kim, S.; Han, C.-S., Efficient Electron Transfer in Functional Assemblies of Pyridine-Modified NQDs on SWNTs. ACS Nano 2009, 4, (1), 324-330.

[12] Quinn, B. M.; Dekker, C.; Lemay, S. G., Electrodeposition of Noble Metal Nanoparticles on Carbon Nanotubes. J. Am. Chem. Soc. 2005, 127, (17), 6146-6147.

[13] Robel, I.; Bunker, B. A.; Kamat, P. V., Single-Walled Carbon Nanotube-CdS Nanocomposites as Light-Harvesting Assemblies: Photoinduced Charge-Transfer Interactions. Adv. Mater. 2005, 17, (20), 2458-2463.

[14] Qu, L.; Dai, L., Substrate-Enhanced Electroless Deposition of Metal Nanoparticles on Carbon Nanotubes. J. Am. Chem. Soc. 2005, 127, (31), 10806-10807.

[15] Mubeen, S.; Zhang, T.; Yoo, B.; Deshusses, M. A.; Myung, N. V., Palladium Nanoparticles Decorated Single-Walled Carbon Nanotube Hydrogen Sensor. J. Phys. Chem. C 2007, 111, (17), 6321-6327.

[16] Otakar, F.; Martin, K.; Ladislav, K.; Marketa, Z.; Jan, P.; Mariana, K.; Lothar, D., Structural properties and electrochemical behavior of CNT-TiO2 nanocrystal heterostructures. Phys. Status Solidi B 2007, 244, (11), 4040-4045.

[17] Bai, H. P.; Lu, X. X.; Yang, G. M.; Yang, Y. H., Hydrogen peroxide biosensor based on electrodeposition of zinc oxide nanoflowers onto carbon nanotubes film electrode. Chin. Chem. Lett. 2008, 19, (3), 314-318.

[18] Ting, Z.; Megan B, N.; Bong-Young, Y.; Marc A, D.; Nosang V, M., Electrochemically Functionalized Single-Walled Carbon Nanotube Gas Sensor. Electroanalysis 2006, 18, (12), 1153-1158.

[19] Ting, Z.; Syed, M.; Elena, B.; Bong Young, Y.; Robert, C. H.; Nosang, V. M.; Marc, A. D., Poly(m-aminobenzene sulfonic acid) functionalized single-walled carbon nanotubes based gas sensor. Nanotechnology 2007, (16), 165504.

[20] Maxwell, C. K.; Bong Young, Y.; Young Woo, R.; Krassimir, N. B.; Wilfred, C.; Ashok, M.; Nosang, V. M., Synthesis and characterization of cadmium telluride nanowire. Nanotechnology 2008, (32), 325711.

[21] Panicker, M. P. R.; Knaster, M.; Kroger, F. A., Cathodic Deposition of CdTe from Aqueous Electrolytes. J. Electrochem. Soc. 1978, 125, (4), 566-572.

[22] Danaher, W. J.; Lyons, L. E., The kinetics of the electrodeposition of cadmium telluride. Aust. J. Chem. 1984, 37, (4), 689-701.

[23] Tans, S. J.; Verschueren, A. R. M.; Dekker, C., Room-temperature transistor based on a single carbon nanotube. Nature 1998, 393, (6680), 49-52.

[24] Jae-Hong, L.; et al., Electrical and gas sensing properties of polyaniline functionalized single-walled carbon nanotubes. Nanotechnology 2010, 21, (7), 075502.

[25] Lim, J.-H.; Phiboolsirichit, N.; Mubeen, S.; Rheem, Y.; Deshusses, M. A.; Mulchandani, A.; Myung, N. V., Electrical and Sensing Properties of Single-Walled Carbon Nanotubes Network: Effect of Alignment and Selective Breakdown. Electroanalysis 2010, 22, (1), 99-105.

[26] Martel, R.; Schmidt, T.; Shea, H. R.; Hertel, T.; Avouris, P., Single- and multi-wall carbon nanotube field-effect transistors. Appl. Phys. Lett. 1998, 73, (17), 2447-2449.

[27] Wang, G.; Swensen, J.; Moses, D.; Heeger, A. J., Increased mobility from regioregular poly(3-hexylthiophene) field-effect transistors. J. Appl. Phys. 2003, 93, (10), 6137-6141.

[28] Kazaoui, S.; Minami, N.; Matsuda, N.; Kataura, H.; Achiba, Y., Electrochemical tuning of electronic states in single-wall carbon nanotubes studied by in situ absorption spectroscopy and ac resistance. Appl. Phys. Lett. 2001, 78, (22), 3433-3435.

[29] Lovall, D.; Buss, M.; Graugnard, E.; Andres, R. P.; Reifenberger, R., Electron emission and structural characterization of a rope of single-walled carbon nanotubes. Phys. Rev. B 2000, 61, (8), 5683.

[30] Orlowski, B. A.; Lacharme, J. P.; Bensalah, S.; Sebenne, C. A., Electronic properties of cleaved CdTe(110) surfaces. Surf. Sci. 1988, 200, (1), L460-L464.

[31] Takahashi, M.; Uosaki, K.; Kita, H.; Yamaguchi, S., Resistivity, carrier concentration, and carrier mobility of electrochemically deposited CdTe films. J. Appl. Phys. 1986, 60, (6), 2046-2049.

[32] Holzinger, M.; Abraham, J.; Whelan, P.; Graupner, R.; Ley, L.; Hennrich, F.; Kappes, M.; Hirsch, A., Functionalization of Single-Walled Carbon Nanotubes with (R-)Oxycarbonyl Nitrenes. J. Am. Chem. Soc. 2003, 125, (28), 8566-8580.

[33] Lee, K. Y.; Kim, M.; Lee, Y. W.; Lee, J.-J.; Han, S. W., Fabrication of metal nanoparticles-carbon nanotubes composite materials in solution. Chem. Phys. Lett. 2007, 440, (4-6), 249-252.

[34] Hecht, D. S.; Ramirez, R. J. A.; Briman, M.; Artukovic, E.; Chichak, K. S.; Stoddart, J. F.; Grüner, G., Bioinspired Detection of Light Using a Porphyrin-Sensitized Single-Wall Nanotube Field Effect Transistor. Nano Lett. 2006, 6, (9), 2031-2036.

Chapter 8

Chemical transformation into Te-based Nanostructures

8.1 Abstract

We demonstrated a simple and inexpensive method for the synthesis of compound semiconductors (*e.g.* Pb_xTe_y, Ag_xTe_y and Cd_xTe_y) from sacrificial metal thin films (*e.g.* Co) by chemical transformation including galvanic displacement (GD) and cation exchange reaction (CER).

8.2 Introduction

Compound semiconductors, especially nanostructures, have attracted intense interest due to their important properties in fundamental research and their potential applications in nanoscale electronics, optoelectronics, and energy harvesting devices [1-3]. However, finding a cost-effective and simple synthesis process with the capability to control structures and properties is one of the most critical challenges ahead of the successful development of compound semiconductors [3-5]. Recently, chemical transformation techniques such as galvanic displacement (GD) and cation exchange reaction (CER) have proven to be effective and promising approaches for synthesizing compound semiconductors with tunable nanostructures, compared to conventional methods [6-12]. Since GD and CER take advantage of the difference in redox potential and thermodynamic flavor between the materials themselves, this chemical transformation provides a simple (basic immersion of the sample into the electrolyte) and inexpensive

(no external energy needed) way to fabricate compound semiconductors with nanostructures from relatively cheap metal substrates [11-14].The investigation of the growth of nanostructures in compound semiconductors by chemical transformation offers the greatest possibility for further scientific development in this area.

In this chapter, we report a simple methodology for synthesizing nanostructures in compound semiconductors from sacrificial Co thin films. Through chemical transformation, the electrodeposited sacrificial metal thin films (*e.g.* Co) can be transformed into compound semiconductors (*e.g.* Pb_xTe_y, Ag_xTe_y and Cd_xTe_y) with enhanced active surface area while still preserving the initial nanostructures that were present during GD and CER. By adjusting the thickness of sacrificial Co layers on Pt substrates, initial nanostructures can be tuned from cucumber-like, x-shaped structures to flower-like structures.

8.3 Experimental Section

The sacrificial Co thin films were galvanostatically electrodeposited by contacting a chloride bath that contained 1 M $CoCl_2$ + 1 M $CaCl_2$ with a Pt-coated $Ti/SiO_2/Si$ substrate under mild conditions (room temperature). Calcium chloride was used as a supporting electrolyte. The electrolyte pH was maintained at 3 with HCl and NaOH. The electrodeposition was carried out using a Princeton Applied Research Potentiostat (VMP2) at a current density of 5 mA cm^{-2} with a traditional three-electrode cell. A platinum substrate with a surface area of 1 cm^2, a saturated calomel electrode (SCE) and platinum-coated titanium anode were used as a working, reference and counter electrode,

respectively. Electrodeposition parameters such as deposition time were varied to prepare sacrificial Co thin films of thicknesses ranging from 1 to 5 μm.

The electrolyte for galvanic displacement was composed of 10 mM $HTeO_2^+$ + 50mM Pb^{2+} in 1 M HNO_3, and solution pH was maintained at pH 1. The electrodeposited Co thin films on Pt substrate were immersed into the electrolyte for 1hr at room temperature. The sample was then rinsed with DI water. To investigate the effect of the thickness of the sacrificial layer on the surface morphology of the samples, galvanic displacement was carried out for each Co thin films with thicknesses ranging from 1 to 5 μm.

Synthesized Pb_xTe_y thin films by GD were immersed into electrolyte containing 50 mM $Ag(NO)_3$ at room temperature to conduct the CER of Ag_xTe_y. The reaction was allowed to proceed until sufficient transformation occurred, (for 24 hrs). After the CER was completed, DI water was used to rinse the sample. It was then dried out in the air. Following the CER of Cd_xTe_y, the as-prepared Ag_xTe_y thin films were dipped into an electrolyte containing 1.3 mg/ ml of $Cd(NO_3)_2$ in methanol with 0.2 ml of tributylphosphine (TBP) at 50^oC for 24hrs. The same cleaning procedure was repeated after this process.

Surface morphology and cross-sectional images were obtained by a scanning electron microscope (SEM, XL30-FEG, Phillips). Further, the film element compositions were obtained by energy-dispersive spectroscopy (EDS, EDAX, Phoenix). An X-ray diffractometer (XRD, D8 Advance Diffractometer, Bruker) with Cu Kα radiation (operating at 40kV) was used for the phase identification of as-synthesized samples, and

the patterns from 100 to 800 with increments of 0.020 and a 0.5 s collection time per increment were recorded.

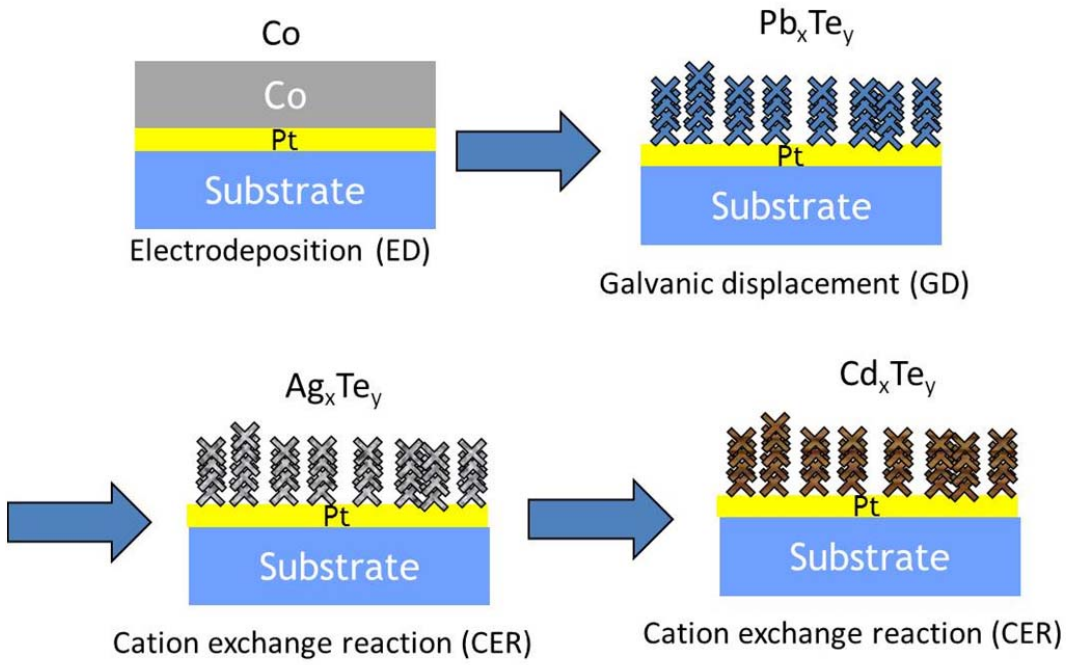

Figure 8.1. Schematic illustration of chemical transformation. The as-prepared Co sacrificial thin films by electrodeposition (ED) were galvanically displaced (GD) to Pb_xTe_y thin films with x-shaped nanostructures. Subsequently, the nanostructures of Pb_xTe_y were chemically transformed into Ag_xTe_y and Cd_xTe_y via cation exchange reaction (CER).

8.4 Results and Discussion

8.4.1 Chemical Transformation From Metal to Compound Semiconductor

Figure 8.1 illustrates a schematic of the chemical transformation from sacrificial Co thin films to Cd_xTe_y thin films with hierarchical nanostructures on Pt substrate. As depicted in Figure 8.1, this chemical transformation is composed of four steps: (i)

electrodeposition of sacrificial Co thin films with various thicknesses on Pt substrate, (ii) galvanic displacement (GD) of sacrificial layer to form x-shaped nanostructures of Pb_xTe_y thin films, (iii) cation exchange reaction (CER) of Pb_xTe_y thin films into Ag_xTe_y, and (iv) further CER for synthesis of Cd_xTe_y thin films while preserving their nanostructures. During GD, the electrochemical reactions between oxidation of sacrificial Co and reduction of metal ions (Pb^{2+} and $HTeO_2^+$) simultaneously occurred due to their difference of redox potential. Once the GD was finished, the active surface area of Pb_xTe_y thin films were dramatically increased compared to the sacrificial Co thin films since the x-shaped Pb_xTe_y nanostructureswere grown towards the direction opposite of the substrate with stem structures. Then this thin film was chemically transformed to Ag_xTe_y with a preservation of structures followed by continuous CER of these nanostructures until it was fully converted into Cd_xTe_y thin films. While the exact mechanism of cation exchange is not yet clearly understood, Moon et al. postulate that the governing factors are different solubility of the ionic solids in the reaction medium and thermodynamic flavor of CER [12]. Figure 8.2 shows SEM images of cross-sectional view of sacrificial Co thin film and as-synthesized Pb_xTe_y, Ag_xTe_y and Cd_xTe_y thin films on Pt substrate, respectively. The electrodeposited sacrificial Co thin film with a thickness of ~3 μm has a sponge-like structure as shown in Figure 8.2(a). On the other hand, Figure 8.2(b)-(d) show that the morphology and amount of deposits are greatly changed during chemical transformation in relation to sacrificial Co thin films. When the GD was started as the first reaction (Figure 8.2(b)), the Pb_xTe_y film became thicker due to the formation of Pb_xTe_y nanostructures and an x-shape Pb_xTe_y with stem structures formed on the surface

of Pt substrate. The following chemical transformations for Ag_xTe_y and Cd_xTe_y preserve the initial stem structures with x-shape on the top , only slightly increasing the size of the nanostructures due to volume expansion, as presented in Figure 8.2(c)-(d). The preservation of the structure and the volume expansion are consistent with the observations that have been reported in the literature [12].

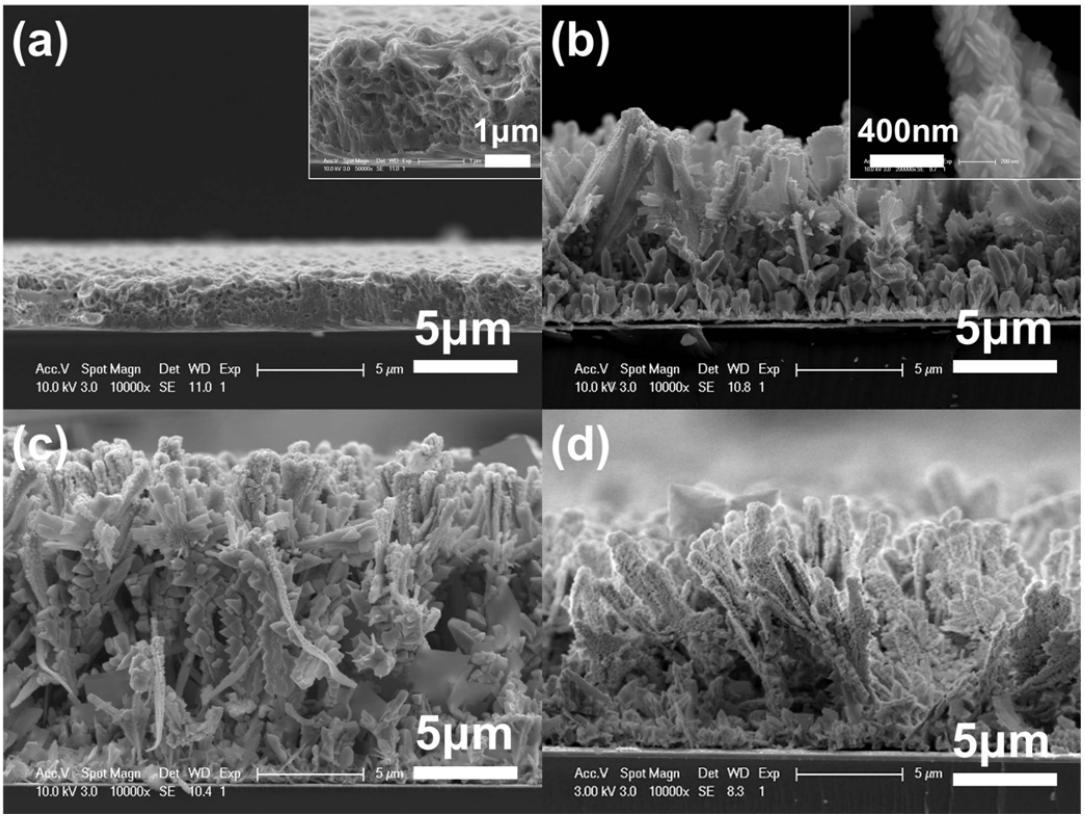

Figure 8.2. Cross-sectional SEM images of (a) as-prepared Co sacrificial thin films with a thickness of ~3 µm, and chemically transformed (b) Pb_xTe_y, (c) Ag_xTe_y and (d) Cd_xTe_y thin films through galvanic displacement (GD) and cation exchange reaction (CER). Fig. 2(b) inset shows the top view of stem structures, which are x-shaped Pb_xTe_y nanostructures.

In order to confirm the chemical transformation, the energy-dispersive spectroscopy (EDS) spectrum and X-ray diffractometer (XRD) pattern were obtained in each step of reaction. As shown in Figure 8.3(a), the deposited Pb content in EDS spectrum continuously decreases as on the reaction proceeds, and reaches to zero, meaning that the Pb^{2+} cations are completely exchanged to other cations such as Ag^{+} and Cd^{2+}. Consequently, the intensity of the peaks for chemically transformed Ag and Cd rapidly increase in each reaction step. A detailed analysis on the composition of each sample will be discussed in a later section. Figure 8.3(b) shows XRD patterns of as-synthesized Pb_xTe_y, Ag_xTe_y and Cd_xTe_y nanostructures on the Pt substrate. It can be clearly seen that the peak of galvanically synthesized Pb_xTe_y have a face-centered cubic (FCC) structure according to JCPDS 38-1435 with the hexagonal Te (JCPDS 36-1452) structures, which can be attributed to the relatively higher deposited Te content (~ 80 at.%) compared to deposited Pb content (~ 20 at.%) (composition of Pb_xTe_y will be shown in next section). As the cation is exchanged into Ag, the XRD patterns verify that the as-prepared Ag_xTe_y are composed of monoclinic β-Ag_2Te (JCPDS 34-0142) structures. The patterns co-exist with the peak of Pb_xTe_y after a cation exchange with Ag^{+}, which might be caused by the remaining the Pb_xTe_y content in the sample. This analysis is consistent with the EDS spectrum of Ag_xTe_y sample. Meanwhile, the peak of the as-synthesized Cd_xTe_y show that they are composed of composite structures with FCC (PDF 15-0770) along with (111), (311) and (331) planes, and orthorhombic phases (JPCDS 41-0941) corresponding to the (001), (011) and (020) planes.

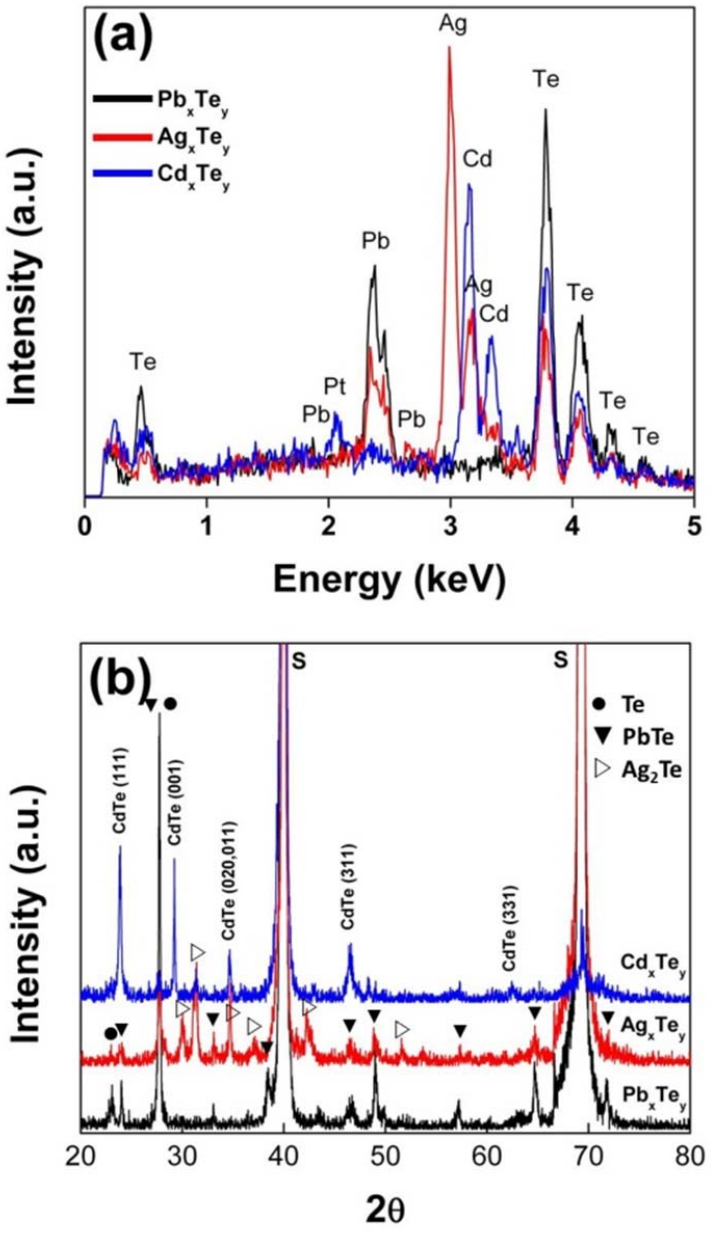

Figure 8.3. (a) EDS spectrum and (b) XRD pattern of as-synthesized Pb_xTe_y, Ag_xTe_y and Cd_xTe_y thin films during the each reaction step of chemical transformation. The samples were synthesized from ~3 μm thick sacrificial Co thin film. (S in Fig. 3(b) : substrates – Pt and Si).

8.4.2 Effect of Thickness of Sacrificial Co Thin Films

For further investigation, the effect of thickness of sacrificial Co thin films on chemical transformation was carried out by varying the thickness of the sacrificial layers on Pt substrate as 1, 3 and 5 μm. As shown in Figure 8.4-6, results clearly indicate the dependence of surface morphology on the sacrificial layer thickness, which varied from cucumber-like (Figure 8.5(a)), x-shaped (Figure 8.5(b)) to flower-like (Figure 8.5(c)) structures, respectively. Figure 8.4(a)-(c) also show that the sparser and bigger nanostructures of Pb_xTe_y were formed by galvanic displacement on increasing thicknesses of the sacrificial Co layers. As the reaction proceeds, the initial nanostructures of Pb_xTe_y are grown accordingly (volume expansion), and then chemically transformed into Ag_xTe_y (Figure 8.4(d)-(f)) and Cd_xTe_y (Figure 8.4(g)-(i)) with well preserved initial nanostructures in each reaction step. This result implies that the initial nanostructures of Pb_xTe_y are dependent on the thickness of sacrificial layer during the GD, and that it also affects the next surface morphology for further chemical transformation. This means that the surface morphology of nanostructures can be modulated by simple adjustment of the thickness of the sacrificial layer on substrate.

The deposited contents of the as-synthesized thin films in each reaction step were measured as a function of thickness of sacrificial Co thin films. As shown in Figure 8.7(a), this analysis confirms that the amount of deposited Pb and Te content is independent of the sacrificial Co thin films thickness, showing the Te-rich Pb_xTe_y within a range of 72~81 at.% Te content. This may be due to the faster deposition rate of Te(s) compared to deposition of Pb^{2+} to form Pb_xTe_y compound (two-step deposition

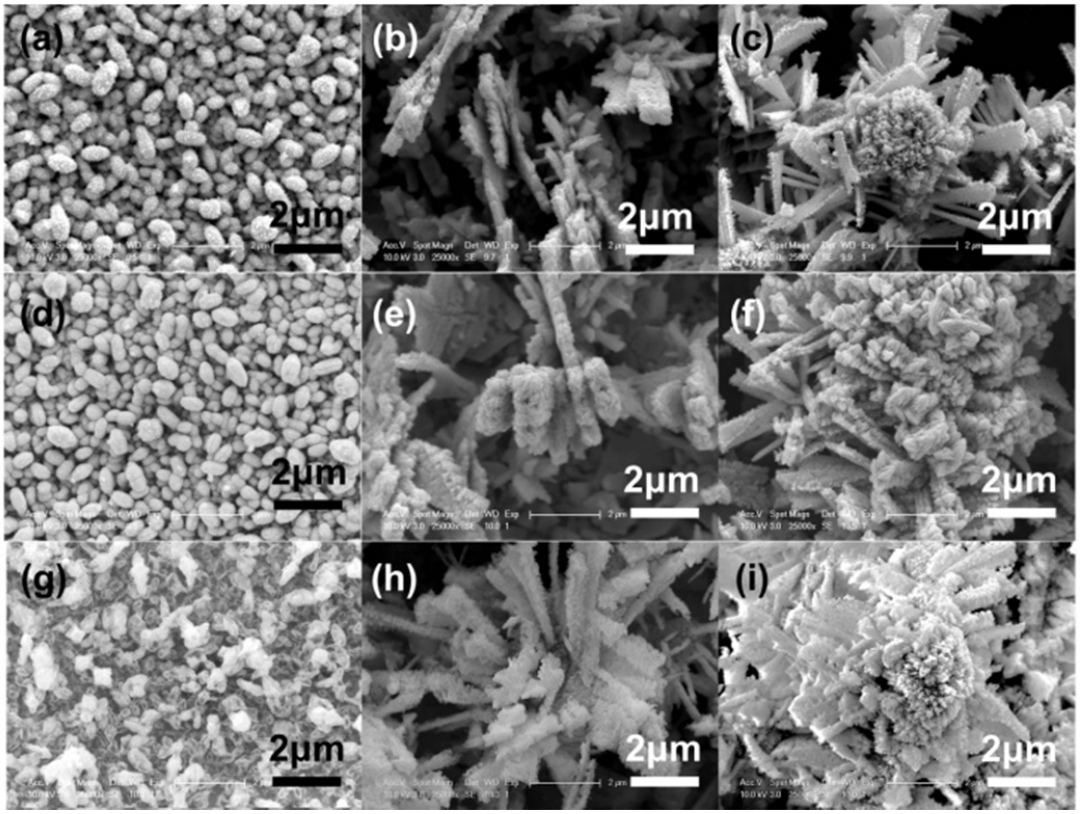

Figure 8.4. SEM images of as-synthesized (a-c) Pb_xTe_y, (d-f) Ag_xTe_y and (g-i) Cd_xTe_y thin films through galvanic displacement (GD) and cation exchange reaction (CER). The samples were chemically transformed from the sacrificial Co thin films with 1 (a,d,g), 3 (b,e,h) and 5 (c,f,i) μm thickness, respectively.

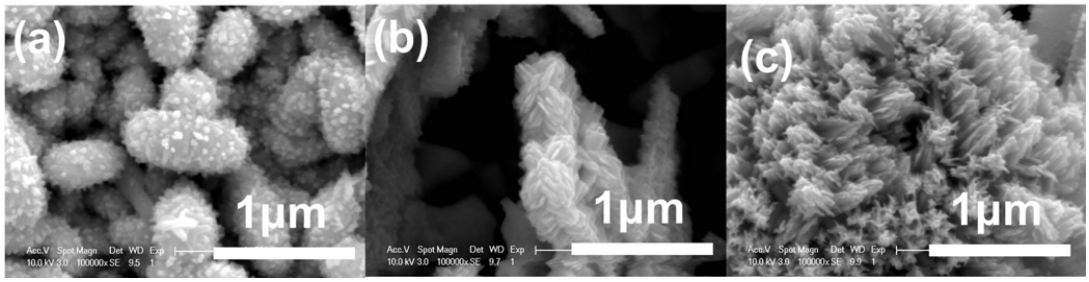

Figure 8.5. SEM images of as-synthesized Pb_xTe_y nanostructures as a function of thickness of sacrificial Co thin films. The samples were galvanically formed from the sacrificial Co thin films with (a) 1, (b) 3 and (c) 5 μm thickness, respectively.

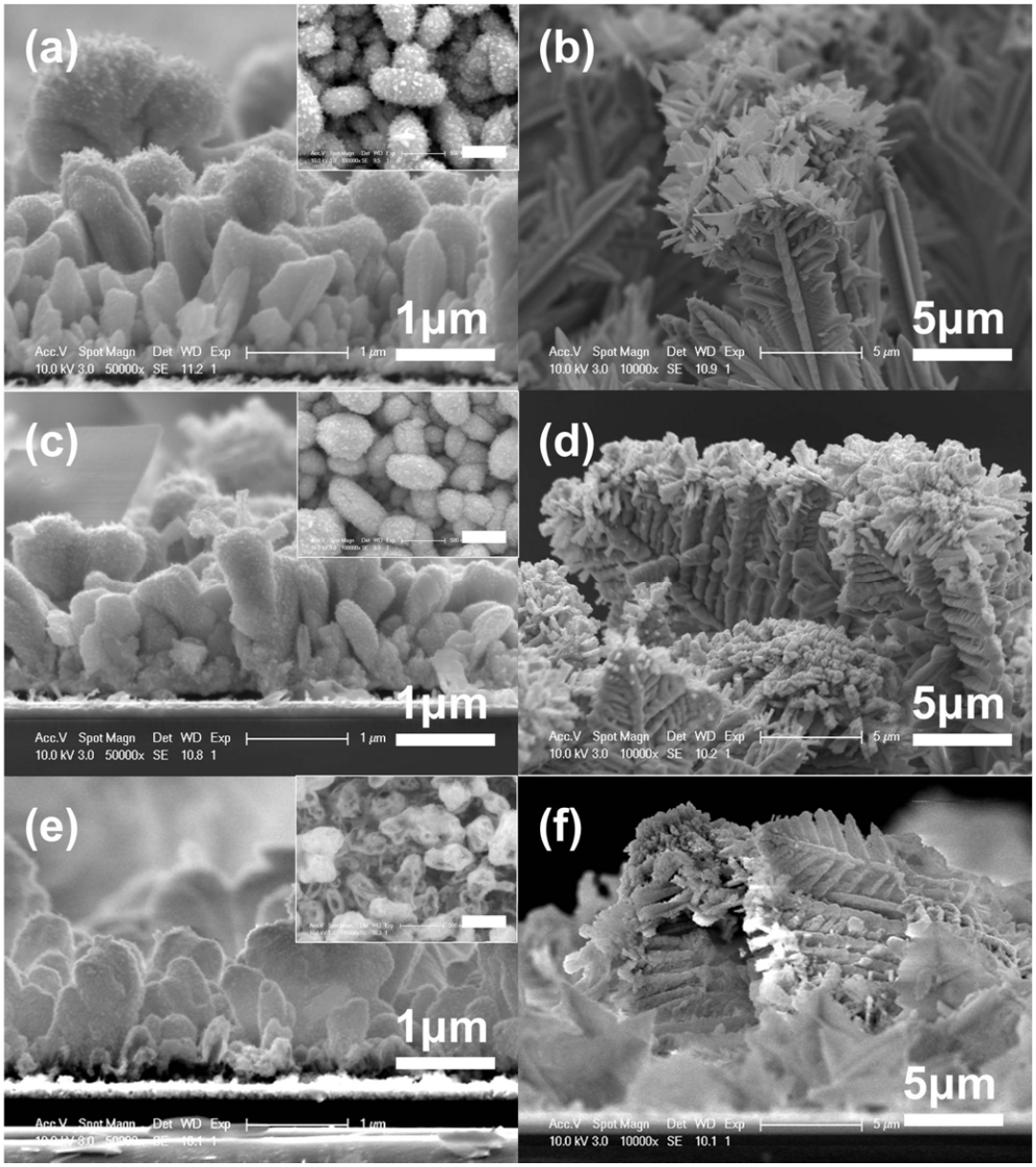

Figure 8.6. Cross-sectional SEM images of as-synthesized (a)-(b) Pb_xTe_y, (c)-(d) Ag_xTe_y and (e)-(f) Cd_xTe_y thin films. The samples were chemically transformed from the sacrificial Co thin films with 1 (a,c,e) and 5 (b,d,f) µm thickness, respectively. Inset images represent the top view of nanostructures. Scare bar (inset) = 400 nm.

mechanism) during GD. As expected, the deposited content of Ag is sharply increased after cations of Pb^{2+} were exchanged into Ag^{+} to form the Ag_xTe_y by CER (Figure 5(b)).

This figure also shows that the remaining Pb content in Ag_xTe_y after CER is relatively higher in the sample that were prepared with 1 μm thick sacrificial Co thin films. This may be caused by their denser structures, resulting in a smaller active surface area cation exchange than those with sparser nanostructures (5 μm). Conversely, this also leads to the conclusion that samples synthesized with 5 μm thick sacrificial Co thin films reach the stoichiometric composition of Ag_2Te in sparser structures. Figure 5(c) shows that all the samples reached the stoichiometric composition of CdTe, while the remaining content of Pb and Ag is negligible within the range of error. This result demonstrates that the CER process in the final step from Ag_xTe_y into Cd_xTe_y is completed.

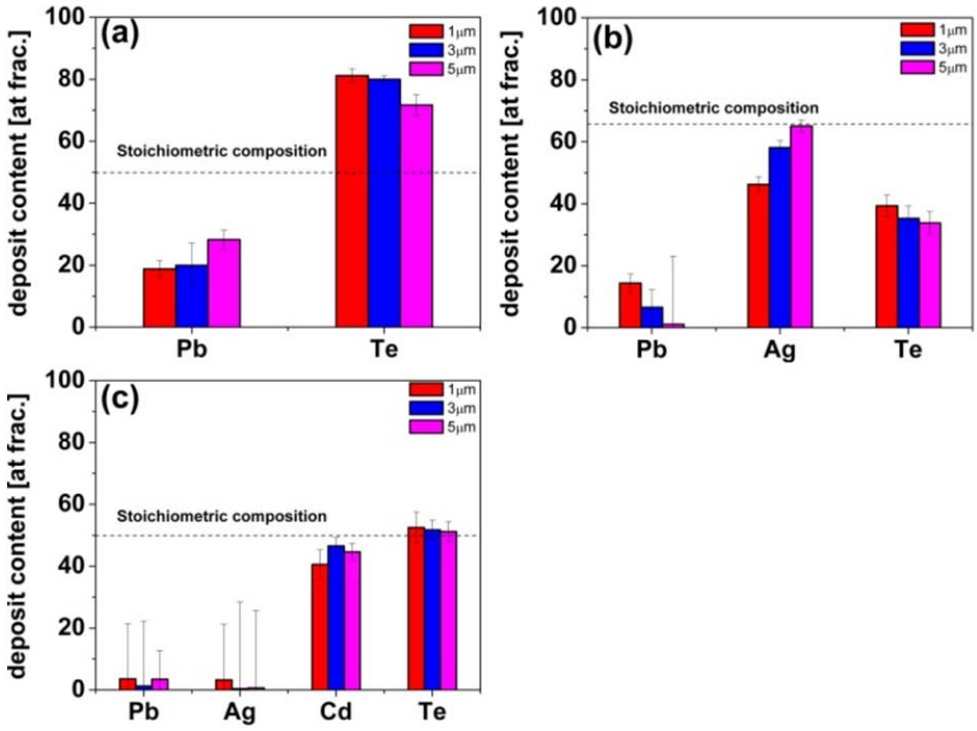

Figure 8.7. Deposited content in (a) Pb_xTe_y, (b) Ag_xTe_y, and (c) Cd_xTe_y thin films as a function of thickness of sacrificial Co thin films.

8.5 Conclusions

In summary, we demonstrated a simple and cost-effective route of chemical transformation from sacrificial metal thin films (*e.g.* Co) for nanostructures in compound semiconductors (*e.g.* Pb_xTe_y, Ag_xTe_y and Cd_xTe_y). By utilizing the GD and CER, the electrodeposited sacrificial Co thin films were chemically transformed into Pb_xTe_y, Ag_xTe_y and Cd_xTe_y with enhanced active surface area while preserving their initial nanostructures in the each reaction step. Furthermore, the initial nanostructures of Pb_xTe_y were easily tuned by adjusting the thickness of sacrificial Co thin films on the substrate during the GD, which could influence all nanostructures for further chemical transformation. This study provides a new and easy path for the synthesis of nanostructures in compound semiconductors by GD and CER from sacrificial Co thin films. Therefore, this synthetic approach will enable us to facilitate the fabrication and may be a general way to produce other semiconductor nanostructures from relatively cheap material.

8.6 References

[1] X. Fang, Y. Bando, U. K. Gautam, C. Ye and D. Golberg, *J. Mater. Chem.*, 2008, **18**, 509-522

[2] A. I. Hochbaum and P. Yang, *Chem. Rev.*, 2009, **110**, 527-546; A. Majumdar, *Science*, 2004, **303**, 777-778.

[3] M. Law, J. Goldberger and P. Yang, *Annu. Rev. Mater. Res.*, 2004, **34**, 83-122.

[4] Y. Xia, P. Yang, Y. Sun, Y. Wu, B. Mayers, B. Gates, Y. Yin, F. Kim and H. Yan, *Adv. Mater.*, 2003, **15**, 353-389

[5] J. C. Hulteen and C. R. Martin, *J. Mater. Chem.*, 1997, **7**, 1075-1087.

[6] C. H. Chang, Y. Rheem, Y.-H. Choa, D.-Y. Park and N. V. Myung, *Electrochim. Acta*, 2010, **55**, 1072-1080

[7] C. H. Chang, Y. Rheem, Y.-H. Choa, D. H. Shin, D.-Y. Park and N. V. Myung, *Electrochim. Acta*, 2010, **55**, 743-752

[8] H. Jung, Y. Rheem, N. Chartuprayoon, J.-H. Lim, K.-H. Lee, B. Yoo, K.-J. Lee, Y.-H. Choa, P. Wei, J. Shi and N. V. Myung, *J. Mater. Chem.*, 2010, **20**, 9982-9987

[9] Y. Rheem, C. H. Chang, C. M. Hangarter, D.-Y. Park, K.-H. Lee, Y.-S. Jeong and N. V. Myung, *Electrochim. Acta*, 2010, **55**, 2472-2476

[10] F. Xiao, B. Yoo, K. H. Lee and N. V. Myung, *J. Am. Chem. Soc.*, 2007, **129**, 10068-10069.

[11] U. Jeong, P. H. C. Camargo, Y. H. Lee and Y. Xia, *J. Mater. Chem.*, 2006, **16**, 3893-3897.

[12] G. D. Moon, S. Ko, Y. Xia and U. Jeong, *ACS Nano*, 2010, **4**, 2307-2319.

[13] M. S. Milan Paunovic, *Fundamentals of Electrochemical Deposition*, Wiley-Interscience, 2nd edn., 2006

[14] R. D. Robinson, B. Sadtler, D. O. Demchenko, C. K. Erdonmez, L.-W. Wang and A. P. Alivisatos, *Science*, 2007, **317**, 355-358.

Chapter 9

Summary and Conclusions

The overall goal of this doctoral work was to develop an electrochemical technique to synthesize chalcogenide nanostructures that can effectively control their size, surface morphology and composition by tailoring experimental parameters, and to systematically investigate their electrical and optoelectrical properties by understanding their growth mechanisms and elucidating the relationship between synthetic parameters and the nanomaterial products. To reach this goal, three chalcogenide materials – Bismuth telluride (Bi_xTe_y) Lead telluride (Pb_xTe_y) and Cadmium telluride (Cd_xTe_y) – were selected as a TE and PV materials. By utilizing electrochemical techniques such as electrodeposition (ED) and galvanic displacement (GD), successful synthesis of nanostructured chalcogenide materials were from sacrificial iron group thin films (e.g. Ni, Co and Fe) was demonstrated. Furthermore, their size (nano to micro), surface morphology (from novel nanostructures to nanoparticles and core/shell hybrid nanostructure) and composition (excess either electropositive element or chalcogens) were shown to be simply and easily tuned by tailoring the electrochemical parameters such as electrolyte composition, type and thickness of sacrificial materials, and reation time. These systematical investigations are expected to allow further synthesis and to establish an experimental design for other nanostructured chalcogenide materials.

Following the brief introduction and overview of TE and PV followed by their materials and synthetic techniques in chapter 1, this dissertation was categorized into two

main parts: Electrochemical synthesis and characterization of TE materials, and PV materials. For the TE materials, hierarchical Bi_xTe_y nanostructures with controlled composition and surface morphology were investigated in chapter 2, and their three-step growth mechanism was explored in chapter 3. Furthermore, results of the synthesis of individual electropositive element (Bi) and chalcogen (Te), and investigation of the effect of their surface morphology, was shown in chapter 4. On the basis of this, the use of an electrochemical method to synthesize the size-controlled Te nanotubes from sacrificial Co nanowires was demonstrated in chapter 5. Finally, the electrochemical process was extended to the synthesis of further lead chalcogenide nanostructures such as Pb_xTe_y, with complete control over their surface morphology, composition, and growth direction as indicated in chapter 6. Moreover, cadmium chalcogenide material (CdTe) was introduced as a means to functionalize SWNTs for fabrication of CdTe NPs/SWNTs hybrid nanostructures, and their electrical and optoelectrical properties were investigated in chapter 7. Finally, a new approach for synthesizing Te-based chalcogenide materials was introduced by chemical transformation from sacrificial Co thin films in Chapter 8.

Detailed results from each chapter include:

Chapter 2 Electrochemical Synthesis of Bi_xTe_y Nanostructures

- Synthesis of Bi_xTe_y thin films by galvanic displacement with three sacrificial thin films (Ni, Co and Fe).
- Strong dependence of surface morphologies (from fine granular to hierarchical structure), crystal structures and compositions (from $Bi_{0.6}Te_{4.4}$ to

$Bi_{1.9}Te_{3.1}$) of the as-synthesized thin films to the types of the sacrificial materials and the $[Bi^{3+}]/[HTeO_2^{+}]$ ratio in the electrolyte.

- Interpretation of OCP analysis: (i) redox reactions occurred simultaneously between the targeted materials (Bi_xTe_y) and the sacrificial metal thin films (Ni, Co and Fe), (ii) the values of the OCP shifted toward more positive values as the available surface area for galvanic displacement decreased, and (iii) the potentials remained at constant positivevalues after the redox reaction had finished.

Chapter 3 Growth Mechanism of Hierarchical Bi_xTe_y Nanostructures

- Three-step growth mechanism of hierarchical Bi_xTe_y nanostructures: (a) the formation and nucleation of star-shaped Bi_xTe_y in the initial stage (0.5 to 3 min), (b) the growth of star-shaped nanostructures to form spindle-shaped Bi_xTe_y with a few branches between 3 to 15 min, and (c) the continuous growth of spindle structures and formation of additional sub-branches on the initial nanostructure (up to 60 min).

Chapter 4 Electrochemical Synthesis of Bi and Te Nanostructures

- Synthesis of Bi and Te thin films by galvanic displacement with three different types of the sacrificial thin films (Ni, Co and Fe).

- Strong dependence of surface morphologies (from hexagonal nanoplatelets to polygon structures) of the as-synthesized thin films on the types and thickness of the sacrificial materials.

Chapter 5 Electrochemical Synthesis of Te Nanotubes

- Synthesis of Te nanotubes (average grain size below 10 nm) from sacrificial Co nanowires by galvanic displacement reactions
- Tunable diameter, wall thickness (from 15 to 30 nm) and length of Te nanotubes by adjusting the diameter and length of the sacrificial nanowires.
- Overview of typical p-type semiconductors with field effect mobility of approx. 0.01 cm^2/Vs.

Chapter 6 Electrochemical Synthesis of Pb_xTe_y Nanostructures

- Synthesis of novel Pb_xTe_y nanostructures by galvanic displacement from sacrificial Co thin films
- Tunable film composition from Te-rich ($Pb_{20}Te_{80}$) to Pb-rich ($Pb_{69}Te_{31}$) by varying the ratio of $[Pb^{2+}]/[HTeO_2^+]$ in the electrolyte
- Strong dependence of surface morphology of Pb_xTe_y (from x-shaped, cucumber-like, flower-like to dendrite structures) to the composition and thickness of sacrificial thin films.

Chapter 7 Electrochemical Synthesis of CdTe NPs/SWNT Hybrid Nanostructures

- Functionalization of SWNTs by CdTe NPs with the capability of controlling their size, surface morphology, and composition by direct electrodeposition.
- Modulation of size and surface morphology of hybrid nanostructures of up to 4 times the magnitude with structures varying from small and nodular structures to the core/shell nanostructures
- Tunable composition of the SWNTs from Te-rich ($Cd_{29}Te_{71}$) to Cd-rich ($Cd_{79}Te_{21}$) by simply varying the applied potential.
- Optoelectrical properties that showed photo-induced current of the CdTe NPs/SWNT hybrid nanostructures under UV irradiation.
- Dependence of the photosensitivity on their size and conductivity type (p-type or n-type).
- Maximum sensitivity of up to 30% through complete coating of the SWNTs with Cd-rich CdTe (n-type).

Chapter 8 Chemical transformation into Te-based Nanostructures

- Demonstration of a simple and cost-effective route of chemical transformation from sacrificial metal thin films (*e.g.* Co) for nanostructures in compound semiconductors (*e.g.* Pb_xTe_y, Ag_xTe_y and Cd_xTe_y).
- Enhanced active surface area while preserving their initial nanostructures in each reaction step.

- Tunability of the initial nanostructures of Pb_xTe_y by adjusting the thickness of sacrificial Co thin films on the substrate during the GD.

Appendix

Electrochemical Synthesis of CdTe NWs/CdS Hybrid Nanostructures Based Solar Cells

Experimental

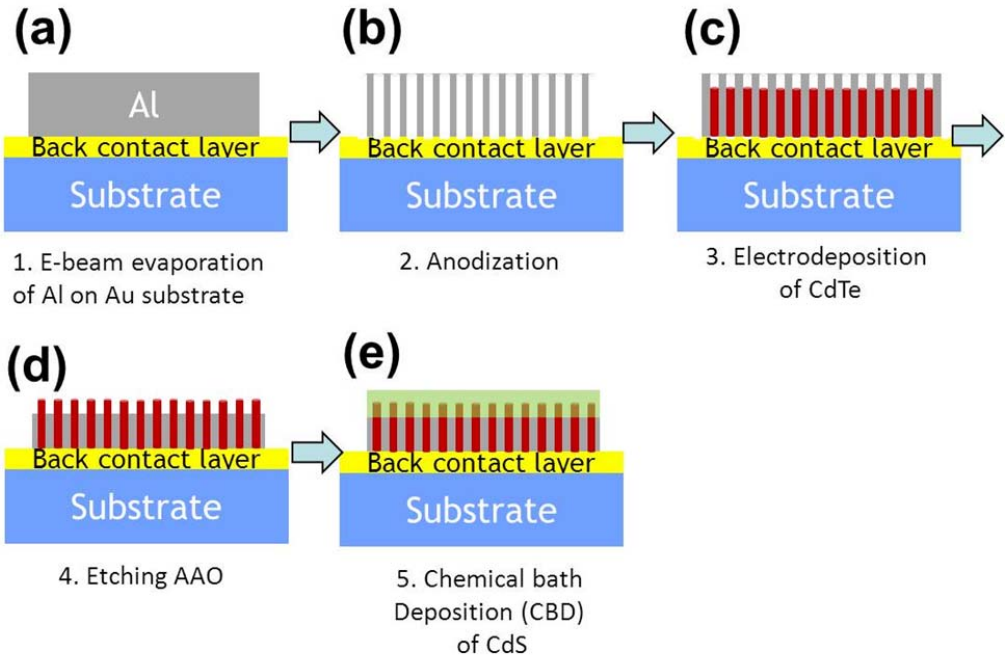

Figure A1.1 Schematic illustration of fabrication of CdTe NWs/CdS hybrid nanostructures based on solar cells at each step: (a) as-prepared Al layer on silicon substrate by e-beam evaporation technique, (b) anodization of Al layer to synthesize nanoporous array, (c) electrodeposition of CdTe NWs into the pore, (d) chemical etching process to expose the top of CdTe NWs, and (e) chemical bath deposition (CBD) of CdS onto exposed CdTe NWs.

The fabrication processes of CdTe NWs/CdS hybrid nanostructures are represented in figure A1.1. An aluminum (Al) substrate was deposited on Au(180 nm)/Ti(20

nm)/SiO_2(100 nm)/Si substrate by electron-beam evaporation process. The Au and Ti layers were used as a back contact materials for solar cells device and as an adhesion layer between Au and SiO_2 layer, respectively. Once the Al substrate was prepared, the Al layer with surface area of 1 cm^2 was anodized in 0.3 M oxalic acid bath at 10^oC with rapid agitation (300 rpm). A two-step anodization process was used to fabricate nanoporous alumina template by applying 50 V for 1 min as the first anodization process followed by 55 V until the anodic current sharply increased then reached to zero. To remove the barrier layer, as-prepared alumina template was submerged into 5 wt. % of phosphoric acid for 60 min at room temperature.

The CdTe nanowires were electrodeposited into the pore of alumina template with the electrolyte containing 1 M $CdSO_4$ and 0.15 mM TeO_2 in 1 M H_2SO_4. The pH of the electrolyte was maintained at 2.0 by adding NaOH and/or H_2SO_4. Electrodeposition was potentiostatically conducted using a Princeton Applied Research Potentiostat (VMP2) at −0.6V vs. SCE. A saturated calomel electrode (SCE) and platinum-coated titanium anode were used as a reference and a counter electrode, respectively. Then the alumina template was partially etched by adding 0.1 M NaOH to expose the CdTe nanowires.

For the chemical bath deposition (CBD) of CdS, the electrolyte composed of 100 mM $Na_2S_2O_3$ and 100 mM $CdSO_4$ in DI water. The CBD of CdS was carried out 200 mL of electrolyte at 85^oC with vigorous agitation (300 rpm) for 3 hrs. Afterwards, the sample was carefully rinsed with DI water and allowed to dry in the air.

Scanning electron microscope (SEM, XL30-FEG, Phillips) and energy-dispersive spectroscopy (EDS, EDAX, Phoenix) were used to examine the surface morphology and

composition of samples. Phase identification of the thin films was carried out by X-ray diffractometer (XRD, D8 Advance Diffractometer, Bruker) with Cu Kα radiation (operating at 40 kV).

Results and Discussions

Figure A1.2(a) and (b) shows cross-sectional SEM images of Al substrate and anodized alumina template with nanopore on a gold substrate from 0.3 M oxalic acid, respectively. Once the dense aluminum layer with a thickness of ~2.3 μm is deposited by e-beam evaporation technique (Figure A1.2(a)), this Al layer on gold substrate was anodized to acquire the porous alumina nanostructures with pore diameter ~ 50 nm and thickness ~ 3.1 μm (Figure A1.2(b)). The thickness ratio of alumina to anodized Al is 1.33, which is consistent with a previous report in the literature [1]. Figure A1.2(c) shows a typical anodization behavior of a two-step anodization process as a function of time. To monitor the anodization process, the anodic current density was measured (blue line in figure A1.2(c)) while the applied voltage was swept from 50 V for 1 min as the first anodization process followed by 55 V (red line in figure A1.2(c)). This anodic current density curve of Al layer on gold substrate started from a relatively greater value at initial stage of anodization due to the highly conducting aluminum. Then, the rapid current density drops were caused by forming of insulating alumina barrier. As the barrier layer thickness decreased due to the chemical and field-assisted dissolution of alumina, the current density slightly increased to reach a steady state of 12 mA/cm^2. When the most of aluminum oxidized and electrolyte comes into the underlying Au layer, anodic current density was rapidly increased.

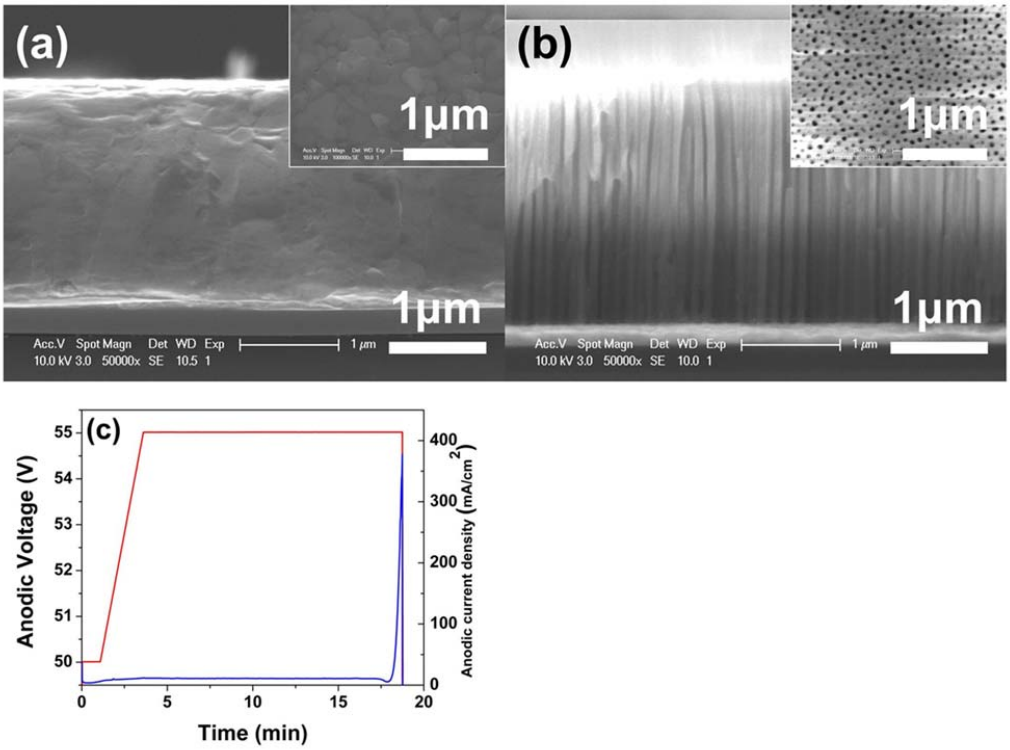

Figure A1.2. SEM images of (a) as-prepared Al layer on $Au/SiO_2/Si$ substrate by e-beam evaporation technique and (b) as-synthesized nanoporous alumina template. (c) Anodic voltage and current density versus time profile during anodization.

Using the as-synthesized alumina template, the CdTe NWs were grown into the nanopore by electrodeposition method with the electrolyte containing 1 M $CdSO_4$ and 0.15 mM TeO_2 in 1 M H_2SO_4. at −0.6 V vs. SCE. Figure A1.3(a) and (b) shows vertically aligned CdTe NWs with a length ~ 2.5 µm after etching the alumina template with 0.1 M NaOH. The electrodeposited CdTe composition and crystal structures were obtained using energy dispersive X-ray spectroscopy (EDS) and X-ray diffractometer (XRD). As shown in figure A1.3(e) and (f), the EDS spectrum and XRD pattern clearly show the peak of Cd and Te with near-stoichiometric composition $Cd_{48}Te_{52}$ and composite structures with hexagonal (PDF 19-0193) along with (103) and (201) planes, and

orthorhombic phases (JPCDS 41-0941) corresponding to the (001), respectively.

Afterwards, the CdS was deposited onto exposed CdTe NWs by chemical bath deposition, which represented that surface morphology of deposited CdS has a granular structure over entire surface. It also confirmed that the cubic structure along with (100) and (200) planes based on the standard JCPDS 21-0829, as shown in figure A1.3(c)-(f).

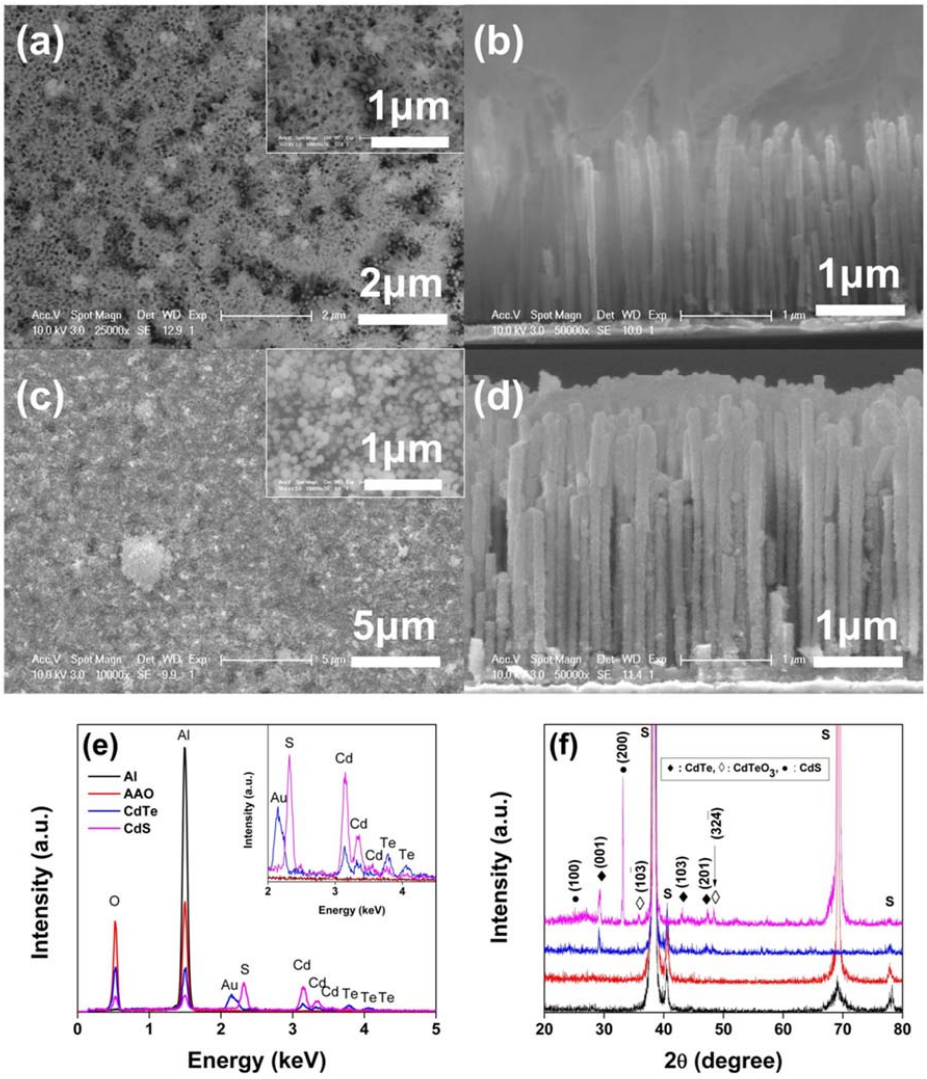

Figure A1.3. SEM Figure 3. SEM images (a),(b) after partial etching of alumina template to expose the top of electrodeposited CdTe NWs and (c),(d) after deposition of CdS on

the top of CdTe NWs by chemical bath deposition (CBD). (e) EDS spectrums and (f) XRD patterns of the sample at each reaction step.

Reference

[1] Li, A.P., F. Muller, A. Birner, K. Nielsch, and U. Gosele, J. Appl. Phys., 1998. 84(11): p. 6023-6026.